TOOLS FOR PHYSICS BEYOND THE STANDARD MODEL

by

CHRISTOPHER A. NEWBY

A DISSERTATION

Presented to the Department of Physics
and the Graduate School of the University of Oregon
in partial fulfillment of the requirements
for the degree of
Doctor of Philosophy

June 2016

DISSERTATION APPROVAL PAGE

Student: Christopher A. Newby

Title: Tools for Physics Beyond the Standard Model

This dissertation has been accepted and approved in partial fulfillment of the requirements for the Doctor of Philosophy degree in the Department of Physics by:

Graham Kribs	Chair
Spencer Chang	Advisor
Jim Brau	Core Member
Michael Kellman	Institutional Representative

and

Scott L. Pratt	Dean of the Graduate School

Original approval signatures are on file with the University of Oregon Graduate School.

Degree awarded June 2016

DISSERTATION ABSTRACT

Christopher A. Newby

Doctor of Philosophy

Department of Physics

June 2016

Title: Tools for Physics Beyond the Standard Model

The standard model (SM) of particle physics is a well studied theory, but there are hints that the SM is not the final story. What the full picture is, no one knows, but this thesis looks into three methods useful for exploring a few of the possibilities.

To begin I present a paper by Spencer Chang, Nirmal Raj, Chaowaroj Wanotayaroj, and me, that studies the Higgs boson. The scalar particle first seen in 2012 may be the vanilla SM version, but there is some evidence that its couplings are different than predicted. By means of increasing the Higgs' coupling to vector bosons and fermions, we can be more consistent with the data.

Next, in a paper by Spencer Chang, Gabriel Barello, and me, we elaborate on a tool created to study dark matter (DM) direct detection. The original work by Anand. *et al.* focused on elastic dark matter, whereas we extended this work to include the inelastic case, where different DM mass states enter and leave the collision. We also examine several direct detection experiments with our new framework to see if DAMA's modulation can be explained while avoiding the strong constraints imposed by the other experiments. We find that there are several operators that can do this.

Finally, in a paper by Spencer Chang, Gabriel Barello, and me, we study an interesting phenomenon know as kinetic mixing, where two gauge bosons can share

interactions with particles even though these particles aren't charged under both gauge groups. This, in and of itself, is not new, but we discuss a different method of obtaining this mixing where instead of mixing between two Abelian groups one of the groups is Nonabelian. Using this we then see that there is an inherent mass scale in the mixing strength; something that is absent in the Abelian-Abelian case. Furthermore, if the Nonabelian symmetry is the $SU(2)_L$ of the SM then the mass scale of the physics responsible for the mixing is about 1 TeV, right around the sweet spot for detection at the LHC.

This dissertation includes previously published and unpublished co-authored material.

CURRICULUM VITAE

NAME OF AUTHOR: Christopher A. Newby

GRADUATE AND UNDERGRADUATE SCHOOLS ATTENDED:

University of Oregon, Eugene, Oregon
Colorado School of Mines, Golden, Colorado

DEGREES AWARDED:

Doctor of Philosophy, Physics, 2016, University of Oregon
Master of Science, Applied Physics, 2010, Colorado School of Mines
Bachelor of Science, Engineering Physics, 2009, Colorado School of Mines

PROFESSIONAL EXPERIENCE:

Graduate Research Assistant

PUBLICATIONS:

Christopher A. Newby. Modeling Three-Body Recombination Rates in Ultracold ^{85}Rb around the 155 G Feshbach Resonance. Colorado School of Mines Thesis, 2010.

Spencer Chang, Christopher A. Newby, Nirmal Raj, and Chaowaroj Wanotayaroj. Revisiting Theories with Enhanced Higgs Couplings to Weak Gauge Bosons. Phys. Rev., D86:095015, 2012.

G. Barello, Spencer Chang, and Christopher A. Newby. A Model Independent Approach to Inelastic Dark Matter Scattering. Phys. Rev., D90(9):094027, 2014.

G. Barello, Spencer Chang, and Christopher A. Newby. Correlated Signals at the Energy and Intensity Frontiers from Nonabelian Kinetic Mixing. 2015. arXiv:1511.02865

ACKNOWLEDGEMENTS

First of all I would like to thank my advisor Spencer Chang for letting me work with him as well as coaching me through the process of writing a paper; from the inception of the basic ideas, working through the fundamental research, looking into relevant theoretical and experimental works, and finally writing the whole thing up.

Also, the hard work and dedication of the other students I worked with is worth mentioning. Without Nirmal, Max, and Gabriel this would have taken me much longer, and that's assuming I would have finished any projects at all. So a big thanks to them.

I would like to thank my friends and family for the moral support through the whole process. Without you I might not have made it...

Finally I would like to thank the University of Oregon for allowing me to work here and for, begrudgingly, paying me. Despite their best efforts to make this process as long and complicated as possible (while saying "get out of here as fast as you can!"), I did it.

TABLE OF CONTENTS

LIST OF FIGURES

Figure Page

LIST OF TABLES

Table Page

CHAPTER I

INTRODUCTION

The standard model (SM) of particle physics has been wildly successful at predicting measurements[1]. Take, for instance, the calculation of the electron's magnetic dipole moment, one of the most accurate theoretical predictions in all of science. This value has been measured to be [2]

$$a_e^{\text{exp}} = 1\,159\,652\,180.73(24) \times 10^{-12}, \tag{1.1}$$

where a_e quantifies the difference between the base Dirac theory (which predicts this value to be zero) and the quantum loop corrections. This measurement is very accurate in and of itself, and the theoretically calculated agrees quite well [3]

$$a_e^{\text{theory}} = 1\,159\,652\,181.13(86) \times 10^{-12}, \tag{1.2}$$

Despite successes like this, there have been some discrepancies between measurements and the SM's predictions. Take, for instance, a similar comparison of the muon's magnetic dipole moment, which is [4–6]

$$\begin{aligned} a_\mu^{\text{exp}} &= 116\,592\,089(54) \times 10^{-11} \\ a_\mu^{\text{theory}} &= 116\,591\,802(42) \times 10^{-11} \end{aligned} \tag{1.3}$$

[1]See the PDG [1] and the many tables of matched theoretical predictions to experimental results contained therein.

which is a 3.6σ difference, and the reason for this difference is currently unknown, though there are models that address this issue by adding a heavy particle with electromagnetic charge or a new gauge boson that couples to the muon[2]. Anomalies like these are what drive particle theory forward, like with the discovery of the neutrino [8, 9] and the charm quark [10–12], and this thesis covers three specific tools to help others explore new, or beyond the SM (BSM), physics.

The first chapter covers a subject that is foremost in many peoples minds: the Higgs boson. Almost four years ago, the Higgs was discovered by the two major detectors at the large hadron collider (LHC) [13, 14]. It agreed remarkably well with theoretical predictions, but there were, and still are, many measurements that needed to be done. There was also, right around the time the announcement was made, a slight anomaly in the Higgs couplings to bosons and fermions [15] as seen in Fig. 1; not much, but the best fit point for the Higgs's coupling to gauge bosons was greater than the SMs prediction. In our paper [16], Spencer Chang, Nirmal Raj, Chaowaroj Wanotayaroj, and I worked with, and elaborated on a model where it is possible to achieve this enhancement: the Georgi-Machacek (GM) model [17].

The measured enhancement to gauge bosons is hard to obtain because only in models with a doubly charged Higgs can this occur without disrupting the unitarization of longitudinal WW/ZZ scattering [18, 19]. In the GM model, the additional Higgs arises from an additional scalar that transforms as a triplet under the $\mathrm{SU}(2)_L$ of the SM with non-zero hypercharge.

Adding another Higgs is not without consequence; aside from increasing the SM-like-Higgs' (hereafter referred to as the Higgs) couplings to fermions and bosons,

[2]See [7] and the references therein for more on these theories.

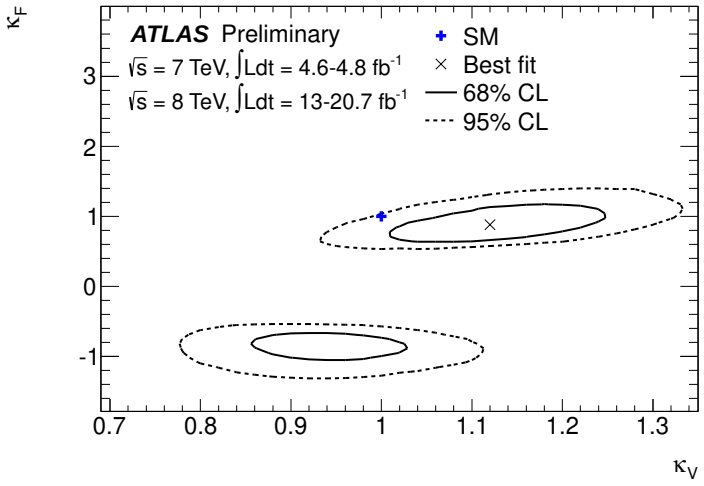

FIGURE 1. Old Higgs couplings to fermions and vector bosons.
Plot of Higgs couplings to fermions (κ_F) and vector bosons (κ_V) assuming only the SM Higgs and that the fermions' couplings to the Higgs is proportional to their masses. Note that the best fit point for positive fermionic coupling has a coupling to vector bosons is greater than one. Plot taken from [15].

including a triplet also changes the ratio of the mass of the weak bosons encapsulated by the ρ parameter [20]

$$\rho \equiv \frac{m_W^2}{m_Z^2 \cos^2 \theta_W} \tag{1.4}$$

where m_W and m_Z are the W and Z boson masses and θ_W is the electroweak mixing angle. The change to ρ is proportional to the vacuum expectation value (vev) of the triplet, which is undesirable since this ratio is very well measured to be $\rho \sim 1.00040 \pm 0.00024$ [1]. To resolve this issue, we impose an $SU(2)_C$ symmetry, the custodial symmetry, to the Higgs sector to preserve the ratio of the masses. This symmetry requires the hypercharge 0 and ± 1 states for the triplet to all be included, and with these states the ρ parameter, at tree level, is exactly one.

In this chapter we also demonstrate several correlated signals and effects, such as production cross section of the SM Higgs and $h \to \gamma\gamma$, and discuss the generalization

of the GM model. Overall, the ability to enhance the Higgs' coupling to gauge bosons is unique to models of this form, and even though recent data has moved the best fit point nearer to the SM prediction [21], see Fig. 2, we could find that nature prefers this to the SM.

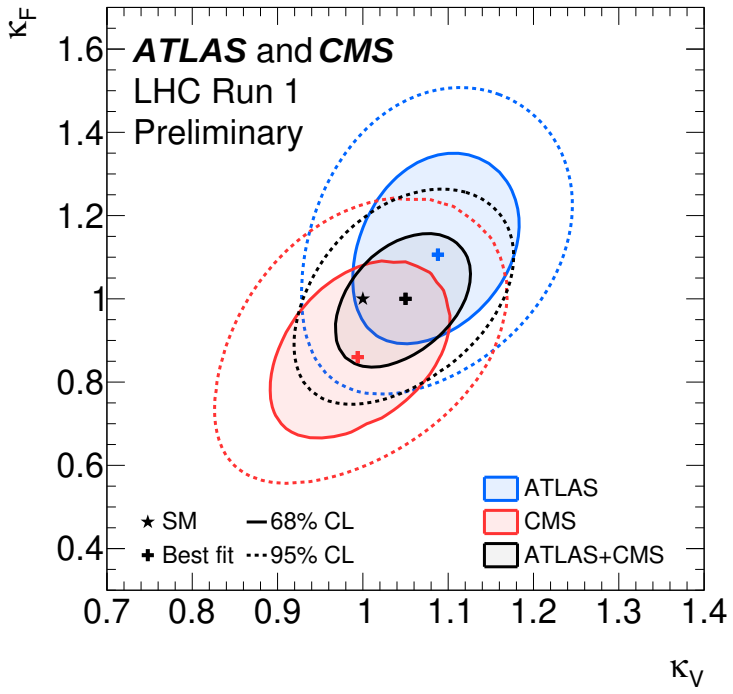

FIGURE 2. New Higgs couplings to fermions and vector bosons.
Plot of Higgs couplings to fermions (κ_F) and vector bosons (κ_V) assuming only the SM Higgs, that the fermions' couplings to the Higgs is proportional to their masses, and that the coupling to fermions is positive. Note that the best fit point for positive fermionic coupling has a coupling to vector bosons is slightly greater than one, but it is consistent with the SM to a large extent. Plot taken from [21].

In the next chapter we move away from collider phenomenology and into the realm of dark matter (DM) direct detection. Dark matter is a theoretically proposed particle that solves many of the gravitational anomalies astronomers have detected, such as galaxy rotation curves, large scale structure, and the CMB spectrum, but little is known of what DM really is, its interactions and mass (see [22, 23] for more

details). The standard picture is that of a single WIMP, or weakly interacting massive particle, that interacts only weakly with the SM and has a large mass. Unfortunately this paradigm is under extreme pressure from many direct detection experiments like XENON [24, 25], LUX [26], CDMS [27], and COUPP [28], though there is one exception. DAMA [29] sees a strong signal for annually modulating DM, a modulation that is predicted because the DM does not orbit our sun like the Earth does. Many of the other experiments claim to rule out this signal as coming from DM, but these limits rely on a very specific form for the DM interaction with the SM. Spencer Chang, Gabriel Barello, and I, in [30], looked at a framework that allows for some wiggle room, namely inelastic DM.

Inelastic DM means that a different DM particle leaves an interaction with a SM particle than the one that collided in the first place. Schematically this can be written as

$$\chi_1 + N \to \chi_2 + N \tag{1.5}$$

where χ_i are the DM particles separated in mass by δ, N is the nucleon they interact with, and $\mathcal{O}_i$ are the operators for the DM-nucleon interaction. This paradigm changes the kinematics of the collision in such a manner that it is possible to explain the DAMA modulation while still evading the bounds imposed by the other direct detection experiments [31]. The change is to the energy conservation of the system, encapsulated by the minimum velocity needed for a scattering event to occur. This velocity is

$$v_{\min} = \frac{1}{\sqrt{2m_N E_R}} \left(\frac{m_N E_R}{\mu_N} + \delta \right) \tag{1.6}$$

where m_N is the nucleon mass, E_R is the incident energy, μ_N is the DM-nucleon reduced mass, and δ is the mass splitting of the two DM particles. Note here that the major difference between elastic and inelastic scattering, the δ term, can significantly increase the minimum velocity, and hence the minimum energy, needed for a scattering event to occur. Mass splittings near the incoming energy of the DM particles in our solar system[3] are therefore much harder to detect at a count-rate experiment as compared to a modulation experiment depending upon the time of year the experiments run.

For our work, instead of focusing on one particular model, we extended the work by Ref. [32], a model independent framework for calculating elastic DM scattering, to the case of inelastic transitions. The method is to break the nonrelativistic interactions into a base set of operators and calculate the nuclear responses to these operators. The list of operators is $(\mathbf{1}, \vec{q}, \vec{v}^{\perp}, \vec{S}_{\chi}, \vec{S}_N)$ where $\vec{q}$ is the momentum transfer, $\vec{S}_i$ is the spin of the DM or the nucleus, and $\vec{v}^{\perp}$ is a velocity that takes into account the relative velocity of the incoming DM and the target nuclei as well as energy conservation.

There is only one modification needed to this method for the inelastic case and that is a change of $\vec{v}^{\perp}$ to account for the change in energy conservation. Because this change doesn't affect the nuclear responses, we can use the basic tools of Ref. [33] while only needing to modify the map from relativistic operators to the nonrelativistic ones. This map is important for accuracy as the operators that depend on $\vec{v}^{\perp}$ can have a change in cross section up to a factor of 4, and more importantly change the location in the peak of the energy spectrum.

[3]For reference the typical energies of a DM collision with the Earth is $E_R \sim 100\,\mathrm{keV}$.

To illustrate this effect, we give examples of how our modifications to Ref. [33]'s program are implemented, and see if any possible explanation for DAMA still exists we looked at several inelastic operators as well as a high-energy model (Magnetic Inelastic DM [34]). From these operators we found some regions of the resulting parameter space where the DAMA result is still allowed when compared to the null results of other direct detection experiments, and with a recent result that calls to question the previously measured conversion factor from electron energy (what the experiment measures) to nuclear energy (the energy in our theories) in iodine [35], these regions grow larger.

The final chapter changes directions again to a framework that has implications for collider and Intensity frontier experiments. Here Spencer Chang, Gabriel Barello, and I, in [36], investigate the peculiar phenomenon where a new gauge boson kinetically mixes with the SM photon. Previous work (see [37]) has focused on the simple mixing of two U(1) gauge groups, where the mixing, written as

$$\epsilon F'_{\mu\nu} F^{\mu\nu} \tag{1.7}$$

where ϵ is the kinetic mixing strength and F, F' are the field strengths for the photon and dark photon. The strength ϵ can have any value[4]. While this term can be written explicitly in the Lagrangian, if we assume nature has diagonalized the gauge bosons, so no mixing occurs naturally, then the only way for a term like this to emerge is through loops made of a particle, called the mediator, charged under both U(1) gauge groups [38]. This causes the predictions for ϵ to vary wildly, as the mixing strength usually goes as $\log(m_{\text{med}})$ at best.

[4]Theoretical models predict a range of $10^{-13} < \epsilon < 10^{-2}$ [37].

However, if one of the gauge groups is made more complex, such as changing one of the kinetically mixed groups to the $\mathrm{SU}(2)_L$ of the SM, then the interaction which produces kinetic mixing is changed to

$$\frac{1}{\Lambda^n}\Delta^a F^a_{\mu\nu} F^{\mu\nu} \tag{1.8}$$

where $F^a_{\mu\nu}$ is the field strength for a nonabelian gauge boson, Δ^a is a field or combination of fields in the adjoint representation of the gauge group, Λ is a mass scale set by the mediator, and n is an integer needed to make this operator dimensionless[5]. Many forms for Δ^a are allowed, but we choose $\mathrm{SU}(2)_L$ of the SM for our gauge group, so we have $\Delta^a = H^\dagger \tau^a H$, where H is the SM Higgs field and τ^a are the Pauli spin matrices.

With this choice, and rewriting the mixing to be between the U(1) of the dark photon with the U(1) of electromagnetism (after the Higgs has already broken the electroweak gauge symmetry), the mixing strength becomes

$$\epsilon = \frac{v^2}{\Lambda^2} s_W \tag{1.9}$$

where v is the SM Higgs vev and s_W is the sine of the electroweak mixing angle. Looking at allowed mixing strengths, see Fig. 3, we find that for a strength of $\epsilon \sim 10^{-4}$, the mediator mass scale is $\Lambda \sim 1\,\mathrm{TeV}$, which is well within the LHC's reach in the near future.

With this framework, we explore this unique phenomenon by creating a fairly basic model which generates this type of kinetic mixing and discuss some of the methods for searching for it at the LHC.

[5]Its value is one over the mass dimension of Δ^a.

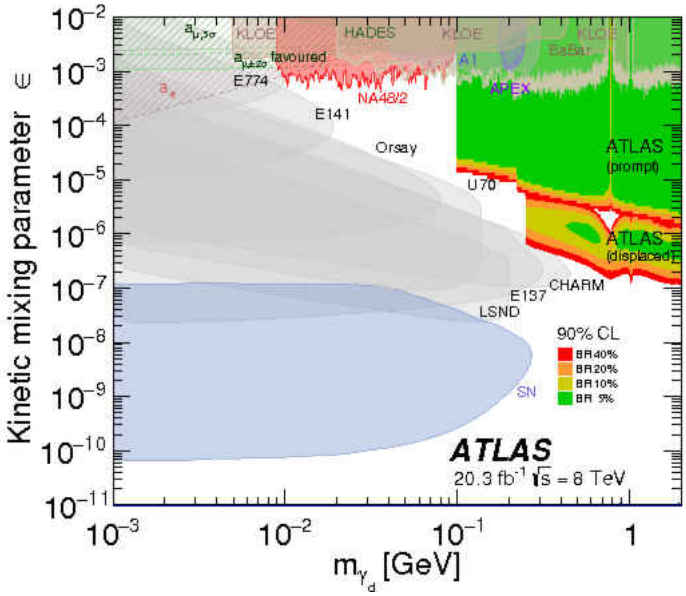

FIGURE 3. Constraints on DP parameter space.
This figure shows the constraints on the $(\epsilon, m_{A'})$ space due to fixed target, beam dump, and collider experiments. Plot taken from [39].

But to begin we look back in time to when the discovery of the Higgs boson had yet to be announced.

CHAPTER II

ENHANCED HIGGS

This chapter is work done by myself, Spencer Chang, Nirmal Raj, and Chaowaroj Wanotayaroj [16].

Introduction

This year is a key turning point in particle physics with the LHC's discovery of a boson compatible with the Standard Model (SM) Higgs particle. The increased luminosity and energy has enabled the Higgs interactions with the SM to be measured more accurately. These crucial measurements will be the foundation for the argument that electroweak symmetry is broken by the vacuum expectation value of a fundamental scalar.

The excitement of the latest LHC [13, 14] and Tevatron [40] Higgs analyses is that they are all consistent with the Standard Model Higgs at 125 GeV. There is also an interesting indication that the data prefers a Higgs boson with nonstandard values for its interactions with the Standard Model, particularly in the diphoton channel. The statistical power of this preference is weak, but if this is confirmed with further data, this would be an enormous revolution, pointing to new physics beyond the Standard Model. Anticipating this possibility, it is worth investigating the theoretical ramifications and correlated signals that would result for different Higgs couplings.

One particularly interesting aspect of recent model-independent fits to Higgs couplings is a hint that the Higgs coupling to weak gauge bosons is enhanced relative to the Standard Model [41–45]. This preference is dominated by excesses in ATLAS/CMS diphoton channels sensitive to Higgses produced in vector boson

fusion [46, 47]. This preference is also observed in the ATLAS coupling analysis [48], whereas the CMS analysis does not prefer enhancement [14].

From a theoretical perspective, such a large coupling to weak gauge bosons is particularly surprising since its value is crucial for unitarizing longitudinal WW/ZZ scattering. This unitarity argument suggests that the coupling cannot be larger than the Standard Model, unless there is a doubly-charged Higgs [18] which can be seen by an isospin analysis of WW scattering [19].

Thus, confirmation of enhanced Higgs coupling to electroweak gauge bosons would in itself be a sign for new physics, motivating a survey of theories that allow such enhancements. Such theories, already considered in the past, have experimental challenges; in particular, they have potentially large precision electroweak corrections to the ρ parameter. This is due to the need for a large contribution of electroweak symmetry breaking to come from a higher representation of $SU(2)_L$. However, this problem can be solved by extending custodial $SU(2)$ symmetry [49, 50], which we refer to as $SU(2)_C$, to these theories [17]. The phenomenology of these models was studied long ago [51, 52] and a generalization of the original model is possible [53], leading to an entire family of possible theories to consider.

In light of the current data and in anticipation of future LHC Higgs results, we revisit these theories, looking for the telltale consequences given specific Higgs couplings and the correlated signals of these models. These theories are interesting since they serve as theoretically and experimentally consistent phenomenological frameworks which extend the coupling parameter space explored by the model-independent fits to Higgs couplings.

The organization of the paper is as follows: in section 2.2, we review a class of theories with enhanced Higgs couplings based on the Georgi-Machacek model; in

section 2.3, we explore the phenomenology of the neutral CP-even Higgs sector; in section 2.4, we discuss the extended Higgs scalars of these models, briefly touching upon their phenomenology and effects on the Higgs decay to photons; finally, in section 2.5, we conclude. We include further details about the Georgi-Machacek model in Appendix 2.A.

Theories with Enhanced Higgs Couplings

In recent years, people have outlined the key ingredients to have enhanced couplings to electroweak gauge bosons for Higgs scalars [18, 19]. One of the necessary properties is the existence of a doubly-charged Higgs. One such theory is well known, the Georgi-Machacek (GM) model [17]. From this example, to enhance the Higgs coupling, one needs a large amount of electroweak symmetry breaking from a higher representation of $SU(2)_L$ than the standard Higgs doublet. This naturally leads to a doubly-charged Higgs state. However, precision electroweak constraints, in particular from the ρ parameter, strongly constrain electroweak symmetry breaking from such higher representations. The GM model avoids this by extending custodial $SU(2)$ symmetry [49, 50] to this theory, naturally controlling the contributions to ρ. This model was explored in depth (see for e.g. [51, 52]), and in particular, we follow the notation in [52].

The GM model has electroweak symmetry breaking from both a standard Higgs doublet and a particular set of $SU(2)_L$ triplets (one complex triplet with hypercharge 1 and one real triplet with hypercharge 0). The custodial symmetry is manifest by

writing the fields as

$$\phi = \begin{pmatrix} \phi^{0*} & \phi^{+} \\ \phi^{-} & \phi^{0} \end{pmatrix}, \quad \chi = \begin{pmatrix} \chi^{0} & \xi^{+} & \chi^{++} \\ \chi^{-} & \xi^{0} & \chi^{+} \\ \chi^{--} & \xi^{-} & \chi^{0*} \end{pmatrix} \tag{2.1}$$

where the matrices ϕ, χ transform as $(2, \bar{2}), (3, \bar{3})$ under $(SU(2)_L, SU(2)_R)$. There are four (nine) real degrees of freedom in $\phi\,(\chi)$ due to the following field relations $\phi^{+} = -\phi^{-*}, \xi^{+} = -\xi^{-*}, \xi^{0} = \xi^{0*}, \chi^{++} = \chi^{--*}, \chi^{+} = -\chi^{-*}$. If the vacuum expectation values (vevs) of ϕ, χ are diagonal, $(SU(2)_L, SU(2)_R)$ breaks down to the diagonal custodial $SU(2)_C$ symmetry. A potential can be written down for these fields that preserves the custodial symmetry, see Eq. 2.9. Radiative corrections can generate custodial $SU(2)$ violating terms, in particular those due to hypercharge gauge interactions [52]. Such terms are dependent on ultraviolet physics and thus could be small in certain setups such as composite Higgs models [17, 54]. For the rest of this paper, we will assume such terms can be neglected, as they are required to be small due to electroweak precision constraints.

Under this approximation, it is convenient to discuss the physical Higgs bosons in terms of custodial $SU(2)$ multiplets. The field content under $SU(2)_C$ are two neutral singlets $H_1, H_1^{'}$, two triplets H_3, G_3, and a five-plet H_5. $H_1^{'}$ and H_5 appear in χ, while the G_3 are the eaten goldstone bosons of electroweak symmetry breaking. This is realized by the vevs

$$\begin{aligned} \langle \phi^0 \rangle &= v_\phi/\sqrt{2}, \quad \langle \chi^0 \rangle = \langle \xi^0 \rangle = v_\chi, \\ v_\phi &= \cos\theta_H\, v, \quad v_\chi = \sin\theta_H\, v/\sqrt{8}, \end{aligned} \tag{2.2}$$

where we have defined a mixing angle for the vevs θ_H. Gauge boson masses are generated, $m_W^2 = m_Z^2 \cos^2\theta_W = \frac{1}{4}g^2(v_\phi^2 + 8v_\chi^2) = \frac{1}{4}g^2v^2$, predicting $\rho = 1$ at tree level as expected. For more details on the scalar spectrum, see appendix 2.A and [52].

In the GM model, fermion masses come from coupling to the Higgs doublet in ϕ. Thus, generating the SM fermion masses will put a lower bound on $\cos\theta_H$. The couplings of the Higgs bosons to SM fields can be easily determined. Here, we focus on the couplings for the $SU(2)_C$ singlets $H_1, H_1^{'}$. The fermion couplings are

$$c_{H_1} = 1/\cos\theta_H, \quad c_{H_1'} = 0 \tag{2.3}$$

and the couplings to WW/ZZ pairs are

$$a_{H_1} = \cos\theta_H, \quad a_{H_1'} = \sqrt{8/3}\sin\theta_H. \tag{2.4}$$

Note: we have followed the convention of recent model-independent fits to Higgs couplings to normalize to the SM values, defining a fermion coupling $c = g_{h\bar{f}f}/g_{h\bar{f}f}^{SM}$ and gauge boson coupling $a = g_{hWW}/g_{hWW}^{SM}$. Here, one sees that the vev contributions to the W, Z masses in the χ field enable H_1' to have enhanced couplings to gauge bosons. Thus, the GM model is a consistent theory where Higgs couplings to W and Z can exceed the Standard Model value. Again, this is consistent with the requirement in [18, 19] since the five-plet H_5 has a doubly-charged Higgs. Furthermore, due to the custodial symmetry of the model, we can have a large contribution of electroweak symmetry breaking from the vev of χ. This enables the GM model to have enhanced gauge boson couplings in an allowed region of parameter space, for $\sin\theta_H > \sqrt{3/8}$, unlike simpler theories with only a single Higgs $SU(2)_L$ triplet.

The GM model lends itself to a simple generalization with ϕ and a nontrivial multiplet $\chi = (r, \bar{r})$, where r is a spin j representation of $SU(2)$ with $r = 2j + 1 > 2$. Such an extended breaking sector was originally noted in [53] and was used to generalize the GM model in [55]. Custodial $SU(2)$ can be extended to this generalization and the physical Higgs multiplets will be from ϕ (H_1 and G_3) and from χ ($SU(2)_C$ multiplets of spin $2j, 2j-1, \ldots, 0$). This modification changes the coupling of the singlet in χ to

$$a_{H_1'} = \sqrt{4j(j+1)/3}\sin\theta_H. \tag{2.5}$$

Thus, larger representations used for χ lead to an even stronger coupling to gauge bosons as well as having an increasingly complicated sector of physical Higgs bosons.

Higgs phenomenology

In this section, we consider the phenomenological consequences of the GM model and its generalization, focusing on the $SU(2)_C$ singlets, deferring to the next section a discussion of the nontrivial $SU(2)_C$ multiplets. Our emphasis is on LHC signals, for the GM model's phenomenology at LEP-2 see [56]. In terms of the model-independent Higgs couplings (a, c), the GM model is an important phenomenological framework because it extends the theoretically allowed parameter space. In general, H_1, H_1' can mix, leading to mass eigenstates

$$\begin{aligned} h_1 &= \cos\alpha\, H_1 + \sin\alpha\, H_1', \\ h_2 &= -\sin\alpha\, H_1 + \cos\alpha\, H_1'. \end{aligned} \tag{2.6}$$

From this mixing angle, it is easy to determine the couplings for h_1, h_2, which we denote by $a_{1,2}, c_{1,2}$. Due to the current Higgs excesses and for illustration we will take h_1 to be the Higgs hinted at in the data, fixing its mass to 125 GeV and assuming its couplings will be measured with future data. One can show that the physically allowed parameter space for this eigenstate is $|a_1| \leq \sqrt{8/3}$, while the GM generalization will raise the allowed range to $|a_1| \leq \sqrt{4j(j+1)/3}$.

Fitting to the couplings for the first mass eigenstate (a_1, c_1) uniquely determines the couplings for the other eigenstate. In Fig. 4, the absolute values of the couplings a_2, c_2 are shown for the GM model. We take the absolute values for the figure presentation due to discontinuous flips of signs across the parameter space. The relative sign of a_2, c_2 is important in determining h_2's decay to photons and we find that there is a relative minus sign between a_2, c_2 only in the upper right portion of the plots (for values $c_1 > 1/a_1$), giving a constructive interference that enhances the photon decay. On these figures, we plot constraints on $\sin^2\theta_H$ due to modifications to the $Z \to \bar{b}b$ decay from loops involving H_3, which for the GM model and its generalization are $\sin^2\theta_H \leq 0.33\,(0.73)$ for $m_{H_3} = 200\,(1000)$ GeV [57]. This constraint is plotted in Fig. 4, excluding the right side of the plots and is shown by the shaded contours in tan and gray for the two H_3 masses. From the figure, one notices an interesting asymmetry between a_2, c_2, where c_2 tends to increase in magnitude as one goes to larger a_1, whereas a_2 has the opposite trend.

The recent model-independent fits to (a_1, c_1) performed by a series of papers [41–45] have shown that there are certain aspects of the Higgs analyses which prefer a_1 values larger than 1. The official ATLAS Higgs coupling analysis also saw a preference for $a_1 > 1$ for $c_1 \sim 1$ [48]. In the ATLAS fit, there is also a region that allows negative c_1 values. but for the region around the SM value, ATLAS requires an enhanced a_1.

Thus, the LHC data is highlighting two interesting regions, one for positive c_1 and one for negative c_1, both with suppression from the SM value of $|c_1| = 1$. To demonstrate the qualitative behavior of our model in these domains and also for fermiophobic couplings we chose the following benchmarks to analyze: *i*) near the SM values but with slight enhanced a_1 and suppressed c_1 around $(a_1, c_1) = (1.1, 0.8)$, *ii*) a flipped region where c_1 is near -1 and a_1 slightly suppressed around $(a_1, c_1) = (0.8, -0.7)$, and *iii*) a fermiophobic region with enhanced a_1 around $(a_1, c_1) = (1.4, 0)$.

A complication that will be discussed in the next section is that most of the mentioned model-independent fits to Higgs couplings assume only couplings to Standard Model particles. In particular, the Higgs decay to photons is calculated from loop diagrams with the top quark and W boson. In the GM model and its generalizations there are additional loop diagrams due to the additional scalar content. These must be taken into account to determine the best fit (a_1, c_1) couplings. For now, we put aside this uncertainty, deferring details to the next section where we discuss the effects of these loops.

As can be seen in Fig. 4, the GM model is able to populate a large region of the (a_1, c_1) parameter space considered in these fits. The limit from $Z \to \bar{b}b$ cuts off the large a_1 region, but as will be shown later, the generalizations for the GM model help to alleviate that constraint. Notice that the GM model nicely accommodates a fermiophobic Higgs while still having perturbative Yukawa couplings to generate fermion masses (which scale as $1/\cos\theta_H$). We see that the h_2 couplings are suppressed near the SM point and enhanced near the flipped region of negative c_1. This plays a large role on the constraints and signal prospects for h_2.

We can first look at the h_2 phenomenology by comparing its signal rate to the Standard Model Higgs. To simplify matters, we consider only the decays into

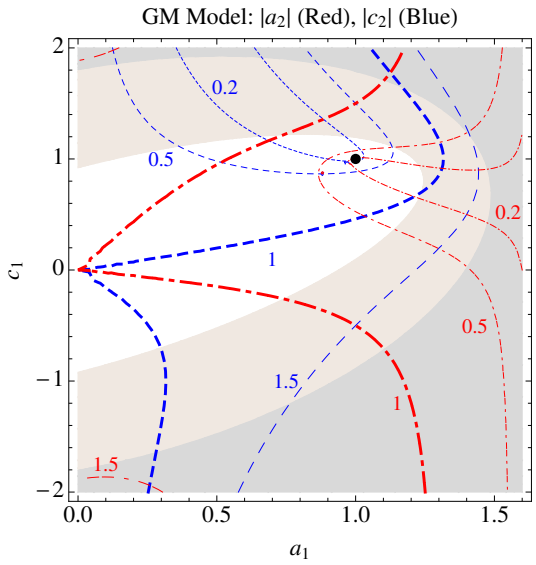

FIGURE 4. Absolute value of couplings a_2, c_2 for Georgi-Machacek model. Absolute value of couplings a_2, c_2 for Georgi-Machacek model as a function of the effective Higgs couplings for the h_1 mass eigenstate (a_1, c_1). The black dot shows the Standard Model values. The contours are (Red, Dot-Dashed) for a_2 and (Blue, Dashed) for c_2. The shaded contours show the excluded region from the correction to $Z \to \bar{b}b$, shown from left to right for $m_{H_3} = 200, 1000$ GeV [57].

WW/ZZ. This is a useful approximation because it focuses on one number, but is also practical since searches for a heavy Standard Model Higgs are most sensitive to these decays [13, 14]. We use the ratio of rates

$$R = \frac{\sigma(pp \to h_2)}{\sigma(pp \to h_{SM})} \times \frac{Br(h_2 \to WW)}{Br(h_{SM} \to WW)} \tag{2.7}$$

where the production channel σ is taken to be both gluon and vector boson fusion production cross sections at $\sqrt{s} = 7$ TeV LHC [59]. This assumes that the efficiencies for heavy Higgs searches are insensitive to the production mechanism and ignores the change in the Higgs width, which are good enough approximations for our purposes. We take into account decays of the heavy Higgs into the lighter one, $h_2 \to h_1 h_1$, which is important for masses where this is kinematically open (i.e. $m_{h_2} > 2m_{h_1} =$

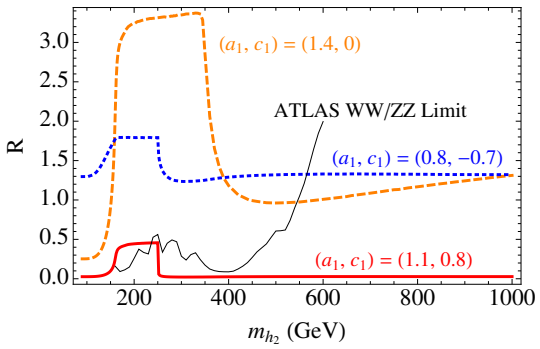

FIGURE 5. R dependence on m_{h_2}.
R dependence on m_{h_2} for three values of (a_1, c_1). The ATLAS limit on WW/ZZ Higgs searches [58] is shown in black.

250 GeV). This R variable depends on a_2, c_2, m_{h_2} and its dependence on m_{h_2} is shown in Fig. 5 for values representative of the three regions mentioned above.

We can now compare this ratio to the current limits for the SM Higgs in the heavy mass range. In order to see if h_2 is allowed in certain parts of the mass range, we look at the latest combined Higgs limits from ATLAS [58] and CMS [14], using the best limit of the two as a function of mass. Since our R variable looks at WW/ZZ decays, we restrict ourselves to the mass range $165 - 600$ GeV where the combined limits are dominated by those decays. The limits from the experiments fluctuate quite a bit as a function of mass, as can be seen in Fig. 5 for the ATLAS limit [58]. Due to the fluctuations, to get a simple understanding of what mass ranges are interesting we have to make some approximations. First of all, R is typically flat as a function of m_{h_2} for a region at lower mass ($165 - 250$ GeV) and higher mass ($400 - 600$ GeV) as shown in Fig. 5. This is due to the turn on of the $\bar{t}t$ and $h_1 h_1$ decays in the intermediate range. In those two regions, we find the largest R value, Max(R_{exp}), allowed by both the ATLAS and CMS combinations is respectively 0.6 and 1 in the lower and higher mass region.

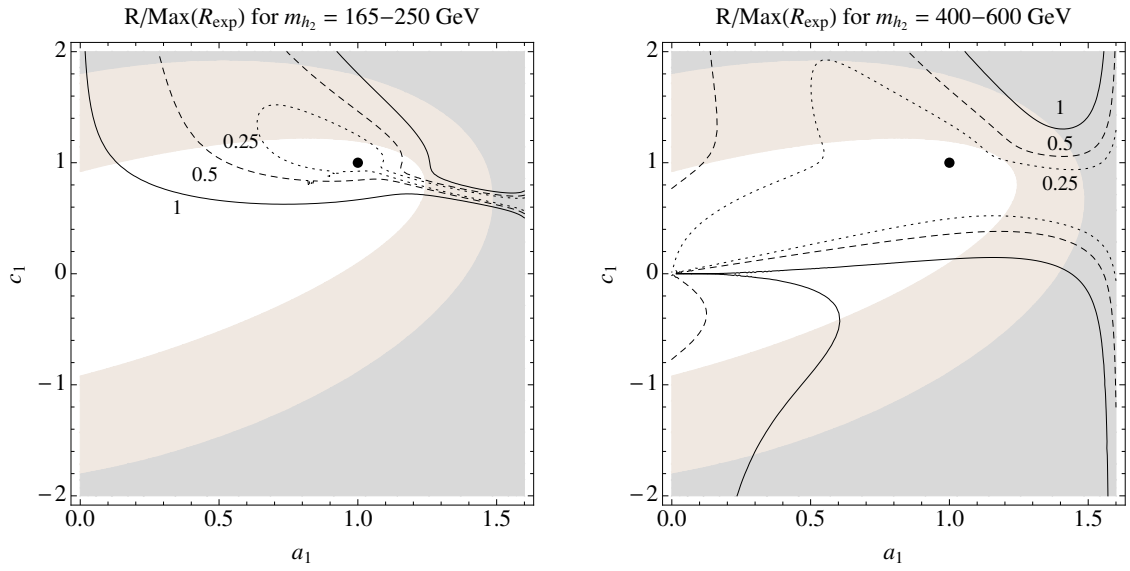

FIGURE 6. $R/\mathrm{Max}(R_{exp})$.
$R/\mathrm{Max}(R_{exp})$ for the h_2 mass ranges $165 - 250$ GeV (left) and $400 - 600$ GeV (right). If the value is greater than 1, h_2 is not allowed in that mass range by the LHC Higgs combined limits on WW/ZZ decays.

To determine if h_2 is allowed in either of these two regions, we divide the average R value of that range by the largest value allowed by the experiments. This gives one an idea of how constrained an h_2 would be in those mass ranges. Furthermore, one can then naively estimate how much additional luminosity would be needed to start constraining this h_2, since it should take a factor of $(R/\mathrm{Max}(R_{exp}))^{-2}$ increase in luminosity from simple statistical scaling. We plot this normalized R in Fig. 6 for the two mass ranges. Again, for values larger than 1, these plots say that that the h_2 cannot exist in this mass range. As seen in the lefthand plot, only a narrow region of the (a_1, c_1) parameter space allows h_2 in the low mass range, primarily around the SM point where the coupling a_2 can be suppressed. In the righthand plot, one sees that there is a wider range allowed by the WW/ZZ searches in the mass range of $400 - 600$ GeV for h_2. The strongest constraints are for negative c_1 and large a_1.

This reflects the fact that the a_2, c_2 couplings are enhanced there; in this parameter space, searches for h_2 with mass above 600 GeV are more motivated.

In certain parts of parameter space, it could also be worthwhile to explore decays of h_2 into $h_1 h_1$ and $\bar{t}t$. In Fig. 7, we plot the ratio

$$r(X) = \frac{\sigma(pp \to h_2)}{\sigma(pp \to h_{SM})} \times Br(h_2 \to X) \tag{2.8}$$

for $X = h_1 h_1, \bar{t}t$ for a h_2 of mass 400 GeV. Notice that this $r(X)$ does not have a Standard Model value for the branching ratio in the denominator. This variable r is designed to determine situations where these decay signals have reasonable rates by normalizing to the SM Higgs production. Thus, it indicates when the production of h_2 and the branching ratio of these modes are both large. As can be seen in Fig. 7, for enhanced a_1, h_2 has a rate into top pairs substantially larger than the Standard Model ($r(\bar{t}t)_{SM} = Br(h_{SM} \to \bar{t}t) \lesssim 0.2$), and thus would be interesting for top resonance searches [60, 61]. The decay into h_1 pairs can also have reasonable rates with $r(h_1 h_1) > 0.25$, but is suppressed in the fermiophobic and $c_1 > 1$ region. There are a variety of strategies to search for these which will depend on the branching ratios of h_1 but could be interesting — for example, in $4b$ [62] or $2b, 2\gamma$ [63] signal topologies.

We can also put mass bounds on h_2 by requiring that the quartic couplings in the potential Eq. 2.9 remain perturbative. To illustrate this, we restrict the quartic couplings $|\lambda_{1,2,3}| \leq 4\pi$ to put upper bounds on m_{h_2}. Since the masses scale as $\sqrt{\lambda} v$, for most of the parameter space this allows one to decouple h_2 to masses above the existing Higgs searches (> 600 GeV). However, there are some regions of (a_1, c_1) whose solutions for θ_H, α put more stringent upper bounds on m_{h_2}. In particular, for $a_1 < 1$, near the $a_1 = c_1$ line, $\sin\theta_H$ approaches zero. This puts a stringent constraint

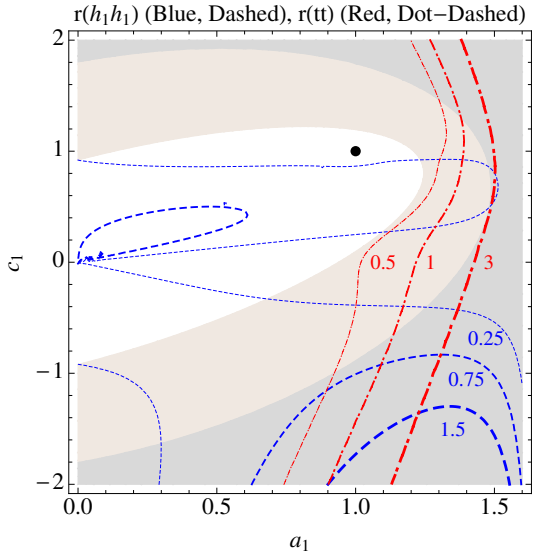

FIGURE 7. $r(X)$ of h_2 to $2h_1$ and $\bar{t}t$,
$r(X)$ of h_2 to $2h_1$ (Blue, Dashed) and $\bar{t}t$ (Red, Dot-Dashed) for a 400 GeV h_2. This variable is large when the signal rates for these Higgs decays are large compared to the Standard Model Higgs production cross section.

on the h_2 mass, since a heavy h_2 requires a large $\lambda_2 \sim 1/\sin^2\theta_H$. One can see this behavior in Fig. 8, as the constraint is only serious around the diagonal in the upper half. Thus, this theoretical constraint only sets a meaningful upper bound for a small fraction of the parameter space.

For generalizations of the GM model, the phenomenology of h_2 changes subtly, as shown in Fig. 9 for the $(4, \bar{4})$ model, where the largest a_1 coupling allowed is increased to $\sqrt{5}$. One sees that the $Z \to \bar{b}b$ constraint allows a larger region of (a_1, c_1) coupling space. The general behavior of the a_2, c_2 contours is the same, although the allowed sizes of the couplings are similarly increased. This trend should only continue as one goes to even larger representations for χ. Since the behavior for the h_2 couplings are similar, the comments on the h_2 phenomenology apply as well to these generalizations. We also found that the upper bound on m_{h_2} from the magnitude of the quartic couplings becomes more stringent as j increases, extending

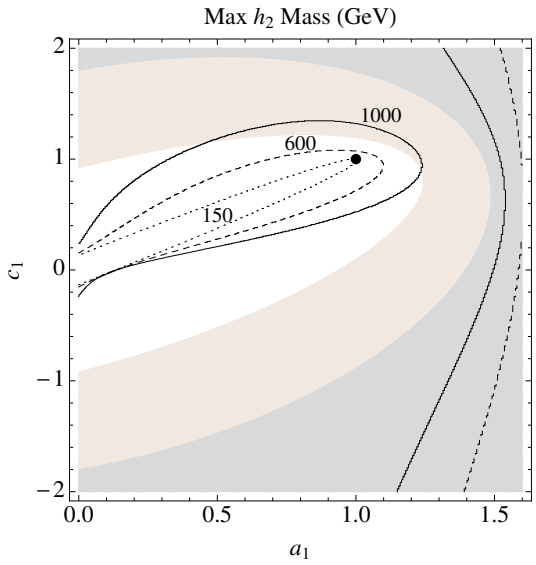

FIGURE 8. $m_{h_2}^{\max}$.
The upper bound on the h_2 mass from imposing an upper limit on the quartic coupling magnitudes $|\lambda_{1,2,3}| \leq 4\pi$.

the region around the diagonal where it is impossible to decouple h_2 above 600 GeV, which improves the chances of seeing a light h_2.

To summarize, the parameter space of the h_1 phenomenology is in one-to-one correspondence with that of h_2. One can determine general features of h_2's phenomenology by combining the information from Fig. 6 and 7. For region i of positive (a_1, c_1) near the SM values, h_2 generally has suppressed couplings; thus in this region, LHC analyses should continue to look in mass ranges where the Standard Model Higgs has already been ruled out to dig out the suppressed rates of this partner Higgs. For region ii of negative c_1 and slightly suppressed a_1, one sees that h_2 couplings to fermions and electroweak gauge bosons are generically enhanced, requiring the h_2 to be heavy enough to be consistent with LHC Higgs searches, $\gtrsim 600$ GeV. However, with its enhanced rate, it would be very interesting to see updated searches for heavy Higgses that extend the mass range. In both these regions, searches

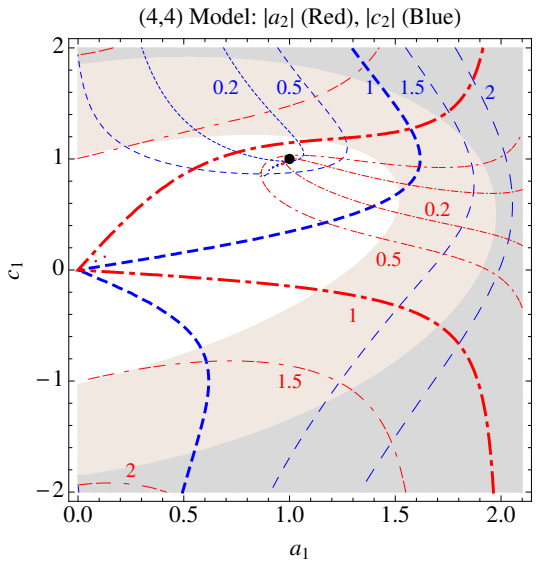

FIGURE 9. Absolute value of couplings a_2, c_2 for the $(4, \bar{4})$ model. Absolute value of couplings a_2, c_2 for the $(4, \bar{4})$ model as a function of the effective Higgs couplings for the h_1 mass eigenstate (a_1, c_1). The black dot shows the Standard Model values. The contours are (Red, Dot-Dashed) for a_2 and (Blue, Dashed) for c_2.

looking for decays into h_1 pairs can also be important. Finally, in region *iii* where h_1 is fermiophobic, h_2 tends to be fermiophilic with enhanced couplings to fermions and with a suppressed coupling to gauge bosons. This h_2 could also be observed in heavy Higgs and in top pair resonance searches [60, 61].

More Model-dependent Signals

Now we will discuss the phenomenology of the scalar fields appearing in nontrivial $SU(2)_C$ multiplets. These multiplets can have quite exotic phenomenology due to their nonstandard quantum numbers. For example, in the five-plet H_5 there is a doubly-charged Higgs. Searches for doubly-charged Higgses at the LHC have predominantly focused on pair producing them, followed by their decays into lepton pairs [64, 65]. Such searches are dependent on Yukawa couplings to χ that give

neutrino masses and thus are model-dependent. However, due to the custodial symmetry in the GM model, it is also possible to get a large contribution to electroweak symmetry breaking to occur in the triplets of χ, leading to a significant single production of H_5^{++} via W^+W^+ fusion. Some early analyses have shown promising prospects for this to be discovered at LHC with $\sqrt{s} = 8$ TeV [66] if the χ vev is large enough and H_5 is light enough. Such searches would be highly motivated if Higgs couplings to gauge bosons get a strong preference for enhancement. The scalars in H_3 are very similar to the heavy Higgses of the minimal supersymmetric Standard Model, where the couplings to fermions are enhanced for large $\sin\theta_H$ and there is no coupling to gauge bosons. However, since there is only a single Higgs doublet in ϕ, these scalars couple universally to up and down-type fermions according to mass. Unfortunately, the constraint from $Z \to \bar{b}b$ [57] tends to push the H_3 to masses too heavy to search for.

The final decay products of these scalars can be even richer, since the different custodial multiplets can cascade into each other, either through W/Z emission or into Higgs pairs. In our approximation, these decays are governed by $SU(2)_C$, with decays emitting a W/Z changing j by 1 and the Higgs pair decays allowed if $j = j_1 + j_2$. Incorporating $SU(2)_C$ violation would split the states within the multiplets, potentially allowing W transitions if the splittings are large enough. The generalizations of the GM model have a richer Higgs sector, given the larger content in χ, leading to even more exotic charges. However, in all of these theories, it is possible to decouple these non-singlet custodial multiplets to masses $\sim \sqrt{4\pi}v \sim 800 - 1000$ GeV, which is the upper bound requiring WW scattering to be unitarized perturbatively (see for e.g., [52]). A more sophisticated analysis of the GM model combining several channels gives more stringent mass limits; in particular

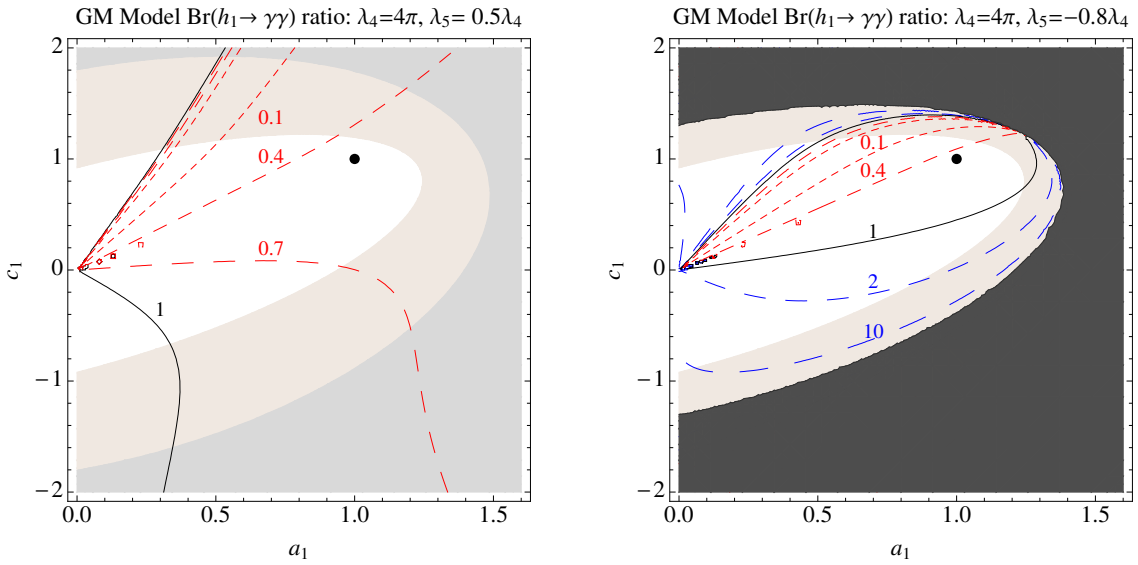

FIGURE 10. Loop effects on the h_1 decay to photons.
Two example plots of the loop effects on the h_1 decay to photons, taking into account only the H_3, H_5 effects from the quartics λ_4, λ_5 in the potential. The plotted contours are the branching ratio to photons with these effects accounted for divided by the branching ratio considering just the a_1, c_1 couplings. The blacked out region is where $m_{H_5} \leq 100$ GeV.

$m_{H_1'} < 700$ GeV, $m_{H_3} < 400$ GeV, $m_{H_5} < 700$ GeV [67], constraining how much these scalars can be decoupled, which improves the possibility of discovering these bosons.

Interestingly, since these additional multiplets appear in nontrivial $SU(2)_C$ multiplets, the neutral Higgses do not have to have equal couplings to W^+W^- and ZZ as compared to the Standard Model. For example, the H_5^0 has $a_{WW} = \sqrt{1/3}\sin\theta_H$ and $a_{ZZ} = -\sqrt{4/3}\sin\theta_H$. Thus, these neutral scalars can provide examples of Zphilic Higgs [68], without large custodial $SU(2)$ violation. In this scenario, the five-plet is the only viable option, since the three-plet does not couple to gauge bosons (due to its CP properties) and higher multiplets cannot couple to two gauge bosons (if $SU(2)_C$ is preserved). Thus, in these theories, a Zphilic Higgs predicts both a doubly-

charged and singly-charged Higgs with mass near 125 GeV. For more discussion on the constraints of custodial $SU(2)$ on the allowed scalar couplings, see [69].

Finally, these additional Higgses have an important effect on the $SU(2)_C$ singlet phenomenology. As discussed recently in [70–72], loop effects of additional charged particles will induce corrections to the H_1, H_1' width into photons. In the GM model, the charged scalars in H_5, H_3 tend to have contributions with the same sign as the top quark; hence, these effects tend to cancel against the W^+ loop, leading to a smaller decay rate into photons. In particular, the couplings in Eq. 2.11 tend to destructively interfere when the λ couplings are positive. To illustrate this effect cleanly, we consider the loop diagrams of the charged scalars H_3, H_5 that are proportional to λ_4, λ_5, the quartic couplings responsible for their mass, see Eq. 2.10. The lefthand plot in Fig. 10 is an example of the modification to the h_1 diphoton branching ratio, where λ_4, λ_5 are both positive, demonstrating the destructive interference. It is also possible to have negative λ's to get constructive interference, but typically this makes the scalars lighter and risks some of the scalars getting tachyonic masses. This can be seen in the righthand plot in Fig. 10, where $\lambda_5 = -0.8\lambda_4$ and the black region shows where $m_{H_5} \leq 100$ GeV. Both these plots show that to maintain the same branching ratio to photons, it is usually necessary to go to larger a_1 and smaller c_1 values.

In generalizations to the GM model, the higher charges of the additional Higgs states can exacerbate the interference, unless one goes to a large enough representation where the entire sign of the amplitude to photons is flipped. However, interestingly, Eq. 2.12 shows that for larger representations of χ, the contribution of λ_5 to the mass of the largest $SU(2)_C$ multiplet is reduced relative to λ_4. However, from Eq. 2.13, one sees that λ_5's contribution to the H_1' coupling to this state is not reduced. Thus, it is easier to have negative λ_5 in the generalizations to reduce the destructive interference,

while avoiding tachyonic masses for scalars. To summarize, these loop contributions are an important effect that complicates the interpretation of the model-independent fits which for the most part include only the top and W loop. A notable exception is a recent fit which analyzed the Georgi-Machacek model parameters and found an improved fit relative to the Standard Model [42]. As a final comment, we note that in a particular Higgs decay channel it is possible with enough statistics to infer the ratio of a_1/c_1 by looking at the rate of gluon fusion versus vector boson fusion. Some combined fit will eventually be able to determine the Higgs couplings to fermions, gauge bosons, *and* any new diagrams inducing decays to photons, which will help pin down these coupling uncertainties in these models.

Conclusion

In light of current and future LHC Higgs searches, we have revisited theories where the Higgs can have enhanced couplings to electroweak gauge bosons. In particular, we reexamined the Georgi-Machacek model and its generalizations where higher "spin" representations of $SU(2)_L$ break electroweak symmetry while maintaining custodial $SU(2)$. These theories widen the allowed couplings for the Higgs, serving as a consistent theoretical and experimental framework to explain enhanced Higgs couplings to W and Z bosons, as well as fermiophobic Higgses.

The phenomenology of the CP-even $SU(2)_C$ singlet sector is particularly interesting, since the couplings of the two Higgses are in one-to-one correspondence. Our assumption is that one of the scalars, h_1, will have its couplings to gauge bosons (a_1) and fermions (c_1) pinned down by future LHC analyses. Currently, fits to LHC Higgs analyses indicate two interesting regions of h_1 coupling space which are phenomenologically similar to our first two benchmarks: i) near the SM

values but with slight enhanced a_1 and suppressed c_1 around $(a_1, c_1) = (1.1, 0.8)$, and *ii*) a flipped region where c_1 is negative and a_1 is slightly suppressed around $(a_1, c_1) = (0.8, -0.7)$. The third and final benchmark *iii*) is a fermiophobic example with enhanced $a_1 \sim 1.4$, which is of interest even if not experimentally favored. In the Georgi-Machacek model and its generalizations, we showed that these regions have qualitatively different phenomenology for the partner Higgs boson h_2. In region i, h_2 has suppressed couplings and can be searched for in lower mass Higgs searches, where the Standard Model Higgs has already been ruled out, whereas in region ii, it has enhanced fermion and gauge boson couplings and should be searched for at high mass (> 600 GeV). In both of these regions, searches for h_2 decays into h_1 pairs are also motivated, since it can have a reasonable rate. In region iii, where h_1 is fermiophobic, h_2 has enhanced fermion couplings, with suppressed gauge boson couplings and thus can be picked up by both searches for heavy Higgses and top resonances.

We also briefly discussed the model-dependent effects of the nontrivial $SU(2)_C$ multiplets, which have exotic scalar signals, such as a doubly-charged Higgs. Aside from direct searches, these scalars contribute nonnegligible loop effects to the Higgs decay rate to photons. These unfortunately tend to suppress the rate and add an additional uncertainty when extracting the couplings for the Higgs boson h_1.

To conclude, if future LHC Higgs analyses indicate that the Higgs boson couplings to electroweak gauge bosons are enhanced, then it will be important to investigate theoretical frameworks that can realize such enhancements. In this paper, we have outlined some of the important correlated signals and effects in such theories by looking at the Georgi-Machacek model and its generalizations. There is a broad range of directions in which to test and confirm these theories, and it will take the

Higgs data to determine whether nature utilizes such a rich and complex mechanism of electroweak symmetry breaking.

Georgi-Machacek Model Formulas

In this appendix, we list details about the Georgi-Machacek model and its generalizations. The potential for the Higgs fields can be written as [52]

$$\begin{aligned} V &= \lambda_1 \left(\mathrm{Tr}\,\phi^\dagger\phi - \cos^2\theta_H v^2\right)^2 + \lambda_2 \left(\mathrm{Tr}\,\chi^\dagger\chi - \frac{3}{8}\sin^2\theta_H v^2\right)^2 \\ &\quad +\lambda_3 \left(\mathrm{Tr}\,\phi^\dagger\phi - \cos^2\theta_H v^2 + \mathrm{Tr}\,\chi^\dagger\chi - \frac{3}{8}\sin^2\theta_H v^2\right)^2 \\ &\quad +\lambda_4 \left[\mathrm{Tr}\,\phi^\dagger\phi\,\mathrm{Tr}\,\chi^\dagger\chi - 2\sum_{ij}\mathrm{Tr}\left(\phi^\dagger\tau_i\phi\tau_j\right)\mathrm{Tr}\left(\chi^\dagger T_i\chi T_j\right)\right] \\ &\quad +\lambda_5 \left[3\,\mathrm{Tr}\,\chi^\dagger\chi\chi^\dagger\chi - \left(\mathrm{Tr}\,\chi^\dagger\chi\right)^2\right]. \end{aligned} \tag{2.9}$$

Here the τ_i, T_i are the $SU(2)$ generators for a doublet and triplet. This has a natural extension to χ of higher representation, $(r,\bar{r}) = (2j+1, \overline{2j+1})$. This changes the factor of $\frac{3}{8}$ in λ_{1-3} to $\frac{3}{4j(j+1)}$, the factor of 2 in λ_4 to $\frac{4}{j(j+1)}$, and the factor of 3 in λ_5 to $(2j+1)$.

Using this potential, for the GM model, the masses of the $SU(2)_C$ multiplets are

$$\begin{aligned} m^2_{H_1,H_1'} &= \begin{pmatrix} 8\cos^2\theta_H(\lambda_1+\lambda_3) & \sqrt{6}\sin 2\theta_H\lambda_3 \\ \sqrt{6}\sin 2\theta_H\lambda_3 & 3\sin^2\theta_H(\lambda_2+\lambda_3) \end{pmatrix} v^2 \\ m^2_{H_3} &= \lambda_4 v^2, \quad m^2_{H_5} = 3(\lambda_4\cos^2\theta_H + \lambda_5\sin^2\theta_H)v^2. \end{aligned} \tag{2.10}$$

We can also determine the Feynman rules for the triple Higgs scalar couplings. Here, we list a few relevant ones for $h_2 \to 2h_1$ decays and H_1, H_1' decays to photons, leaving

out a factor of i:

$$\begin{aligned}
H_1H_1H_1 &= -24\cos\theta_H(\lambda_1+\lambda_3)v \\
H_1H_1'H_1' &= -8\cos\theta_H\lambda_3 v \\
H_1H_1H_1' &= -2\sqrt{6}\sin\theta_H\lambda_3 v \\
H_1'H_1'H_1' &= -6\sqrt{6}\sin\theta_H(\lambda_2+\lambda_3)v \\
H_1H_3^+H_3^- &= -8\cos\theta_H(\sin^2\theta_H\lambda_1+\lambda_3+\lambda_4)v \\
H_1H_5^+H_5^- &= -8\cos\theta_H\left(\lambda_3+\frac{3}{4}\lambda_4\right)v \\
H_1'H_3^+H_3^- &= -2\sqrt{6}\sin\theta_H\left(\cos^2\theta_H\lambda_2+\lambda_3+\frac{2}{3}\lambda_4\right)v \\
H_1'H_5^+H_5^- &= -2\sqrt{6}\sin\theta_H(\lambda_2+\lambda_3+2\lambda_5)v.
\end{aligned} \tag{2.11}$$

The couplings for the H_5^{++} are the same as those of H_5^+ as expected from $SU(2)_C$ symmetry. Note that we have corrected some of the expressions in [52].

For the generalized GM model, the masses of the $SU(2)_C$ multiplets in the singlet and spin $2j$ sector are:

$$\begin{aligned}
m^2_{H_1,H_1'} &= \begin{pmatrix} 8\cos^2\theta_H(\lambda_1+\lambda_3) & \sqrt{\frac{12}{j(j+1)}}\sin 2\theta_H\lambda_3 \\ \sqrt{\frac{12}{j(j+1)}}\sin 2\theta_H\lambda_3 & \frac{6}{j(j+1)}\sin^2\theta_H(\lambda_2+\lambda_3) \end{pmatrix} v^2 \\
m^2_{H_{4j+1}} &= \frac{2(j(2j+1)\lambda_4\cos^2\theta_H+3\lambda_5\sin^2\theta_H)}{j(j+1)}v^2.
\end{aligned} \tag{2.12}$$

For the triple Higgs scalar couplings, we focus on the couplings of H_1, H_1' to the highest charged multiplet H_{4j+1} which has a maximum charged state of charge $2j$.

Again, leaving out a factor of i, the Feynman rules are:

$$\begin{aligned} H_1 H^+_{4j+1} H^-_{4j+1} &= -8\cos\theta_H \left[\lambda_3 + \frac{(2j+1)}{2(j+1)}\lambda_4\right] v \\ H_1^{'} H^+_{4j+1} H^-_{4j+1} &= -\frac{4\sqrt{3}}{\sqrt{j(j+1)}} \sin\theta_H (\lambda_2 + \lambda_3 + 2\lambda_5) v. \end{aligned} \tag{2.13}$$

The couplings for the other charged states in H_{4j+1} are the same as those of H^+_{4j+1} from $SU(2)_C$ symmetry.

CHAPTER III

IDM

This chapter is work done by myself, Spencer Chang, and Gabriel Barello [30].

Introduction

Dark matter direct detection experiments are an ambitious effort to observe galactic dark matter scattering off of nuclear targets [73] as a means to study dark matter's interactions with normal matter. Beginning with the early experiments in the eighties, there has been steady progress to increasing sensitivity. Planned experiments in the future will push this frontier [22], giving us hope that such interactions will be confirmed soon. Such a discovery would give important insights into the fundamental nature of dark matter and its place in the Standard Model of particle physics.

The experimental challenges of direct detection are many. Finding conclusive evidence is a tall order, as demonstrated by several recent experimental anomalies, the most famous being the annual modulation signal seen by DAMA [29], which appear to be in conflict with the null results of other experiments. However, whether a dark matter scenario is consistent with existing limits and excesses depends strongly on the form of its interactions with the nucleus. For each interaction, the relative sensitivities of different experiments can vary wildly, leading to the hope of a scenario consistent with all of the existing data. Another reason to study the allowed interactions is that certain interactions may have distinctive features in the signal that allow better background separation. These reasons highlight the importance of exploring the full landscape of possible interactions. Some examples of the studied possibilities

include inelastic transitions [74], dark matter form factors [75, 76], dark matter-nucleus resonances [77, 78], and isospin-violating dark matter [79–81].

Given the large range of possible scattering interactions allowed by dark matter theories, it has proven useful to study the phenomenology of dark matter scattering in a model independent fashion [32, 82]. In particular, Ref. [32] has provided a systematic study of the effective description of nonrelativistic, elastic scattering and a Mathematica package to generate the necessary form factors [33]. A notable success of this approach was the illumination of nuclear responses beyond the standard spin-independent and spin-dependent responses that are primarily considered by dark matter experiments. Thus, model independent approaches have the benefit of larger applicability, pointing out all of the regions where experiments can be sensitive — see [83–88] for some recent work in this direction.

In this paper, we extend this work by considering the modifications necessary to describe inelastic transitions of the dark matter particle. Such transitions have important kinematic effects and were originally proposed and studied for scattering to a heavier dark matter state [31, 74] and then later extended to the "down scattering" case [89–91]. We will investigate the modifications to Ref. [32] that must be made to properly treat inelastic scattering in a model-independent fashion. As we will show, this requires a straightforward reorganization of the basis of scattering matrix-elements. This has the added benefit that we were able to suitably modify the Mathematica package [33] to calculate the form factors for inelastic scattering.

To illustrate the utility of this methodology, we will demonstrate how the inelastic transitions between particles of spin 1/2 to 1/2, 0 to 1, and 0 to 0 can be treated in a standard basis of nonrelativistic matrix elements. We do so by considering the relativistic operators between such particles that can be mediated by spin 0 or

1 particles. Using these results, we perform a reanalysis of the magnetic inelastic dark matter scenario [34] and perform a model independent scan over the relativistic operators to determine scenarios which could explain the DAMA/LIBRA signal. For the magnetic inelastic dark matter scenario and for operators which couple the dark matter to protons only, we find the constraints from xenon detectors can be weakened to allow some operators to survive, while germanium detectors have an extremely weak sensitivity. However, a stringent constraint comes from iodine targets, like those used by COUPP and KIMS. A large uncertainty in this analysis is the quenching factor of iodine. Depending on the values we assume, the constraints from KIMS, XENON, and LUX can change by a large amount, due to changes in the recoil spectra. Another uncertainty is the lack of form factors for cesium and tungsten. Given these uncertainties, we find that DAMA explanations are constrained but not ruled out yet, which should be resolved by the next round of experimental releases.

The outline of the rest of the paper is as follows. In section 3.2, we discuss the kinematics of inelastic scattering to determine the relevant kinematic variables. In section 3.3 we discuss the modifications to the operators needed to describe dark matter inelastic transitions. In section 3.4, as an application of this formalism, we fit the annual modulation signal at DAMA/LIBRA and discuss the constraints from other experiments. In section 3.5, we conclude. Finally, in the appendices, we give further details on the nonrelativistic limit of the kinematics and matrix elements of inelastic scattering.

Variables for Inelastic Kinematics

To begin, we need to determine the correct variables to describe inelastic scattering. To do so, we need to understand the kinematic modifications of an inelastic

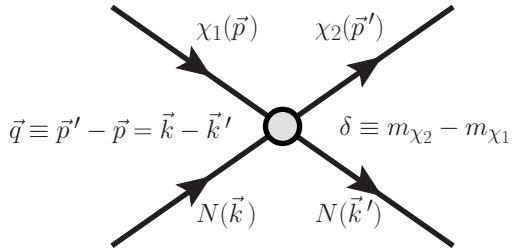

FIGURE 11. Schematic for IDM.
Inelastic scattering of dark matter off of a nucleon with our conventions for the kinematic variables.

transition for nonrelativistic scattering. We are interested in scattering events of the type

$$\chi_1(\vec{p})\ N(\vec{k}\,) \to \chi_2(\vec{p}\,')\ N(\vec{k}\,') \tag{3.1}$$

where χ_1 is the incoming dark matter particle, χ_2 is the outgoing particle, and N is a nucleon in the target nucleus, see Fig. 11. There is a mass splitting between the two particles $\delta = m_{\chi_2} - m_{\chi_1}$. Positive δ was the first case to be considered originally [74], which pointed out that this has the important effects of favoring scattering off of heavier nuclei and increasing the annual modulation fraction. Negative δ leads to exothermic transitions which have also been considered in the literature [89–91]. In certain theories, the elastic scattering process is forbidden or suppressed [92, 93], making these inelastic transitions the leading way to detect dark matter scattering. For a survey of such theories, see [74, 94–98].

The modifications of a nonzero splitting δ on the kinematics is straightforward. To leading order in the nonrelativistic expansion, δ is the additional energy required to make the transition occur. Thus, given the scaling of kinetic energy, we expect situations where the splitting scales as $\delta \sim O(v^2)$ to have a consistent velocity

expansion. Since dark matter in our galaxy have speeds $v \sim 10^{-3}c$, this means that we should consider splittings in the range $\delta \sim 100$ keV $\left(\frac{m_\chi}{100 \text{ GeV}}\right)$.

Now, we adapt the analysis of [32] to inelastic scattering in order to determine the relevant degrees of freedom that characterize the effective theory in a velocity expansion. One approach would be to start with the relativistic kinematics and take the nonrelativistic limit. Although this gives the same result, as we show in Appendix 3.A, we find that it is simpler to proceed from the constraints of Galilean invariance where velocities receive a common shift. This determines that there are two relevant vectors that are boost invariant, $\vec{v} \equiv \vec{v}_{\chi_1} - \vec{v}_{N_{in}} = \vec{p}/m_{\chi_1} - \vec{k}/m_N$ and $\vec{q} = \vec{p}\,' - \vec{p} = \vec{k} - \vec{k}'$, while the boost invariant scalars are the particle masses and δ. Note that $\vec{p}\,' - \vec{p}$ is not exactly Galilean invariant; due to the mass difference δ, it is invariant to leading order in the velocity expansion and thus is a consistent approximation at first order. Throughout this discussion, we are working in this expansion and will cavalierly use equalities for expressions if they are equal to the same order in the expansion.

At this point, it is useful to construct an orthogonal basis of these vectors. To do so, consider the scattering in the center-of-mass frame, where $\vec{v}_{\chi_1} = \frac{\mu_N}{m_{\chi_1}}\vec{v}$, $\vec{v}_{N_{in}} = -\frac{\mu_N}{m_N}\vec{v}$, and μ_N is the reduced mass between χ_1 and N. The initial energy in this frame, expanded to second order in velocities, is

$$E_{in} \approx m_{\chi_1} + m_N + \frac{1}{2}\mu_N v^2. \tag{3.2}$$

After scattering, the momentum vectors are $\vec{p}' = \vec{p} + \vec{q}$ and $\vec{k}' = \vec{k} - \vec{q}$. Expanding the final energy to the same order, we find

$$\begin{aligned} E_{out} &= m_{\chi_2} + m_N + \frac{1}{2m_{\chi_2}}|\vec{p} + \vec{q}|^2 + \frac{1}{2m_N}|\vec{k} - \vec{q}|^2 \\ &\approx E_{in} + \delta + \vec{v} \cdot \vec{q} + \frac{|\vec{q}|^2}{2\mu_N}. \end{aligned} \tag{3.3}$$

To reach the final form, we treated all momenta as order v and δ as order v^2. Thus, we find that energy conservation requires

$$\delta + \vec{v} \cdot \vec{q} + \frac{|\vec{q}|^2}{2\mu_N} = 0. \tag{3.4}$$

Using this constraint, one can easily show that

$$\vec{v}^{\perp}_{\text{inel}} \equiv \vec{v} + \frac{\vec{q}}{2\mu_N} + \frac{\delta}{|\vec{q}|^2}\vec{q} = \vec{v}^{\perp}_{\text{el}} + \frac{\delta}{|\vec{q}|^2}\vec{q} \tag{3.5}$$

is perpendicular to $\vec{q}$. Here we see that the inelastic kinematics alters this vector from the elastic version $\vec{v}^{\perp}_{\text{el}}$ by a new piece proportional to δ. This new term is entirely consistent with the velocity expansion.

As a consistency check, notice that Eq. 3.4 requires

$$|\vec{v}| \geq \frac{1}{|\vec{q}|}\left|\frac{|\vec{q}|^2}{2\mu_N} + \delta\right|. \tag{3.6}$$

If we write the momentum transfer in terms of the energy recoil $|\vec{q}| = \sqrt{2m_N E_R}$, we find that the minimum velocity for scattering is

$$v_{\text{min}} = \frac{1}{\sqrt{2m_N E_R}}\left|\frac{m_N E_R}{\mu_N} + \delta\right| \tag{3.7}$$

which reproduces the well known result in the literature [74].

Inelastic Scattering Operators

Now that we know the correct variables to describe inelastic kinematics, we can list the allowed matrix elements for inelastic, nonrelativistic dark matter-nucleon scattering. To leading order in the velocity expansion, we found that the only modification is that $\vec{v}^{\perp}$ is changed from the elastic case. Thus, the operators that are allowed are the same as in [32] with $\vec{v}^{\perp} \to \vec{v}^{\perp}_{\text{inel}}$. Listing these in the same numbering scheme, we have

$$
\begin{aligned}
&\mathcal{O}_1 = \mathbf{1}_\chi \mathbf{1}_N, \quad \mathcal{O}_2 = (v^{\perp}_{\text{inel}})^2, \quad \mathcal{O}_3 = i\vec{S}_N \cdot \left(\frac{\vec{q}}{m_N} \times \vec{v}^{\perp}_{\text{inel}} \right), \\
&\mathcal{O}_4 = \vec{S}_\chi \cdot \vec{S}_N, \quad \mathcal{O}_5 = i\vec{S}_\chi \cdot \left(\frac{\vec{q}}{m_N} \times \vec{v}^{\perp}_{\text{inel}} \right), \\
&\mathcal{O}_6 = \left(\vec{S}_\chi \cdot \frac{\vec{q}}{m_N} \right) \left(\vec{S}_N \cdot \frac{\vec{q}}{m_N} \right), \\
&\mathcal{O}_7 = \vec{S}_N \cdot \vec{v}^{\perp}_{\text{inel}}, \quad \mathcal{O}_8 = \vec{S}_\chi \cdot \vec{v}^{\perp}_{\text{inel}}, \\
&\mathcal{O}_9 = i\vec{S}_\chi \cdot \left(\vec{S}_N \times \frac{\vec{q}}{m_N} \right), \quad \mathcal{O}_{10} = i\vec{S}_N \cdot \frac{\vec{q}}{m_N}, \\
&\mathcal{O}_{11} = i\vec{S}_\chi \cdot \frac{\vec{q}}{m_N}, \quad \mathcal{O}_{12} = \vec{S}_\chi \cdot \left(\vec{S}_N \times \vec{v}^{\perp}_{\text{inel}} \right), \\
&\mathcal{O}_{13} = i \left(\vec{S}_\chi \cdot \vec{v}^{\perp}_{\text{inel}} \right) \left(\vec{S}_N \cdot \frac{\vec{q}}{m_N} \right), \\
&\mathcal{O}_{14} = i \left(\vec{S}_\chi \cdot \frac{\vec{q}}{m_N} \right) \left(\vec{S}_N \cdot \vec{v}^{\perp}_{\text{inel}} \right), \\
&\mathcal{O}_{15} = - \left(\vec{S}_\chi \cdot \frac{\vec{q}}{m_N} \right) \left((\vec{S}_N \times \vec{v}^{\perp}_{\text{inel}}) \cdot \frac{\vec{q}}{m_N} \right),
\end{aligned}
\tag{3.8}
$$

where $\vec{S}_{\chi,N}$ are the spin operators for the dark matter and nucleon. In [32], operator $\mathcal{O}_2$ was not considered since it doesn't appear in the nonrelativistic reduction of the scattering matrix elements of relativistic operators, and we find the same result here.

Thus, the important operators are at most linear in $\vec{v}^{\perp}_{\text{inel}}$. Since $\vec{v}^{\perp}_{\text{inel}}$ differs from the elastic $\vec{v}^{\perp}$ by just a shift in $\vec{q}$, we will later find that this linearity allows one to utilize the form factors provided by the Mathematica package [33].

There are two other modifications to the elastic case that we will find. First of all, δ can be a coefficient multiplying the operators when one reduces from relativistic operators. The second effect is that $\vec{q}$ no longer has to appear in the combination of $i\vec{q}$, as can be seen by the expression for $\vec{v}^{\perp}_{\text{inel}}$. In the elastic case, this was guaranteed by the interaction being Hermitian. Since conjugation swaps initial and final states, this acts as time reversal, $i\vec{q} \xrightarrow{T} i\vec{q}$. However, for the inelastic case, the initial and final states are not the same particle, so this is no longer required by the interaction. In general, the inelastic operators in Eq. 3.8 may have arbitrary complex coefficients, as long as they appear in appropriate Hermitian conjugate pairs in the Hamiltonian. This was not the case for elastic operators because Hermiticity requires them to have real coefficients.

Form Factors for Inelastic Scattering

Now, one must use these nucleon-dark matter operators to determine the matrix elements within the target nucleus. We will give a brief summary here, giving more details in Appendix 3.C. Since inelasticity modifies $\vec{v}^{\perp}_{\text{inel}}$, we should examine how this affects the nuclear response. First of all, by introducing the target velocity $\vec{v}_T$, we

rewrite

$$\begin{aligned}
\vec{v}_{\rm el}^{\perp} &= \vec{v} + \frac{\vec{q}}{2\mu_N} \\
&= \left(\frac{\vec{p}}{m_{\chi_1}} - \frac{\vec{k}}{m_N}\right) + \frac{1}{2m_{\chi_1}}\left(\vec{p}' - \vec{p}\right) + \frac{1}{2m_N}\left(\vec{k} - \vec{k}'\right) \\
&\approx \frac{1}{2}(\vec{v}_{\chi_1} + \vec{v}_{\chi_2} - \vec{v}_{N_{in}} - \vec{v}_{N_{out}}) \\
&= \frac{1}{2}(\vec{v}_{\chi_1} + \vec{v}_{\chi_2} - \vec{v}_{T_{in}} - \vec{v}_{T_{out}}) \\
&\quad + \frac{1}{2}\left[(\vec{v}_{T_{in}} - \vec{v}_{N_{in}}) + (\vec{v}_{T_{out}} - \vec{v}_{N_{out}})\right] \\
&\equiv \vec{v}_{{\rm el}\,T}^{\perp} + \vec{v}_{\rm nuc}.
\end{aligned} \tag{3.9}$$

Thus for each nucleon in the nucleus, $\vec{v}_{\rm el}^{\perp}$ is equal to the target's $\vec{v}_{\rm el}^{\perp}$ plus a term, $\vec{v}_{\rm nuc}$, that is dependent on the nucleon's relative velocity to the nucleus, also known as Fermi motion. Similarly, for the inelastic velocity, we have

$$\vec{v}_{\rm inel}^{\perp} = \vec{v}_{{\rm inel}\,T}^{\perp} + \vec{v}_{\rm nuc} \tag{3.10}$$

where

$$\vec{v}_{{\rm inel}\,T}^{\perp} = \frac{1}{2}(\vec{v}_{\chi_1} + \vec{v}_{\chi_2} - \vec{v}_{T_{in}} - \vec{v}_{T_{out}}) + \frac{\delta}{|\vec{q}|^2}\vec{q}, \tag{3.11}$$

Since the nucleus and dark matter scattering is also in the nonrelativistic limit, the same kinematic considerations from before show that $\vec{v}_{{\rm inel}\,T}^{\perp}$ is perpendicular to $\vec{q}$ and thus we can now interpret $\vec{q}$ as the momentum transfer from χ_1 to the target *nucleus*.

The reason for the separation of $\vec{v}_{{\rm inel}\,T}^{\perp}$ into target and relative parts is that the nuclear form-factors only depend on interactions with *nucleons*, so only $\vec{v}_{\rm nuc}$ is an operator. The five nucleon interactions are [32]:

$$\begin{aligned}
&\mathcal{O}_1^N = \mathbf{1}_N, \qquad \mathcal{O}_2^N = -2\vec{v}_{\rm nuc}\cdot\vec{S}_N, \\
&\vec{\mathcal{O}}_3^N = 2\vec{S}_N, \qquad \vec{\mathcal{O}}_4^N = -\vec{v}_{\rm nuc}, \text{ and} \\
&\vec{\mathcal{O}}_5^N = 2i\vec{v}_{\rm nuc}\times\vec{S}_N.
\end{aligned} \tag{3.12}$$

which correspond to different types of nucleon responses. $\mathcal{O}_1^N$ corresponds to the charge interaction, $\mathcal{O}_2^N$ to the axial charge interaction, $\vec{\mathcal{O}}_3^N$ to the axial vector interaction, $\vec{\mathcal{O}}_4^N$ to the vector magnetic interaction, and $\vec{\mathcal{O}}_5^N$ to the vector electric interaction. Note that the explicit dependence on the inelastic nature of the scattering is not in the operators but in the coefficients. For a more detailed discussion of the nuclear form factors see [32].

For our cases, since $\vec{v}_{\rm inel}^{\perp}$ only appears linearly (see Tables 1-4), we merely have to incorporate the change of $\vec{v}_{{\rm el}\,T}^{\perp} \to \vec{v}_{{\rm inel}\,T}^{\perp}$ in the Mathematica notebook [33]. In calculating the matrix elements squared, this results in terms which are proportional to $|\vec{v}_{{\rm inel}\,T}^{\perp}|^2$. This has the simple form

$$\begin{aligned}
|\vec{v}_{{\rm inel}\,T}^{\perp}|^2 &= |\vec{v}_T|^2 - \left(\frac{1}{2\mu_T} + \frac{\delta}{|\vec{q}|^2}\right)^2 |\vec{q}|^2 \\
&= |\vec{v}_T|^2 - v_{{\rm min}\,T}^2
\end{aligned} \tag{3.13}$$

where $\vec{v}_T = \vec{v}_{\chi_1} - \vec{v}_{T_{in}}$ and μ_T is the χ_1-nucleus reduced mass. In the second form, we have written the subtracted term as $v_{{\rm min}\,T}$, the minimum speed to scatter off of the nucleus with energy E_R, which is the nucleus version of Eq. 3.7. Note that for upscattering ($\delta > 0$) this leads to a suppression of this factor and for both signs of δ, this term goes to zero at the minimum incoming velocity.

The power of this formalism is that it gives the correct variables in which to characterize inelastic scattering and thus is helpful for understanding results that are at first surprising. As an example, in Ref. [34], an inelastic dark matter model was analyzed that had a magnetic dipole interaction with the nucleus. For the scattering of this dark matter dipole off of the nucleus charge, peculiar terms involving $\delta/|\vec{v}|^2, \delta/E_R$ are found. In that paper, these terms were only discovered by a systematic expansion. However, in terms of this discussion, these terms are just due to the contribution from the δ dependent terms of $|\vec{v}^{\perp}_{\text{inel}\,T}|^2$. Of course, the main improvement on Ref. [34] is that the form factors can now be reliably computed by a modification of the Mathematica notebook [33]. Again, for details on how to implement these inelastic modifications to the form factor calculation, see Appendix 3.C.

Relativistic Matrix Elements for Fermion-Fermion Inelastic Transitions

As a first application of this formalism, let's analyze the case where $\chi_{1,2}$ are both spin 1/2 fermions. We start with the relativistic operators that would generate such scattering off of a nucleon. We list the same twenty operators of [33] in Tables 1 and 2 for inelastic scattering [1]. Factors of $1/m_M$ are added to get the correct mass dimension, where m_M is a proxy for the mass of the mediator for the interaction. This coefficient involves powers of the UV coupling strength and can have strong q^2 dependence, especially if the mediator is light or massless. Factors of i are set up so that if $\Psi_2 = \Psi_1$, the operator is Hermitian, thus allowing a convenient comparison to the elastic case by taking $\delta = 0$. The third column is the nonrelativistic limit of the matrix element after multiplying by $1/(4m_N m_\chi)$ to get to standard nonrelativistic

[1] Our operator 20 has one less factor of i due to a typo in [33].

normalization. This matrix element is then decomposed in the final column in the basis of the fifteen nonrelativistic operators of Eq. 3.8.

Index	Relativistic Operator	Nonrelativistic Limit $\times \frac{1}{4m_N m_\chi}$	$\sum_i c_i \mathcal{O}_i$
1	$\bar{\chi}_2\chi_1\bar{N}N$	$\mathbf{1}_\chi \mathbf{1}_N$	$\mathcal{O}_1$
2	$i\bar{\chi}_2\chi_1\bar{N}\gamma^5 N$	$i\frac{\vec{q}}{m_N}\cdot\vec{S}_N$	$\mathcal{O}_{10}$
3	$i\bar{\chi}_2\gamma^5\chi_1\bar{N}N$	$-i\frac{\vec{q}}{m_\chi}\cdot\vec{S}_\chi$	$-\frac{m_N}{m_\chi}\mathcal{O}_{11}$
4	$\bar{\chi}_2\gamma^5\chi_1\bar{N}\gamma^5 N$	$-(\frac{\vec{q}}{m_\chi}\cdot\vec{S}_\chi)(\frac{\vec{q}}{m_N}\cdot\vec{S}_N)$	$-\frac{m_N}{m_\chi}\mathcal{O}_6$
5	$\bar{\chi}_2\gamma^\mu\chi_1\bar{N}\gamma_\mu N$	$\mathbf{1}_\chi \mathbf{1}_N$	$\mathcal{O}_1$
6	$\bar{\chi}_2\gamma^\mu\chi_1\bar{N}i\sigma_{\mu\nu}\frac{q^\nu}{m_M}N$	$\frac{\vec{\lvert q\rvert}^2}{2m_N m_M}\mathbf{1}_\chi\mathbf{1}_N$ $+2\left(\frac{\vec{q}}{m_\chi}\times\vec{S}_\chi + i\vec{v}^\perp_{\rm inel}\right)\cdot\left(\frac{\vec{q}}{m_M}\times\vec{S}_N\right)$	$\frac{\vec{\lvert q\rvert}^2}{2m_N m_M}\left(\mathcal{O}_1+\frac{4m_N}{m_\chi}\mathcal{O}_4\right)$ $-\frac{2m_N}{m_M}\left(\frac{m_N}{m_\chi}\mathcal{O}_6+\mathcal{O}_3\right)$
7	$\bar{\chi}_2\gamma^\mu\chi_1\bar{N}\gamma_\mu\gamma^5 N$	$-2\vec{S}_N\cdot(\vec{v}^\perp_{\rm inel}-\frac{\delta}{\vec{\lvert q\rvert}^2}\vec{q})$ $+2i\vec{S}_\chi\cdot(\vec{S}_N\times\frac{\vec{q}}{m_\chi})$	$-2\left(\mathcal{O}_7+i\frac{m_N\delta}{\vec{\lvert q\rvert}^2}\mathcal{O}_{10}-\frac{m_N}{m_\chi}\mathcal{O}_9\right)$
8	$i\bar{\chi}_2\gamma^\mu\chi_1\bar{N}i\sigma_{\mu\nu}\frac{q^\nu}{m_M}\gamma^5 N$	$2i\frac{\vec{q}}{m_M}\cdot\vec{S}_N$	$\frac{2m_N}{m_M}\mathcal{O}_{10}$
9	$\bar{\chi}_2 i\sigma^{\mu\nu}\frac{q_\nu}{m_M}\chi_1\bar{N}\gamma_\mu N$	$-\frac{\vec{\lvert q\rvert}^2}{2m_\chi m_M}\mathbf{1}_\chi\mathbf{1}_N$ $-2\left(\frac{\vec{q}}{m_N}\times\vec{S}_N + i\vec{v}^\perp_{\rm inel}\right)\cdot\left(\frac{\vec{q}}{m_M}\times\vec{S}_\chi\right)$	$-\frac{\vec{\lvert q\rvert}^2}{2m_\chi m_M}\left(\mathcal{O}_1+\frac{4m_\chi}{m_N}\mathcal{O}_4\right)$ $+\frac{2m_N}{m_M}\left(\mathcal{O}_6+\mathcal{O}_5\right)$
10	$\bar{\chi}_2 i\sigma^{\mu\nu}\frac{q_\nu}{m_M}\chi_1\bar{N}i\sigma_{\mu\alpha}\frac{q^\alpha}{m_M}N$	$4\left(\frac{\vec{q}}{m_M}\times\vec{S}_\chi\right)\cdot\left(\frac{\vec{q}}{m_M}\times\vec{S}_N\right)$	$\frac{4m_N^2}{m_M^2}\left(\frac{\vec{\lvert q\rvert}^2}{m_N^2}\mathcal{O}_4-\mathcal{O}_6\right)$

TABLE 1. Relativistic operators I.

Relativistic operators for inelastic transitions between two fermions $\chi_{1,2}$, their matrix element in the nonrelativistic limit multiplied by a factor of $1/(4m_\chi m_N)$, and their expansion in the basis of allowed scattering matrix-elements.

11	$\bar{\chi}_2 i\sigma^{\mu\nu}\frac{q_\nu}{m_M}\chi_1\bar{N}\gamma_\mu\gamma^5 N$	$4i\left(\frac{\vec{q}}{m_M}\times\vec{S}_\chi\right)\cdot\vec{S}_N$	$\frac{4m_N}{m_M}\mathcal{O}_9$
12	$i\bar{\chi}_2 i\sigma^{\mu\nu}\frac{q_\nu}{m_M}\chi_1\bar{N}i\sigma_{\mu\alpha}\frac{q^\alpha}{m_M}\gamma^5 N$	$-\left[i\frac{\vec{\lvert q\rvert}^2}{m_\chi m_M}-4\vec{v}^\perp_{\rm inel}\cdot\left(\frac{\vec{q}}{m_M}\times\vec{S}_\chi\right)\right]\frac{\vec{q}}{m_M}\cdot\vec{S}_N$	$-\frac{\vec{\lvert q\rvert}^2}{m_M^2}\left(\frac{m_N}{m_\chi}\mathcal{O}_{10}+4\mathcal{O}_{12}\right)$ $-\frac{4m_N^2}{m_M^2}\mathcal{O}_{15}$
13	$\bar{\chi}_2\gamma^\mu\gamma^5\chi_1\bar{N}\gamma_\mu N$	$2\left(\vec{v}^\perp_{\rm inel}-\frac{\delta}{\vec{\lvert q\rvert}^2}\vec{q}\right)\cdot\vec{S}_\chi$ $+2i\vec{S}_\chi\cdot\left(\vec{S}_N\times\frac{\vec{q}}{m_N}\right)$	$2\left(\mathcal{O}_8+\mathcal{O}_9+i\frac{m_N\delta}{\vec{\lvert q\rvert}^2}\mathcal{O}_{11}\right)$
14	$\bar{\chi}_2\gamma^\mu\gamma^5\chi_1\bar{N}i\sigma_{\mu\nu}\frac{q^\nu}{m_M}N$	$4i\vec{S}_\chi\cdot\left(\frac{\vec{q}}{m_M}\times\vec{S}_N\right)$	$-\frac{4m_N}{m_M}\mathcal{O}_9$
15	$\bar{\chi}_2\gamma^\mu\gamma^5\chi_1\bar{N}\gamma_\mu\gamma^5 N$	$-4\vec{S}_\chi\cdot\vec{S}_N$	$-4\mathcal{O}_4$
16	$i\bar{\chi}_2\gamma^\mu\gamma^5\chi_1\bar{N}i\sigma_{\mu\nu}\frac{q^\nu}{m_M}\gamma^5 N$	$4i\frac{\vec{q}}{m_M}\cdot\vec{S}_N\left(\vec{v}^\perp_{\rm inel}-\frac{\delta}{\vec{\lvert q\rvert}^2}\vec{q}\right)\cdot\vec{S}_\chi$	$\frac{4m_N}{m_M}\left(\mathcal{O}_{13}-i\frac{m_N\delta}{\vec{\lvert q\rvert}^2}\mathcal{O}_6\right)$
17	$i\bar{\chi}_2 i\sigma^{\mu\nu}\frac{q_\nu}{m_M}\gamma^5\chi_1\bar{N}\gamma_\mu N$	$2i\frac{\vec{q}}{m_M}\cdot\vec{S}_\chi$	$\frac{2m_N}{m_M}\mathcal{O}_{11}$
18	$i\bar{\chi}_2 i\sigma^{\mu\nu}\frac{q_\nu}{m_M}\gamma^5\chi_1\bar{N}i\sigma_{\mu\alpha}\frac{q^\alpha}{m_M}N$	$\vec{S}_\chi\cdot\frac{\vec{q}}{m_M}\left[i\frac{\vec{\lvert q\rvert}^2}{m_N m_M}-4\vec{v}^\perp_{\rm inel}\cdot(\frac{\vec{q}}{m_M}\times\vec{S}_N)\right]$ $-4\frac{\delta}{m_M}\vec{S}_\chi\cdot(\frac{\vec{q}}{m_M}\times\vec{S}_N)$	$\frac{m_N^2}{m_M^2}\left(\frac{\vec{\lvert q\rvert}^2}{m_N^2}\mathcal{O}_{11}+4\mathcal{O}_{15}\right)$ $-i\frac{4m_N\delta}{m_M^2}\mathcal{O}_9$
19	$i\bar{\chi}_2 i\sigma^{\mu\nu}\frac{q_\nu}{m_M}\gamma^5\chi_1\bar{N}\gamma_\mu\gamma^5 N$	$-4i\frac{\vec{q}}{m_M}\cdot\vec{S}_\chi\left(\vec{v}^\perp_{\rm inel}-\frac{\delta}{\vec{\lvert q\rvert}^2}\vec{q}\right)\cdot\vec{S}_N$ $-i\frac{4\delta}{m_M}\vec{S}_\chi\cdot\vec{S}_N$	$-\frac{4m_N}{m_M}\left(\mathcal{O}_{14}-i\frac{m_N\delta}{\vec{\lvert q\rvert}^2}\mathcal{O}_6\right)$ $-i\frac{4\delta}{m_M}\mathcal{O}_4$
20	$\bar{\chi}_2 i\sigma^{\mu\nu}\frac{q_\nu}{m_M}\gamma^5\chi_1\bar{N}i\sigma_{\mu\alpha}\frac{q^\alpha}{m_M}\gamma^5 N$	$4\frac{\vec{q}}{m_M}\cdot\vec{S}_\chi\frac{\vec{q}}{m_M}\cdot\vec{S}_N$	$\frac{4m_N^2}{m_M^2}\mathcal{O}_6$

TABLE 2. Relativistic operators II.

Relativistic operators for inelastic transitions between two fermions $\chi_{1,2}$, their matrix element in the nonrelativistic limit multiplied by a factor of $1/(4m_\chi m_N)$, and their expansion in the basis of allowed scattering matrix-elements.

When calculating the matrix elements, we do not find explicit terms with $\vec{v}^{\perp}_{\rm inel}$, instead we get terms of $\vec{v}^{\perp}_{\rm el}$. This is because the additional term of $\frac{\delta}{|\vec{q}|^2}\vec{q}$ does not appear in the nonrelativistic reduction. However, many factors of $\vec{v}^{\perp}_{\rm el}$ appear as $\vec{v}^{\perp}_{\rm el}\cdot(\vec{q}\times\vec{S})$ which are equivalent to $\vec{v}^{\perp}_{\rm inel}\cdot(\vec{q}\times\vec{S})$. The other terms are of the form $\vec{v}^{\perp}_{\rm el}\cdot\vec{S}$ which we rewrite as $(\vec{v}^{\perp}_{\rm inel}-\frac{\delta}{|\vec{q}|^2}\vec{q})\cdot\vec{S}$. Writing the matrix elements in terms of $\vec{v}^{\perp}_{\rm inel}$ is convenient since it minimizes cross terms in the matrix element squared. Note that in operators 18 and 19 there are additional terms proportional to δ which are new nontrivial contributions to the scattering amplitude. Amusingly, these contributions come from terms of $\frac{\delta}{|\vec{q}|^2}\vec{q}$ dotted into $\vec{q}$, canceling the $|\vec{q}|^2$ term in the denominator. As a final check, we see that when we take $\delta = 0$ we recover the elastic results in [33].

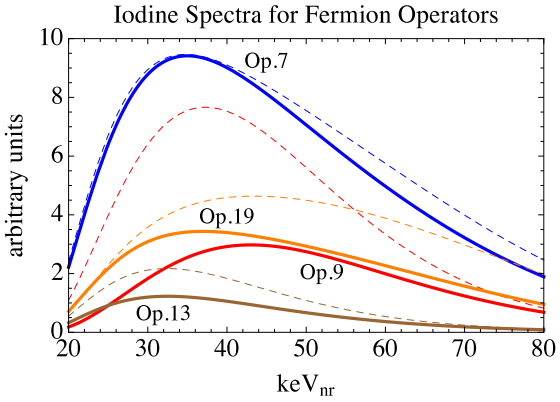

FIGURE 12. Sample iodine scattering spectra.
Sample iodine scattering spectra with equal couplings to protons and neutrons for fermion operators $7, 9, 13, 19$. The dark matter parameters are $m_\chi = 70$ GeV and $\delta = 120$ keV. In solid are our predicted curves while dashed curves show incorrect spectra from combining elastic form factors with the inelastic velocity threshold.

In Fig. 12, we plot some examples for the energy recoil spectra for these fermion operators in arbitrary units. In this figure, we are assuming iodine scattering with equal couplings to protons and neutrons with a dark matter mass $m_\chi = 70$ GeV and mass splitting $\delta = 120$ keV. In solid lines, we have our predicted rates. As a comparison, we show in dashed lines an incorrect spectra if we had taken the

elastic form factors but still integrated from the correct minimum velocity for inelastic scattering, $v_{\min T}$. Notice that the correct spectra is always smaller than the incorrect spectra for the operators considered with a positive δ. This reflects the vanishing of $|\vec{v}^{\perp}_{\text{inel}\,T}|^2$ on threshold. We chose these operators (7, 9, 13, 19) because they illustrate that the inelastic modifications to the form factors can in some cases significantly alter the shape and normalization of the spectra. In addition, we found these differences to be quite sensitive to the choice of target nuclei and isospin structure of the nucleon couplings.

Relativistic Matrix Elements for Scalar-Vector Inelastic Transitions

An additional novelty of inelastic scattering is that it allows transitions between dark matter particles of different spin. In this section, we consider the case where this transition is between a scalar Φ and a vector V^{μ}. Such nearly degenerate states have been shown to occur in models where the dark matter is composite [95, 96] due to a hyperfine splitting in the dark sector. In Table 3, we list eight Hermitian operators which can be mediated by either spin 0 or 1 mediators. For the third column, we list the matrix element's nonrelativistic limit after multiplying by a factor of $1/(2m_N)$ to go to the standard nonrelativistic normalization for the nucleons.

Index	Relativistic Operator	Nonrelativistic Limit $\times \frac{1}{2m_N}$	$\sum_i c_i \mathcal{O}_i$
1	$\frac{1}{m_M}\left(\Phi \overleftrightarrow{\partial}_\mu V^\mu\right) \bar{N} N$	$i \frac{\vec{q}}{m_M} \cdot \vec{\varepsilon}$	$\frac{m_N}{m_M} \mathcal{O}_{11}$
2	$\frac{1}{m_M} \partial_\mu (\Phi V^\mu)\, \bar{N} N$	$i \frac{\vec{q}}{m_M} \cdot \vec{\varepsilon}$	$\frac{m_N}{m_M} \mathcal{O}_{11}$
3	$\Phi V^\mu \bar{N} \gamma_\mu N$	$\frac{1}{2}\vec{\varepsilon} \cdot \left[2\vec{v}_{\rm inel}^{\perp} - \left(\frac{2m_N \delta}{\vec{\lvert q \rvert}^2} - \frac{m_N}{m_\chi}\right) \frac{\vec{q}}{m_N}\right] - i\vec{\varepsilon} \cdot (\frac{\vec{q}}{m_N} \times \vec{S}_N)$	$\mathcal{O}_8 - \mathcal{O}_9 + \frac{i}{2}\left(\frac{2m_N \delta}{\vec{\lvert q \rvert}^2} - \frac{m_N}{m_\chi}\right) \mathcal{O}_{11}$
4	$\frac{i}{m_M}\left(\Phi \overleftrightarrow{\partial}_\mu V^\mu\right) \bar{N} \gamma^5 N$	$-\frac{\vec{q}}{m_M} \cdot \vec{\varepsilon} \frac{\vec{q}}{m_N} \cdot \vec{S}_N$	$-\frac{m_N}{m_M} \mathcal{O}_6$
5	$\frac{i}{m_M} \partial_\mu (\Phi V^\mu)\, \bar{N} \gamma^5 N$	$-\frac{\vec{q}}{m_M} \cdot \vec{\varepsilon} \frac{\vec{q}}{m_N} \cdot \vec{S}_N$	$-\frac{m_N}{m_M} \mathcal{O}_6$
6	$\Phi V^\mu \bar{N} \gamma_\mu \gamma^5 N$	$-2\vec{S}_N \cdot \vec{\varepsilon}$	$-2\mathcal{O}_4$
7	$\Phi V^\mu \bar{N} i \sigma_{\mu\nu} \frac{q^\nu}{m_M} N$	$2i\vec{\varepsilon} \cdot (\frac{\vec{q}}{m_M} \times \vec{S}_N)$	$-2\frac{m_N}{m_M} \mathcal{O}_9$
8	$i\Phi V^\mu \bar{N} i \sigma_{\mu\nu} \frac{q^\nu}{m_M} \gamma^5 N$	$i\vec{\varepsilon} \cdot \left[2\vec{v}_{\rm inel}^{\perp} - \left(\frac{2m_N \delta}{\vec{\lvert q \rvert}^2} - \frac{m_N}{m_\chi}\right) \frac{\vec{q}}{m_N}\right] \frac{\vec{q}}{m_M} \cdot \vec{S}_N$	$\frac{m_N}{m_M}\left[2\mathcal{O}_{13} - i\left(\frac{2m_N \delta}{\vec{\lvert q \rvert}^2} - \frac{m_N}{m_\chi}\right) \mathcal{O}_6\right]$

TABLE 3. Relativistic operators III.

The inelastic relativistic operators for a transition from a dark matter particle of spin 0 to a spin 1 particle, $\Phi \to V^\mu$, their matrix element in the nonrelativistic limit after multiplying by a factor of $1/(2m_N)$, and then their decomposition in the basis of allowed scattering matrix elements. This final step of replacing the spin 1 polarization vector $\vec{\epsilon}$ with $\vec{S}_\chi$, is valid if we multiply the final matrix element squared by a correction factor c_{corr} in Eq. 3.16.

All of these matrix elements are in the form of $M = \vec{X} \cdot \vec{\epsilon}$, where $\vec{\epsilon}$ is the polarization vector of the spin 1 dark matter particle (which we take to be real for notational simplicity). Depending on whether the spin 1 particle is in the initial or final state, we have to average or sum over these polarizations. Since $\sum_{pol} \epsilon^i \epsilon^j = \delta^{ij}$, we have for the spin-summed (or averaged) matrix element squared

$$\overline{|M|^2} = \begin{cases} \frac{1}{3}|\vec{X}|^2 \text{ spin 1 in initial state} \\ \\ |\vec{X}|^2 \text{ spin 1 in final state} \end{cases} . \tag{3.14}$$

This form allows us to treat these matrix elements with our basis of nonrelativistic operators in the following way. If we just naively replace $\vec{\epsilon}$ with $\vec{S}_\chi$, we would have

$$\overline{|M|^2} = \frac{1}{2s_\chi + 1} \sum_{spins,i,j} S_\chi^i S_\chi^j X^{i*} X^j = \frac{s_\chi(s_\chi+1)}{3}|\vec{X}|^2. \tag{3.15}$$

Thus, we can use the same operator basis where we naively replace $\vec{\epsilon}$ with $\vec{S}_\chi$ by multiplying the final result by a correction factor

$$c_{corr} = \begin{cases} \frac{1}{s_\chi(s_\chi+1)} \text{ spin 1 in initial state} \\ \\ \frac{3}{s_\chi(s_\chi+1)} \text{ spin 1 in final state} \end{cases} . \tag{3.16}$$

Thus, in the final column of Table 3, we decompose the matrix element under this replacement of $\vec{\epsilon} \to \vec{S}_\chi$, so that we can write it in the same operator basis as the fermion case. These correction factors are accounted for in the additions we made to the Mathematica package of [33].

Relativistic Matrix Elements for Scalar-Scalar Inelastic Transitions

As one more example, we analyze the case of a dark matter scattering process with a transition from a spin 0 particle Φ_1 to another spin 0 particle Φ_2. In Table 4, we list seven operators between these two scalars which can be mediated by either spin 0 or 1 mediators. For the third column, we list the matrix element's nonrelativistic limit after multiplying by a factor of $1/(2m_N)$ to go to the standard nonrelativistic normalization for the nucleons.

Index	Relativistic Operator	Nonrelativistic Limit $\times\frac{1}{2m_N}$	$\sum_i c_i\mathcal{O}_i$
1	$\Phi_2\Phi_1\bar{N}N$	$\mathbf{1}_\chi\mathbf{1}_N$	$\mathcal{O}_1$
2	$\Phi_2\Phi_1 i\bar{N}\gamma^5 N$	$i\frac{\vec{q}}{m_N}\cdot\vec{S}_N$	$\mathcal{O}_{10}$
3	$\frac{1}{m_M}\left(i\Phi_2\overleftrightarrow{\partial}_\mu\Phi_1\right)\bar{N}\gamma^\mu N$	$2\frac{m_\chi}{m_M}\mathbf{1}_\chi\mathbf{1}_N$	$2\frac{m_\chi}{m_M}\mathcal{O}_1$
4	$\frac{1}{m_M}\left(i\Phi_2\overleftrightarrow{\partial}_\mu\Phi_1\right)\bar{N}\gamma^\mu\gamma^5 N$	$-4\frac{m_\chi}{m_M}\left(\vec{v}^\perp_{\rm inel}-\frac{\delta}{\vert\vec{q}\vert^2}\vec{q}\right)\cdot\vec{S}_N$	$-4\frac{m_\chi}{m_M}\left(\mathcal{O}_7+i\frac{m_N\delta}{\vert\vec{q}\vert^2}\mathcal{O}_{10}\right)$
5	$\frac{1}{m_M}\partial_\mu(\Phi_2\Phi_1)\,\bar{N}\gamma^\mu\gamma^5 N$	$-\frac{2i}{m_M}\vec{q}\cdot\vec{S}_N$	$-2\frac{m_N}{m_M}\mathcal{O}_{10}$
6	$\frac{1}{m_M}\left(i\Phi_2\overleftrightarrow{\partial}_\mu\Phi_1\right)Ni\sigma_{\mu\nu}\frac{q^\nu}{m_M}N$	$4i\frac{m_\chi}{m_M}\vec{v}^\perp_{\rm inel}\cdot\left(\frac{\vec{q}}{m_M}\times\vec{S}_N\right)+\frac{m_\chi}{m_N m_M^2}\vert\vec{q}\vert^2\mathbf{1}_\chi\mathbf{1}_N$	$\frac{m_\chi}{m_N m_M^2}\vert\vec{q}\vert^2\mathcal{O}_1-4\frac{m_\chi m_N}{m_M^2}\mathcal{O}_3$
7	$\frac{i}{m_M}\left(i\Phi_2\overleftrightarrow{\partial}_\mu\Phi_1\right)Ni\sigma_{\mu\nu}\gamma^5\frac{q^\nu}{m_M}N$	$4i\frac{m_\chi}{m_M}\frac{\vec{q}}{m_M}\cdot\vec{S}_N$	$4\frac{m_\chi m_N}{m_M^2}\mathcal{O}_{10}$

TABLE 4. Relativistic operators IV.

The inelastic relativistic operators for a transition between dark matter particles both of spin 0, $\Phi_1\to\Phi_2$, their matrix element in the nonrelativistic limit after multiplying by a factor of $1/(2m_N)$, and then their decomposition in the basis of allowed scattering matrix elements.

Fitting DAMA/LIBRA's annual modulation signal

In this section we present fits to the DAMA/LIBRA annual modulation signal [29]. For the following analysis we consider $\delta > 0$, which favors dark matter scattering off of heavier targets. Thus we specifically consider constraints from XENON10 [24], XENON100 [25], LUX [26], CDMS [27], COUPP [28], and KIMS [99]. Unfortunately, we cannot be inclusive in our consideration of constraints. In particular we cannot derive limits from other direct detection experiments such as CRESST ($CaWO_4$) [100] or fully analyze KIMS (CsI) which could be sensitive to the preferred parameter spaces. This is because tungsten and cesium form factors are not yet available in the Mathematica package [33], so we cannot treat them at the same level. However, KIMS most recent analysis [99] claims any scenario involving iodine scattering to explain the DAMA modulation is incompatible with their data, which considering *only* iodine scattering, is mostly accurate, but there are some exceptions. As we will demonstrate, KIMS limits are strongly dependent on the iodine quenching factors which have some large uncertainties at the moment. Given all of these caveats, we will find some allowed regions on parameter space but expect these scenarios to be tested in the near future.

Experimental Input

To analyze the direct detection signal, we take a dark matter density $\rho = 0.3$ GeV/cm^3 [101] and a Maxwell-Boltzmann velocity distribution with parameters $v_0 = 220$ km/s [102] and $v_{\rm esc} = 550$ km/s [103]. For DAMA, since inelastic kinematics favors scattering off of heavier targets, we only consider scattering off of the iodine nuclei in the NaI crystals. We calculated the shift in the best fit points due to Na for operator 2 and found only a 0.07% change in the best fit m_M, and a 0.01% shift in

χ^2, so decided not to include Na in the full analysis. We found the modulation rate for scattering off of iodine alone and determined the point in (m_χ, δ, m_M) parameter space which minimized a χ^2 fit against the DAMA/LIBRA data [29]. For our χ^2, we used the first 12 bins of their data, which corresponds to an energy range of 2-8 keV_{ee}. Later on, when we plot the 2D parameter space $(\delta, 1/m_M)$, we will show contours for $\Delta\chi^2 = 2.3, 5.99$ representing the $68, 95\%$ C. L. region for two degrees of freedom $(d.o.f.)$.

An important parameter in our fits is the quenching factor we adopt for iodine in NaI. The quenching factor Q determines the relationship between the measured energy in electron equivalents, keV_{ee}, and the original energy imparted to the nucleus keV_{nr}, $\text{keV}_{\text{ee}} = Q \times \text{keV}_{\text{nr}}$. Because of this, a good measurement of the quenching factor is necessary to determine the mass splitting and dark matter mass which best fits the DAMA/LIBRA modulation signal as well as determining the constraints from other experiments. For NaI, the value for iodine's quenching factor $Q_I = 0.09$ [104] is widely used, however a more recent paper [35] reports a measurement of $Q_I = 0.04$. We will consider both values for iodine's quenching factor in what follows and denote it by Q_{NaI}. A smaller quenching factor shifts the nuclear recoil energies that are relevant to DAMA to higher energies, so even though there is no suppression at xenon targets for scattering due to kinematics, the energy range could be outside of the acceptance range for LUX and XENON100 (this is more important for LUX as it has a smaller acceptance window). We find that a smaller quenching factor generally requires a larger value of δ to fit the DAMA data which leads to a suppression of scattering at lighter targets like the germanium at CDMS. These considerations mean that an uncertainty in the quenching factor has profound consequences for constraining signals seen in direct detection experiments.

As limits, we first consider the xenon scattering limits in recent analyses by XENON100 [25] and LUX [26]. For XENON100's analysis, there was an exposure of 7.6×10^3 kg $\cdot$ days and the acceptance we used was extracted from the hard discrimination cut of Fig. 1 in [25] used in their maximum gap analysis. This acceptance range is 2 to 43.3 $\mathrm{keV_{nr}}$, though we extended their acceptance window to 50 $\mathrm{keV_{nr}}$ assuming the acceptance didn't change in the last 6.7 $\mathrm{keV_{nr}}$. They observed two events, which we take to be all signal, giving a Poisson 90% C.L. limit of 5.32 events. LUX's analysis had 1.0×10^4 kg $\cdot$ days of exposure and used a 99.6% efficiency after a 50% NR acceptance in an energy range of 10-36 $\mathrm{keV_{nr}}$ (the low energy, 0-10 $\mathrm{keV_{nr}}$, efficiency isn't 99.6% but can be found in the efficiency curve after the single scattering requirements have been accounted for in Fig. 1 of [26]). They observed one event, which we take to be all signal, leading to a Poisson 90% C.L. limit of 3.89 events. As both XENON100 and LUX experiments were primarily searching for elastic dark matter, their energy ranges weren't conducive to a search for inelastic dark matter which favors higher nuclear recoil energies, leading to weakened sensitivities. To be sensitive to these high energy scatters, we also consider an older XENON10 analysis that was focused on inelastic dark matter [24]. This XENON10 analysis had an exposure of 316 kg $\cdot$ days, with an extended energy range of 75-250 $\mathrm{keV_{nr}}$ that has a high efficiency $\sim 32\%$, after applying software cuts and nuclear recoil acceptance. They saw no events in their extended range. Since the advantage of this analysis over the more recent xenon experiments is its extended energy range and not its exposure we chose to constrain models if they predict more than 2.3 events (the 90% C.L. limit with no observed events) in this 75-250 $\mathrm{keV_{nr}}$ range.

We looked at the constraints from CDMS inelastic dark matter search from their germanium detectors [27] as well. Due to the lighter mass of germanium relative

to xenon, we expected its limits would be suppressed relative to xenon limits. This CDMS analysis had 970 kg·days of exposure, and even with perfect acceptance the exclusions for all operators were $\gtrsim$ 1000 times weaker than the limits from the xenon experiments. Thus we decided not to include any more details for germanium detectors.

An important constraint comes from COUPP which employs a CF_3I target [28]. We considered scattering of the dark matter off of the iodine as well as the fluorine, but not the carbon as its form factor isn't available in the Mathematica package. However, due to carbon's light mass, it shouldn't give a significant contribution except for small mass splittings. Our analysis of the COUPP data proceeds similarly to our analysis of the xenon experiments. COUPP had three runs with i) exposures of 70.6 kg·days and an energy threshold of 7.8 keV_{nr}, ii) 88.5 kg·days with an energy threshold of 11 keV_{nr}, and iii) 394 kg·days with an energy threshold of 15.5 keV_{nr}. We considered only single bubble events for which there was a total efficiency of 79.1%, and we used the step-function efficiency model [105] for the iodine nucleation efficiency which rises to 100% above 40 keV_{nr}. Note that we didn't observe a significant shift in the derived limits when using the other parameterized efficiencies [105]. COUPP saw a total of 13 events for all three energy thresholds after time-isolation cuts. Considering these as signal gives a Poisson 90% C.L. limit of 18.96 events. In all cases, we integrated scatters up to 200 keV_{nr} which covers the range of allowed scatters.

The last experiment we consider is KIMS [99] which has a CsI target. Their analysis has 90% C.L. limits on the dark matter scattering rate in eight bins ranging from 3-11 keV_{ee}. For the purposes of constraining operators we consider a scenario ruled out if the predicted rate in any of these eight bins is larger than the stated limit for that bin. Because KIMS uses CsI there is a different quenching factor for

the iodine than the one for NaI crystals. In [106] the quenching factor is measured to be ~ 0.10 over a range of 20 to 120 keV_{nr}. However, similar to NaI, recent results [107] have pointed to a lower value of $Q_I \sim 0.05$ for CsI too. The recent paper only measured CsI doped with sodium, which is not the same as the KIMS detectors which are doped with thallium. However, in light of the new measurement and since the earlier measurement [106] found similar quenching factors for detectors of different doping, a value of $Q_I \sim 0.05$ for the KIMS detectors seems reasonable. Thus, we consider both values in the following analysis and to differentiate it from the iodine quenching factor for NaI, we denote it as Q_{CsI}. As another reminder, we emphasize that we cannot perform this analysis with cesium scattering, so all our constraints from the KIMS experiment are assuming only iodine recoils. Thus, the KIMS limits should get stronger with cesium scattering, but we unfortunately do not know how large of an effect this is.

One other issue we need to consider is the running time of these experiments, since large modulation can lead to order one changes in the scattering rate throughout the year. We use the average scattering rate for XENON100, COUPP, and KIMS since their exposure was accumulated over a year, for LUX we use the maximum rate since its exposure was obtained during the summer, and for XENON10 we average over its run from October to February.

$Q_{\rm NaI}$	m_χ(GeV)	δ(keV)	m_M(GeV)	$\chi^2/d.o.f.$	$r^{90\%}_{\rm XENON10}$	$r^{90\%}_{\rm XENON100}$	$r^{90\%}_{\rm LUX}$	$r^{90\%}_{\rm COUPP}$	$r^{90\%}_{\rm KIMS,0.10}$	$r^{90\%}_{\rm KIMS,0.05}$
Magnetic Inelastic Dark Matter										
0.09	58.0	111.7	3209	0.97	0.0002	17.500	67.5	1.39	1.17	0.08
0.04	122.7	179.3	1096	0.82	0.2943	0.284	0.0	1.32	0.97	0.93

TABLE 5. Best fit parameters and count rates for MIDM.
This table presents the best fit parameters to the DAMA/LIBRA data for the magnetic dipole transition operator and its $\chi^2/d.o.f.$ value. For these operators, the couplings are defined in Eq. 3.19. The final five columns give normalized limits, with the ratio of predicted to 90% C.L. allowed counts for XENON10, XENON100, LUX, and COUPP and the largest ratio of the KIMS bins counts/kg·days/keV over the 90% C.L. limit (this limit is presented for two different iodine quenching factors for KIMS, $Q_{\rm CsI}$). There is a fit for two values of the iodine quenching factor for NaI $Q_{\rm NaI} = 0.09$, 0.04. Due to data taking conditions, the values for the XENON100, COUPP, and KIMS columns use the average yearly rate, the rate for LUX was the maximum, and the rate for XENON10 was averaged from October to February.

Reanalysis of Magnetic Inelastic Dark Matter

In this section, we revisit the case of magnetic inelastic dark matter where the transition is mediated by a magnetic dipole transition [34]

$$\mathcal{L} = \frac{\mu_\chi}{2}\bar{\chi}_2\sigma^{\mu\nu}\chi_1 F_{\mu\nu} + h.c. \tag{3.17}$$

Theoretically this scenario is appealing since the tensor operator vanishes for Majorana fermions, naturally leading to an inelastic transition. Furthermore, iodine has a large dipole moment relative to most other heavy nuclear targets, mitigating xenon and tungsten constraints [34]. As mentioned earlier, the form factors used for these scenarios were highly uncertain [34], but we can now reliably calculate them with our modification of the Mathematica code. Note that cesium does have a large dipole moment as well, but since it isn't implemented in the Mathematica notebook, we unfortunately have to neglect its scattering contribution.

To calculate the form factor for the dipole transition, we use the following coefficients for the fermion operators 9 and 10 involving protons and neutrons

$$\mathcal{L}_{\text{MIDM}} = \frac{1}{q^2}\left[\bar{\chi}_2 i\sigma^{\mu\nu}\frac{q_\nu}{m_M}\chi_1\ \bar{p}\gamma_\mu p\right] \tag{3.18}$$

$$+\ 0.9\frac{m_M}{m_N q^2}\left[\bar{\chi}_2 i\sigma^{\mu\nu}\frac{q_\nu}{m_M}\chi_1\ \bar{p}i\sigma_{\mu\alpha}\frac{q^\alpha}{m_M}p\right]$$

$$-\ 0.96\frac{m_M}{m_N q^2}\left[\bar{\chi}_2 i\sigma^{\mu\nu}\frac{q_\nu}{m_M}\chi_1\ \bar{n}i\sigma_{\mu\alpha}\frac{q^\alpha}{m_M}n\right]. \tag{3.19}$$

The relative coefficients are set by the proton and neutron magnetic moments being 2.8 and -1.91 nuclear magnetons, respectively. Given the overall normalization, the relationship between our m_M and the dark matter dipole moment is $1/m_M = e\mu_\chi$.

The best fit points in this parameter space are shown in Table 5 for the two choices of quenching factor, $Q_{\rm NaI} = 0.09$, 0.04. The $\chi^2/d.o.f.$ for our fit to DAMA is shown, with a $d.o.f. = 9$, showing a very nice goodness of fit. The final six columns show the normalized limits, r, from xenon and iodine experiments so that r values above 1 are constrained at 90% C.L. For XENON10, XENON100, LUX, and COUPP experiments, r is the ratio of predicted events over the number of events allowed at 90% C.L. (2.3, 5.32, 3.89, and 18.96 respectively). For KIMS, in each bin from 3-11 keV_{ee} we take the predicted bin rate divided by the 90% C.L. limit on the rate in that bin, with r being the largest of these bin ratios. We list KIMS constraints where we assume two values of the quenching factor $Q_{\rm CsI} = 0.10$ and 0.05 for CsI. Notice that for $Q_{\rm NaI} = 0.04$, the scenario is narrowly excluded by COUPP while being unconstrained by the other experiments.

Xenon Constraints

The strength of the LUX or XENON100 limit depends strongly on the value of $Q_{\rm NaI}$ we choose. For the standard value $Q_{\rm NaI} = 0.09$, the $2-6$ keV_{ee} energy range of DAMA's modulation spectra is $\sim 22-67$ keV_{nr}. With the lower value of $Q_{\rm NaI} = 0.04$ this changes to a much higher range of $50-150$ keV_{nr}. For inelastic dark matter, the modulated and unmodulated spectra span roughly the same energy bins and since xenon's mass is similar to iodine, the scattering off xenon will be roughly in the same range of nuclear recoil energies. This explains why the LUX constraints are noticeably weaker for $Q_{\rm NaI} = 0.04$, since its acceptance goes to zero above ~ 36 keV_{nr} while XENON100's goes up to 50 keV_{nr}. This acceptance helps to make XENON100 competitive despite its smaller exposure.

To show this effect, we look at the best fit spectra for magnetic inelastic dark matter with different $Q_{\rm NaI}$ values. We saw that XENON100 and LUX were a strong constraint for the larger value of the quenching factor, but the constraints for $Q_{\rm NaI} = 0.04$ were much weaker. This is directly related to the location of the scattering spectrum relative to the experimental acceptance windows as shown in Fig. 13. For $Q_{\rm NaI} = 0.09$, the peak of the spectrum is well covered by both experiments, leading to the stringent constraints. However, for $Q_{\rm NaI} = 0.04$, the peak scattering is missed by both experiments, with LUX having no sensitivity. Given these high energy events, we also checked the constraints from XENON10's inelastic dark matter analysis [24] which extended to much higher energies. In Fig. 13 and Table 5, one can see that this XENON10 constraint is slightly stronger for the smaller iodine quenching factor, but is still not able to constrain this scenario due to its low exposure. On the other hand, in existing XENON100 or LUX data there are about $\sim$ 100 events at high energy, so we encourage an extension of their analysis to energies above 50 $\mathrm{keV_{nr}}$. If the background in this region can be kept under control, they would have a high sensitivity to this scenario.

Iodine Constraints

As expected, the constraints from other iodine detectors are very stringent for most inelastic dark matter scenarios since this is a direct comparison of the same target. For COUPP constraints, changing $Q_{\rm NaI}$ hardly affects the constraints. The energy thresholds of the COUPP runs are not too high to lose many low energy events and the acceptance at high energy means that COUPP is sensitive to essentially all of the iodine scattering relevant for DAMA. This explains why COUPP is the best

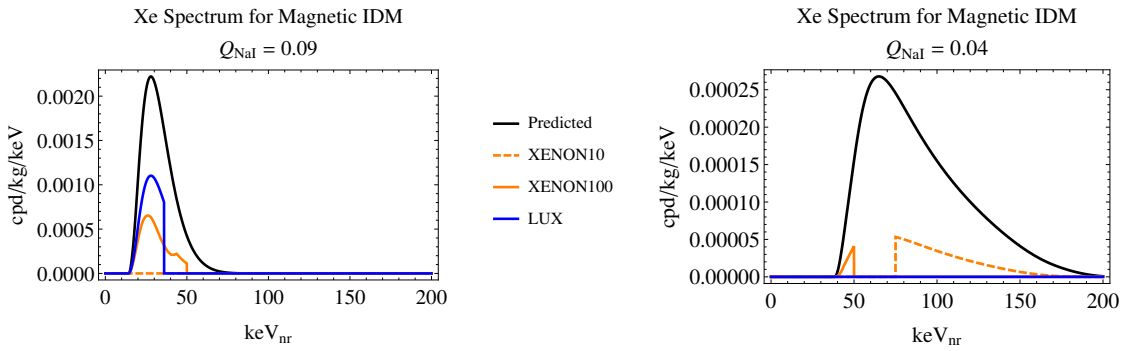

FIGURE 13. Xenon scattering spectrum.
These figures shows the xenon scattering spectrum for the best fit to DAMA's signal for magnetic inelastic dark matter for two choices of $Q_{\rm NaI}$. The black curve is the expected spectrum while the orange (blue, orange-dashed) curve is the accepted spectrum for XENON100 (LUX, XENON10). Note that for $Q_{\rm NaI} = 0.09$ the peak is visible to both XENON100 and LUX, but for $Q_{\rm NaI} = 0.04$ both these experiments' acceptances are too low at high energy to see a significant number of events.

constraint on DAMA both in terms of sensitivity and robustness from quenching factor uncertainties.

For KIMS, if the iodine quenching values used by the DAMA and KIMS experiments, $Q_{\rm NaI} = 0.09, Q_{\rm CsI} = 0.10$ are correct, the best fit point for magnetic inelastic dark matter is ruled out. These constraints show a strong dependence on the quenching factor values chosen. As the recent work of [35] and [107] shows, the correct values are not pinned down yet and could be significantly smaller. This is especially relevant to KIMS constraints, since the scattering spectrum can be substantially shifted in energy, allowing much weaker constraints for some choices of the quenching factors. As an illustration, we show in the four plots of Fig. 14 how the spectra at KIMS shifts as we change the two quenching factors. In the upper left plot, we see that for the quenching factors $Q_{\rm NaI} = 0.09, Q_{\rm CsI} = 0.10$, the best fit point is constrained in the lowest KIMS bin. However, in the upper right plot, changing to $Q_{\rm CsI} = 0.05$, we see that the spectrum shifts to energy bins below their threshold, giving no constraint.

In general, such a combination of quenching factors leads to particular weak limits from KIMS due to the scattering moving below threshold. In the bottom left, the benchmark point with $Q_{\rm NaI} = 0.04, Q_{\rm CsI} = 0.10$, leads to a mild constraint in the 6 keV_{ee} bin. In the bottom right, changing the CsI quenching factor to 0.05, the spectrum shifts to lower values again leading to a rate that is almost constrained in the first bin with a smaller normalized limit, r. Given the uncertainties, we consider both CsI quenching factors in presenting KIMS limits. However, if the same physics leads to the quenching factors of NaI and CsI to be of similar size, we find that KIMS becomes a more robust constraint.

Up to these quenching factor issues, iodine targets still provide the most model independent constraints on scenarios where iodine scattering explains the DAMA signal. For these cases, the only way to suppress scattering is to have higher modulation amplitude. Since COUPP and KIMS both ran over a year, this can lead to a modest drop in sensitivity which explains why the higher δ point has weaker constraints.

Combined Limit Plots for Magnetic Inelastic Dark Matter

Although the best fit points for magnetic inelastic dark matter are ruled out conclusively by COUPP, there can be viable regions of parameter space which maintain a decent fit to DAMA. To search for these we fix the best fit dark matter mass and then explored the remaining two dimensional parameter space in (δ, m_M). For DAMA, the $68, 95\%$ C.L. parameter estimation regions were computed relative to the best fit χ^2. As can be seen in the left plot of Fig. 15, if $Q_{\rm NaI} = 0.09$, the constraints from LUX and XENON100 are strong and rule out all of the DAMA parameter space. However, for the case of $Q_{\rm NaI} = 0.04$, the right plot of Fig. 15

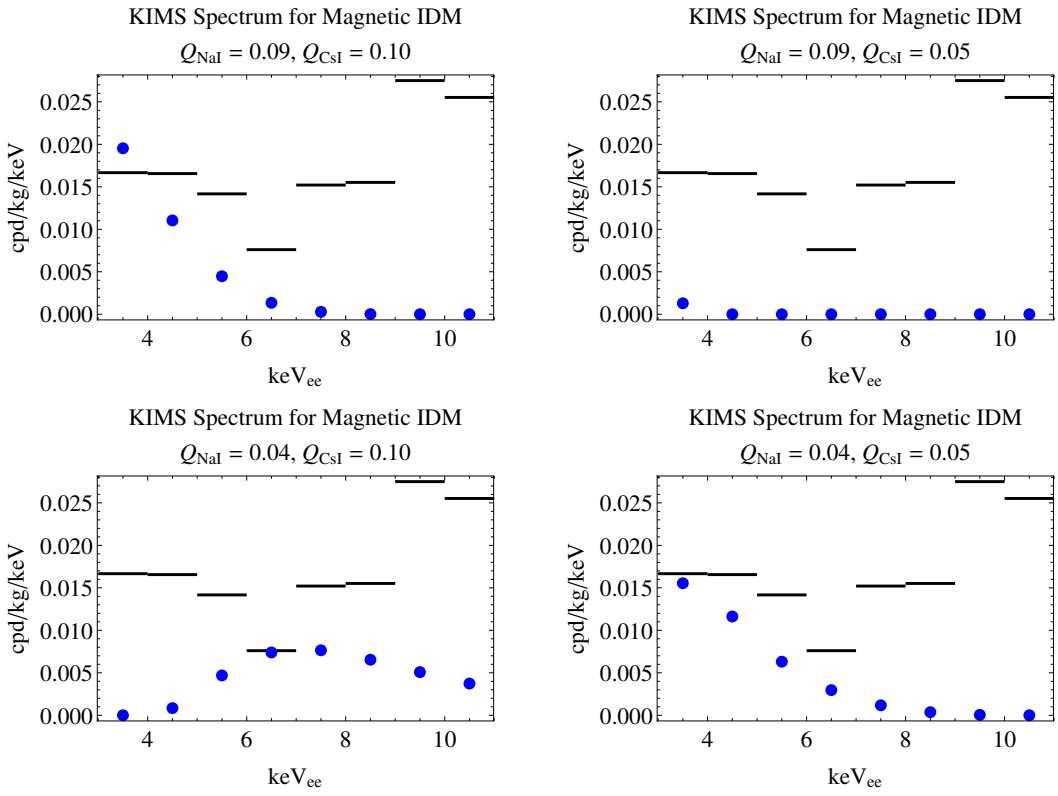

FIGURE 14. KIMS energy spectrum.
This figure shows the KIMS energy spectrum for scattering events for magnetic inelastic dark matter at different $Q_{\rm NaI}$'s and $Q_{\rm CsI}$'s. The blue points are the best fit points predicted rates and the black lines are the 90% limits in each KIMS bin [99]. Notice that the peak can shift from lower to higher energies as the quenching factors vary causing significant changes to the limit.

shows that the constraints from all experiments weaken as one moves to higher values of the mass splitting, leading to a sliver of the 68% C.L. DAMA region which is not constrained and a significant region allowed at 95% C.L. That XENON10 and the iodine experiments slowly fall off with increasing mass splitting shows how these experiments are mostly being weakened by increasing modulation and not a change in the energy spectrum.

In Fig. 16, we show the modulation spectra for the best fit point and an unconstrained point with the DAMA data points for comparison. We see that the

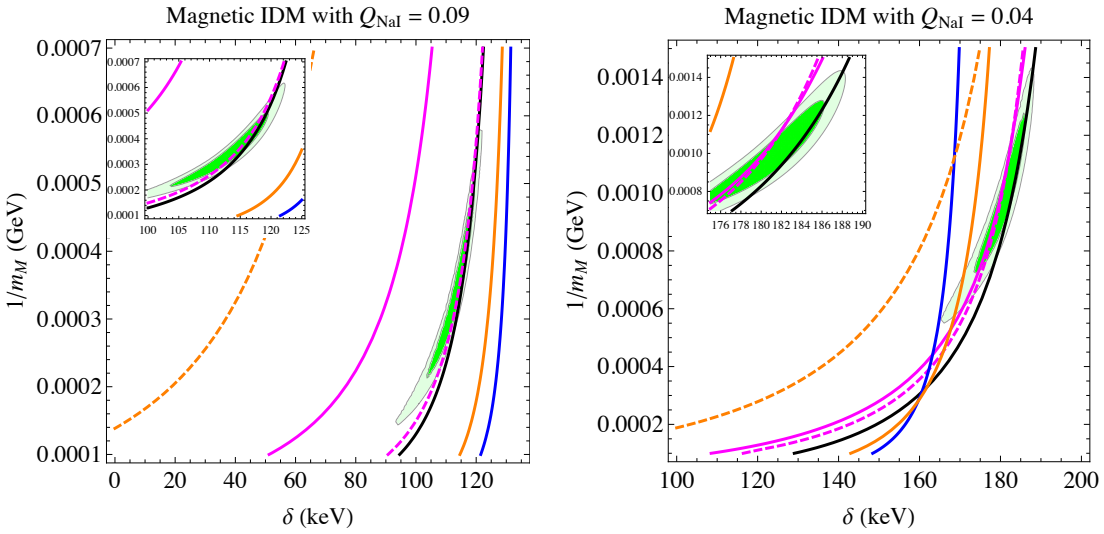

FIGURE 15. Combined limits plots for MIDM.
This figure shows the combined limits plots for magnetic inelastic dark matter. The DM masses used are those listed with the corresponding quenching factor in Table 5. Constraints from LUX (blue), XENON100 (orange), XENON10 (orange dashed), KIMS ($Q_{\rm CsI} = 0.05$ magenta solid, $Q_{\rm CsI} = 0.10$ magenta dashed) and COUPP (black) are also shown, with the 90% C.L. limits listed in section 3.4.

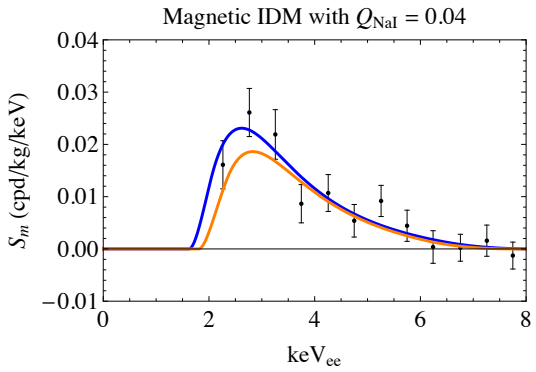

FIGURE 16. MIDM modulation amplitudes.
This shows the magnetic inelastic dark matter modulation amplitudes with the DAMA data points for comparison. The plot assumes a iodine quenching factor $Q_{\rm NaI} = 0.04$ and has both the best-fit modulation amplitude in blue and a sample unconstrained fit in orange. For nine $d.o.f.$, the parameter values for the best fit are $(m_\chi, \delta, m_M) = (122.7\ \text{GeV}, 179.3\ \text{keV}, 1096\ \text{GeV})$ with $\chi^2/d.o.f. = 0.82$ and for the unconstrained point are $(m_\chi, \delta, m_M) = (122.7\ \text{GeV}, 184.5\ \text{keV}, 952\ \text{GeV})$ with $\chi^2/d.o.f. = 1.17$.

increase in mass splitting leads to a degradation in the χ^2 but still has a good fit to the DAMA spectra. Note that the values of $1/m_M$ required are quite reasonable since the magnetic moment of a particle should be of order a dark matter "magneton" $= e/(2m_\chi)$, so that $1/m_M \sim e^2/(2m_\chi) = 5 \times 10^{-4}(\frac{100\ \text{GeV}}{m_\chi})$. The required magnetic moment seems to be similar to those seen in the nucleon sector and thus it seems plausible that this part of parameter space could appear generically in a complete model of magnetic inelastic dark matter.

General Model Independent Analysis

Now, we consider a more general model independent search for consistent scenarios that explain the DAMA annual modulation signal. We performed a survey of the relativistic operators listed in Tables 1-4 by analyzing the scattering when only one operator is turned on at a time. Depending on the operator, we need to multiply by a dimensionful coupling λ to describe the effective operator in the Lagrangian. For the fermion operators, we took this coupling to be $\lambda = 1/m_M^2$, so that m_M characterizes the scale of the effective operator. For the bosonic cases, we instead take $\lambda = 1/m_M$. Thus the parameters we varied were the dark matter mass m_χ, the dimensional coupling parameter m_M, and the mass splitting δ.

Op. #	$Q_{\rm NaI}$	m_χ(GeV)	δ(keV)	m_M(GeV)	$\chi^2/d.o.f.$	$r^{90\%}_{\rm XENON100}$	$r^{90\%}_{\rm LUX}$	$r^{90\%}_{\rm COUPP}$	$r^{90\%}_{\rm KIMS,0.10}$	$r^{90\%}_{\rm KIMS,0.05}$
Spin 1/2 → 1/2 Transition										
2	0.09	44.2	59.0	15.9	1.08	0.049	0.130	3.28	2.27	0.21
	0.04	84.6	103.2	17.4	1.03	0.006	0.014	4.23	2.50	2.16
4	0.09	40.8	57.0	0.5	1.15	0.030	0.082	2.77	2.08	0.06
	0.04	61.8	0.0	1.0	1.01	0.035	0.072	10.30	5.17	4.30
7	0.09	55.3	108.3	1.6	0.97	0.017	0.053	1.41	1.09	0.11
	0.04	111.8	163.2	1.5	0.97	0.001	0.000	1.81	1.22	1.12
8	0.09	44.2	59.0	7.8	1.08	0.049	0.130	3.28	2.27	0.21
	0.04	84.6	103.2	8.3	1.03	0.006	0.014	4.23	2.50	2.16
9	0.09	47.4	69.0	4.6	1.01	40.420	117.900	3.00	2.19	0.21
	0.04	95.1	135.1	4.0	0.99	1.791	2.847	2.79	1.83	1.59
10	0.09	40.9	53.2	2.5	1.06	0.111	0.284	3.12	2.21	0.09
	0.04	62.4	0.0	3.7	1.00	0.156	0.282	12.67	5.26	4.34

TABLE 6. Best fit parameters and counts for fermion-fermion operators I.
This table presents the best fit parameters to the DAMA/LIBRA data for each fermionic operator for which iodine showed an enhancement over xenon, considering proton coupling *only*, and their $\chi^2/d.o.f.$ value. For these fermion operators, the coupling is $\lambda = 1/m_M^2$. The final five columns give normalized limits, with the ratio of predicted to 90% C.L. allowed counts for XENON100, LUX, and COUPP and the largest ratio of the KIMS bins counts/kg·days/keV over the 90% C.L. limit (this limit is presented for two different iodine quenching factors for KIMS, $Q_{\rm CsI}$). Each operator has a fit for two values of the iodine quenching factor for NaI $Q_{\rm NaI} = 0.09, 0.04$. Due to data taking conditions, the values for the XENON100, COUPP, and KIMS columns uses the average yearly rate, and the rate for LUX was the maximum.

Op. #	$Q_{\rm NaI}$	m_χ(GeV)	δ(keV)	m_M(GeV)	$\chi^2/d.o.f.$	$r^{90\%}_{\rm XENON100}$	$r^{90\%}_{\rm LUX}$	$r^{90\%}_{\rm COUPP}$	$r^{90\%}_{\rm KIMS,0.10}$	$r^{90\%}_{\rm KIMS,0.05}$
Spin $1/2 \to 1/2$ Transition										
11	0.09	50.8	96.6	5.8	1.11	0.042	0.119	1.72	1.29	0.10
	0.04	85.5	106.4	7.7	1.03	0.032	0.056	4.26	2.44	2.10
13	0.09	56.1	110.9	19.6	0.96	13.640	55.640	1.32	1.08	0.08
	0.04	112.6	170.7	15.6	0.94	0.751	0.015	1.42	0.97	0.92
14	0.09	50.8	96.6	5.8	1.11	0.042	0.119	1.72	1.29	0.10
	0.04	85.5	106.4	7.7	1.03	0.032	0.056	4.26	2.44	2.10
15	0.09	54.3	106.0	49.6	1.02	0.021	0.069	1.49	1.15	0.10
	0.04	102.7	146.8	54.3	1.00	0.005	0.006	2.47	1.60	1.44
19	0.09	52.6	97.5	0.6	1.02	0.045	0.139	1.66	1.23	0.09
	0.04	99.9	137.7	0.7	1.01	0.012	0.015	2.18	1.36	1.20
20	0.09	40.8	57.0	2.5	1.15	0.030	0.082	2.77	2.08	0.06
	0.04	61.8	0.0	3.9	1.01	0.035	0.072	10.30	5.17	4.30

TABLE 7. Best fit parameters and counts for fermion-fermion operators II.
This table presents the best fit parameters to the DAMA/LIBRA data for each fermionic operator for which iodine showed an enhancement over xenon, considering proton coupling *only*, and their $\chi^2/d.o.f.$ value. For these fermion operators, the coupling is $\lambda = 1/m_M^2$. The final five columns give normalized limits, with the ratio of predicted to 90% C.L. allowed counts for XENON100, LUX, and COUPP and the largest ratio of the KIMS bins counts/kg·days/keV over the 90% C.L. limit (this limit is presented for two different iodine quenching factors for KIMS, $Q_{\rm CsI}$). Each operator has a fit for two values of the iodine quenching factor for NaI $Q_{\rm NaI} = 0.09, 0.04$. Due to data taking conditions, the values for the XENON100, COUPP, and KIMS columns uses the average yearly rate, and the rate for LUX was the maximum.

To narrow our survey and to specifically avoid the stringent constraints of xenon target experiments, we only considered operators whose transition probabilities for iodine were significantly ($\geq$ 10 times) enhanced over xenon. These operators were identified by examining the ratio of iodine's transition probability to xenon's at the minimum velocity for iodine (see Eq. 3.7), as it is higher than the minimum velocity for xenon scattering. This ratio was plotted, for a specific value of m_χ on the (δ, E_R) plane with E_R the nuclear recoil energy (the parameter m_M cancels in the ratio). The operators' coupling to nucleons was varied between pure proton, pure neutron, equal coupling to proton and neutron, and equal but opposite couplings. We found that only pure coupling to protons significantly favored iodine over xenon and further that all iodine-enhanced operators had some contribution from the nucleon spin $\vec{\mathcal{O}}_3^N$, see Eq. 3.12. Since iodine's nucleus has an unpaired proton while xenon has an unpaired neutron, this explains why the sensitivity is enhanced if we only couple to the proton [108]. As a check that this method for selecting operators finds all relevant ones, we also performed a full analysis for several other operators and nucleon couplings and found the results matched our predictions from this selection process. Note that our inability to treat cesium in KIMS is particularly important for coupling to proton spin, since cesium also has an unpaired proton. On the other hand, tungsten isotopes only have unpaired neutrons, so we expect that their rates would be suppressed much like xenon targets.

The best fit points in this parameter space is shown in Tables 6 - 9 for the two choices of quenching factor of $Q_{\rm NaI} = 0.09$, 0.04. The $\chi^2/d.o.f.$ for our fit to DAMA is shown, with a $d.o.f. = 9$, showing a reasonable goodness of fit for all operators. The final five columns show the normalized limits, r, from xenon and iodine experiments so that r values above 1 are constrained at 90% C.L. For XENON100, LUX, and

COUPP experiments, r is the ratio of predicted events over the number of events allowed at 90% C.L. (5.32, 3.89, and 18.96 respectively). For KIMS, in each bin from 3-11 keV_{ee} we take the predicted bin rate divided by the 90% C.L. limit on the rate in that bin, with r being the largest of these bin ratios. We list KIMS constraints where we assume two values of the quenching factor $Q_{\text{CsI}} = 0.10$ and 0.05 for CsI. Notice that there are a few operators which are narrowly excluded by COUPP while being unconstrained by the other experiments.

Even though we've discussed how XENON10 is sensitive to much higher energy scatters than XENON100 or LUX, we find that it generically sets weaker constraints for this model independent analysis due to its lower exposure. In a few cases, the limits of XENON10 were similar or just a bit larger than XENON100, for example fermion operators 7, 15, and 19, spin 0 to 1 operators 6, and spin 0 to 0 operator 4, but they were not large enough to be constraining. Because these constraints were not strong enough to rule out any best fit points, we chose not to include the XENON10 limits in our tables or figures for this model independent survey.

Op. #	$Q_{\rm NaI}$	m_χ(GeV)	δ(keV)	m_M(GeV)	$\chi^2/d.o.f.$	$r^{90\%}_{\rm XENON100}$	$r^{90\%}_{\rm LUX}$	$r^{90\%}_{\rm COUPP}$	$r^{90\%}_{\rm KIMS,0.10}$	$r^{90\%}_{\rm KIMS,0.05}$
Spin $0 \to 1$ Transition										
4	0.09	40.8	57.0	0.5	1.15	0.030	0.082	2.77	2.08	0.06
	0.04	61.8	0.0	1.0	1.01	0.035	0.072	10.30	5.17	4.30
5	0.09	40.8	57.0	0.5	1.15	0.030	0.082	2.77	2.08	0.06
	0.04	61.8	0.0	1.0	1.01	0.035	0.072	10.30	5.17	4.30
6	0.09	54.3	106.0	22.6	1.02	0.021	0.069	1.49	1.15	0.10
	0.04	102.7	146.8	14.3	1.00	0.005	0.006	2.47	1.60	1.44
7	0.09	50.8	96.6	1.4	1.11	0.042	0.119	1.72	1.29	0.10
	0.04	85.5	106.4	1.6	1.03	0.032	0.056	4.26	2.44	2.10

TABLE 8. Best fit parameters and counts for scalar-vector operators.
This table presents the best fit parameters to the DAMA/LIBRA data for each bosonic operator for which iodine showed an enhancement over xenon, considering proton coupling *only*, and their $\chi^2/d.o.f.$ value. For these bosonic operators, the coupling is $\lambda = 1/m_M$. The final five columns give normalized limits, with the ratio of predicted to 90% C.L. allowed counts for XENON100, LUX, and COUPP and the largest ratio of the KIMS bins counts/kg·days/keV over the 90% C.L. limit (this limit is presented for two different iodine quenching factors for KIMS, $Q_{\rm CsI}$). Each operator has a fit for two values of the iodine quenching factor for NaI $Q_{\rm NaI} = 0.09, 0.04$. Due to data taking conditions, the values for the XENON100, COUPP, and KIMS columns uses the average yearly rate, and the rate for LUX was the maximum.

Op. #	$Q_{\rm NaI}$	m_χ(GeV)	δ(keV)	m_M(GeV)	$\chi^2/d.o.f.$	$r^{90\%}_{\rm XENON100}$	$r^{90\%}_{\rm LUX}$	$r^{90\%}_{\rm COUPP}$	$r^{90\%}_{\rm KIMS,0.10}$	$r^{90\%}_{\rm KIMS,0.05}$
Spin $0 \to 0$ Transition										
2	0.09	44.2	58.2	1.0	1.08	0.049	0.127	3.32	2.29	0.21
	0.04	84.6	103.3	1.1	1.03	0.005	0.013	4.21	2.49	2.15
4	0.09	56.6	108.7	1.0	0.99	0.011	0.041	1.48	1.16	0.10
	0.04	115.6	166.7	1.3	0.96	0.001	0.000	1.76	1.21	1.12
5	0.09	44.2	58.2	1.0	1.08	0.049	0.127	3.32	2.29	0.21
	0.04	84.6	103.3	1.1	1.03	0.005	0.013	4.21	2.49	2.15
7	0.09	44.2	58.2	3.7	1.08	0.049	0.127	3.32	2.29	0.21
	0.04	84.6	103.3	4.5	1.03	0.005	0.013	4.21	2.49	2.15

TABLE 9. Best fit parameters and counts for scalar-scalar operators.
This table presents the best fit parameters to the DAMA/LIBRA data for each bosonic operator for which iodine showed an enhancement over xenon, considering proton coupling *only*, and their $\chi^2/d.o.f.$ value. For these bosonic operators, the coupling is $\lambda = 1/m_M$. The final five columns give normalized limits, with the ratio of predicted to 90% C.L. allowed counts for XENON100, LUX, and COUPP and the largest ratio of the KIMS bins counts/kg·days/keV over the 90% C.L. limit (this limit is presented for two different iodine quenching factors for KIMS, $Q_{\rm CsI}$). Each operator has a fit for two values of the iodine quenching factor for NaI $Q_{\rm NaI} = 0.09, 0.04$. Due to data taking conditions, the values for the XENON100, COUPP, and KIMS columns uses the average yearly rate, and the rate for LUX was the maximum.

Combined Limit Plots for Relativistic Operators

Although the best fit points are ruled out conclusively by COUPP, we still find viable regions of parameter space which maintain a decent fit to DAMA, similar to the case of magnetic inelastic dark matter. For some of the operators, we found that the DAMA regions could stretch far into the high δ region of parameter space. The resulting increase in modulation can lead to consistency with the COUPP and KIMS constraints. The fermion operators which have such an allowed region are operator 2 for $Q_{\rm NaI} = 0.09$, operator 7 for both quenching factors, operator 9 for $Q_{\rm NaI} = 0.04$, 11 for $Q_{\rm NaI} = 0.09$, 13 for $Q_{\rm NaI} = 0.04$, 15 with both quenching factors, and 19 with both quenching factors. Also the scalar to scalar operator 4 has a consistent region for both quenching factors. For these operators, we have plotted the allowed regions in Fig. 17 and 18. One again can see that the key to avoiding constraints is moving to higher δ. Thus, the allowed spectra at DAMA will again generically be at slightly higher energy with a slight reduction in the overall amplitude, similar to what was seen in Fig. 16. In this list of allowed operators, we ignored degeneracies in scattering form factors where we have the families i) fermion 2, fermion 8, scalar 2, and scalar 5, ii) fermion 11, fermion 14, and scalar to vector 7, iii) fermion 15 and scalar to vector 6. These families share allowed parameter space, although different values for m_M are required to get the same rate. Interestingly, some operators whose best fit values are only narrowly ruled out remain ruled out in these two dimensional scans. For instance, fermion operators 4, 10, 20 and scalar to scalar operator 7 have reasonable constraints for $Q_{\rm NaI} = 0.09$. In these cases, the form factors do not allow good DAMA fits to persist to higher δ thus making it impossible to avoid the constraints.

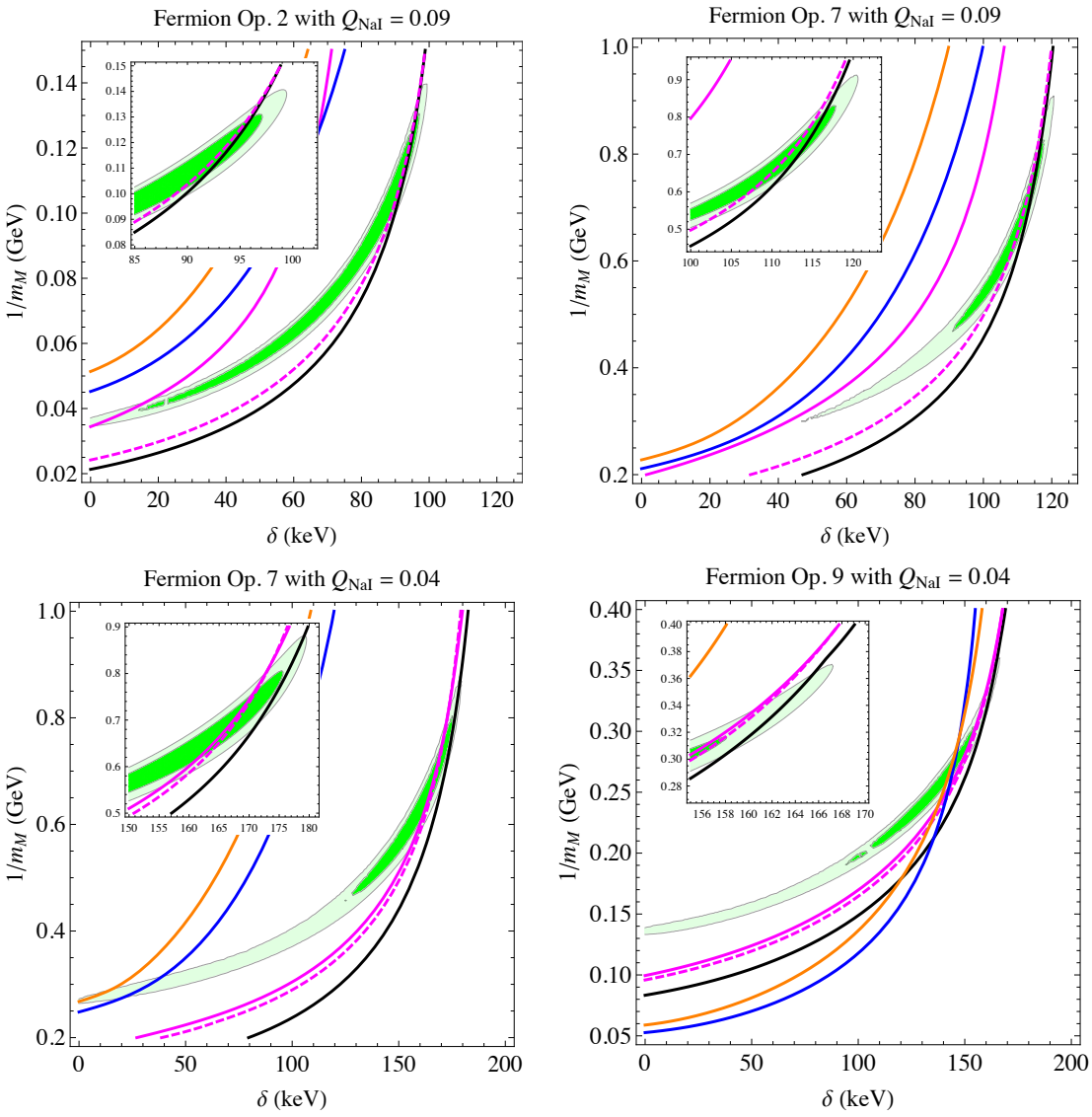

FIGURE 17. Combined limits plots I.
This figure shows the combined limits plots for operators which have an unconstrained region that fits the DAMA signal. The DM masses used are those listed with the corresponding operator in Tables 6 and 7. Constraints from LUX (blue), XENON100 (orange), KIMS ($Q_{\rm CsI}$ = 0.05 magenta solid, $Q_{\rm CsI}$ = 0.10 magenta dashed) and COUPP (black) are also shown, with the 90% C.L. limits listed in section 3.4.

Conclusions

We have shown that a nonrelativistic effective theory for the inelastic scattering of dark matter off a nucleus is a straightforward extension of elastic scattering. The

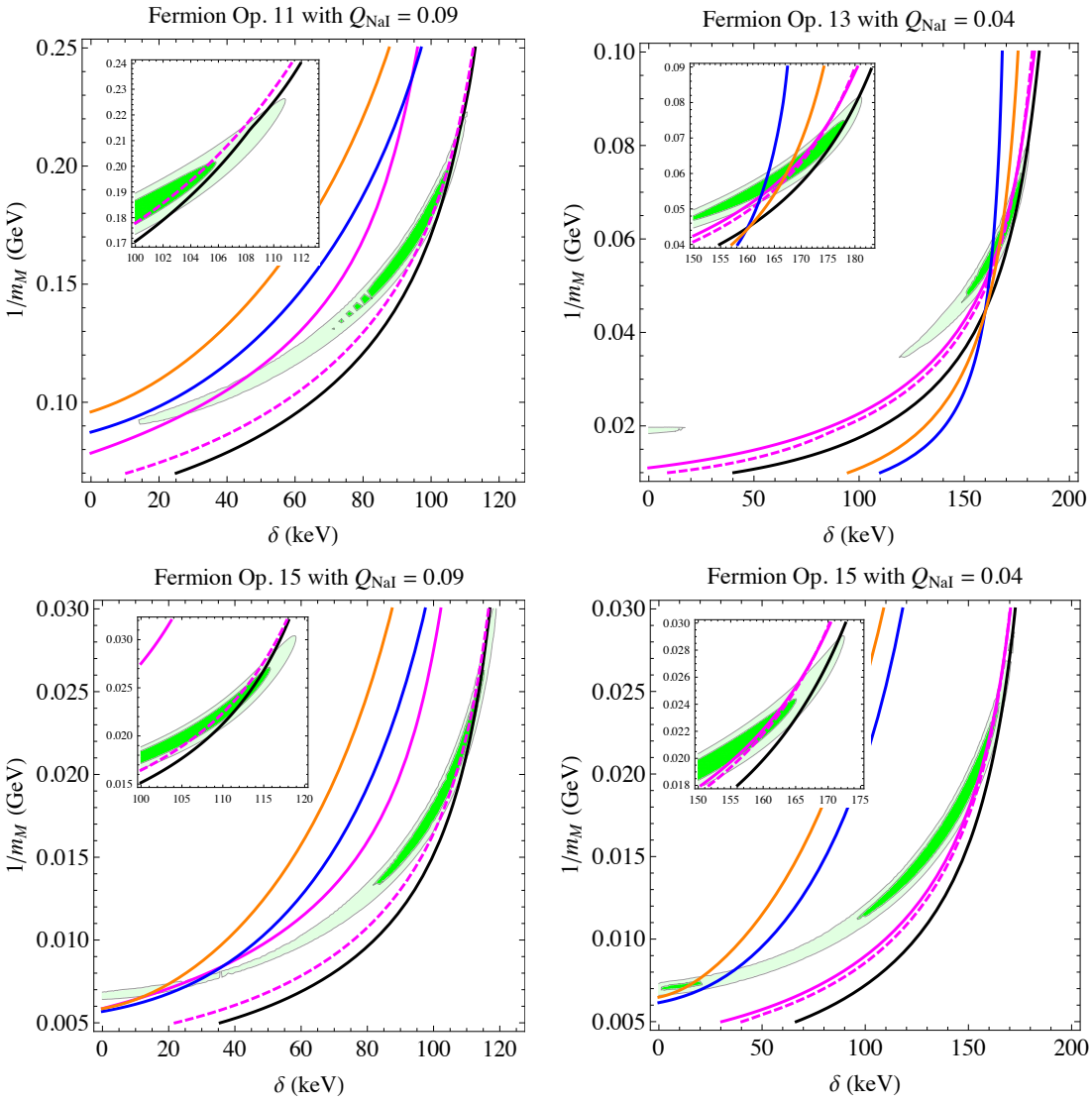

FIGURE 18. Combined limits plots II.
This figure shows the combined limits plots for operators which have an unconstrained region that fits the DAMA signal. The DM masses used are those listed with the corresponding operator in Tables 6 and 7. Constraints from LUX (blue), XENON100 (orange), KIMS ($Q_{\rm CsI}$ = 0.05 magenta solid, $Q_{\rm CsI}$ = 0.10 magenta dashed) and COUPP (black) are also shown, with the 90% C.L. limits listed in section 3.4.

modifications revolve around the Galilean-invariant, incoming dark matter velocity. Due to the inelastic kinematics, the components of the incident velocity that are perpendicular to the momentum transfer $\vec{q}$ have a new piece that depends on the

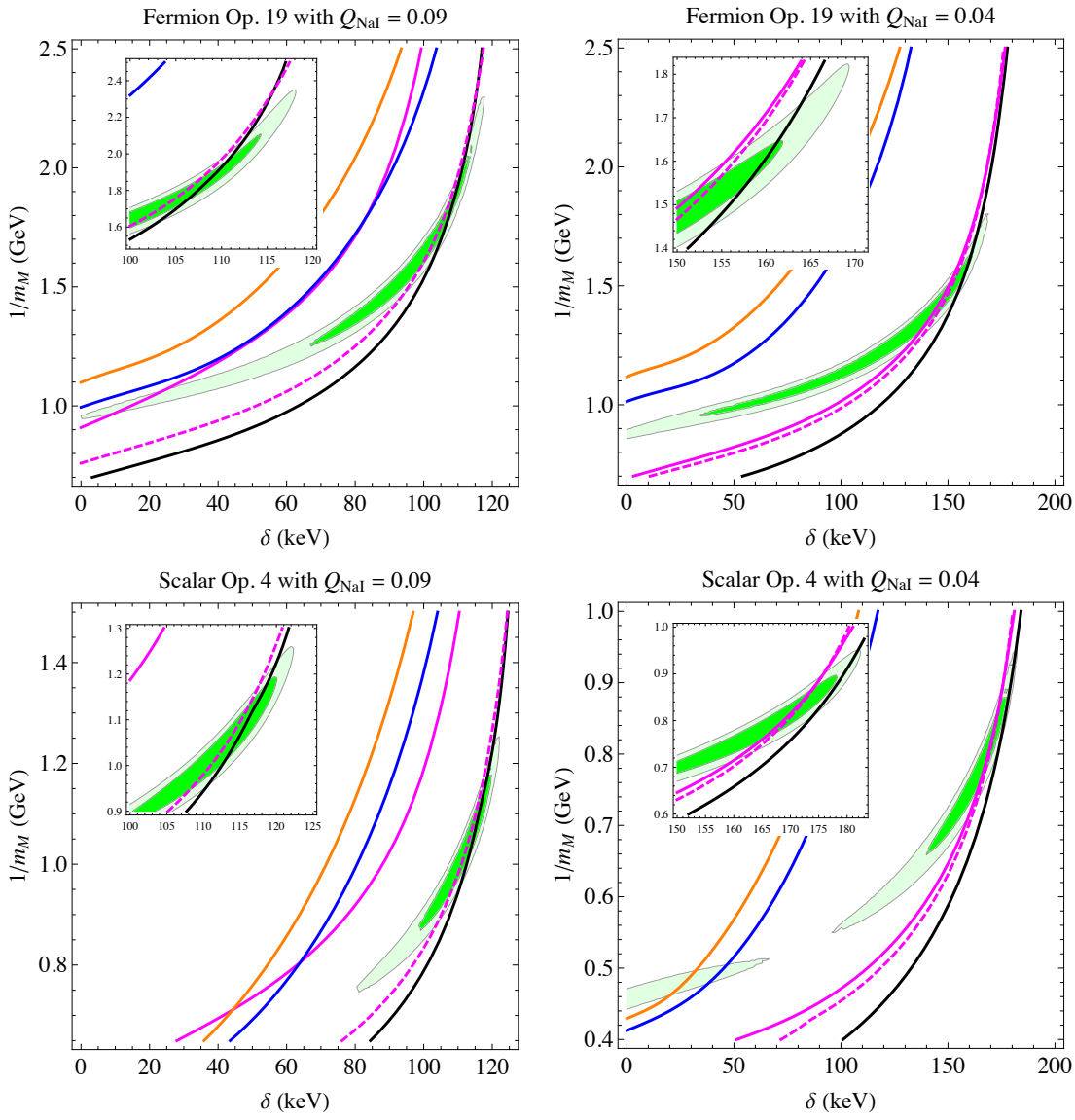

FIGURE 19. Combined limits plots III.
This figure shows the combined limits plots for the remaining operators which have an unconstrained region that fits the DAMA signal. The DM masses used are those listed with the corresponding operator in Tables 6 - 9. Constraints from LUX (blue), XENON100 (orange), KIMS ($Q_{\rm CsI} = 0.05$ magenta solid, $Q_{\rm CsI} = 0.10$ magenta dashed) and COUPP (black) are also shown, with the 90% C.L. limits listed in section 3.4.

mass splitting δ

$$\vec{v}^{\perp}_{\rm inel} \equiv \vec{v} + \frac{\vec{q}}{2\mu_N} + \frac{\delta}{|\vec{q}|^2}\vec{q}. \tag{3.20}$$

This variable change motivates a new basis of scattering matrix elements written in terms of $\vec{v}_{\rm inel}^{\perp}$. As an application, we have shown how inelastic transitions of a fermion to fermion, scalar to scalar, and scalar to vector can be written in terms of this basis. Finally, since the nuclear matrix elements for most cases only depend linearly on this velocity, we were able to modify the Mathematica code [33] to generate the form factors for inelastic scattering processes. Thus, our work extends the framework of [32] so that inelastic dark matter transitions can now be treated in a model independent fashion.

Armed with our effective theory, we then created several fits to the DAMA/LIBRA annual modulation. We considered both the scenario of magnetic inelastic dark matter as well as a model independent survey looking at individual relativistic operators. Due to the strong constraints from XENON100 and LUX, in the model independent scan, we considered choices for the nucleon couplings that would enhance iodine scattering over xenon. This led us to consider operators involving only couplings to protons that are sensitive to the proton spin. CDMS constraints by comparison are significantly weaker due to germanium's lighter mass and even smaller proton spin. However, we showed that there are significant constraints from the iodine experiments KIMS and COUPP, which provide a mostly model-independent constraint. These limits are thus harder to avoid; we find that they can only be weakened by enhanced modulation or by uncertainties in the iodine quenching factors, which affect the KIMS limits.

For the case of magnetic inelastic dark matter and for some of the relativistic operators involving only proton couplings, we found that scenarios could be consistent with the DAMA fit and existing constraints. However, we would like to stress that we are not able to definitively claim a consistent explanation of the DAMA signal.

First of all, due to lack of implementation, we could not treat scattering off of cesium or tungsten, which are relevant for KIMS and CRESST. Cs in particular has an unpaired proton and should lead to stronger constraints from KIMS. Hopefully in a future update of the notebook [33], these elements could be included. Second, we only tested the relativistic *operators* using our effective theory. No models explaining these interactions were considered and thus in a complete model may run into difficulties when confronted with other dark matter constraints. However, it would be interesting to look at complete models realizing these scenarios, which we leave to future work. In particular, the magnetic inelastic dark matter scenario should be straightforward to build in a model, since the required coupling structure is through the standard electromagnetic couplings (for specific realizations see refs. [109, 110]).

In the near future, these models should be definitively tested from direct detection experiments alone. To do so, one high priority is resolving the current uncertainty in iodine quenching factors so as to both pin down the DAMA parameter space and firm up the constraints from KIMS. Existing data at XENON100 and LUX at energies above 50 $\mathrm{keV_{nr}}$ should also be reanalyzed which will enhance sensitivities to scenarios when the iodine quenching factor is low. Finally, iodine target experiments are the most robust tool to rule out or discover these scenarios. In particular, COUPP's next analysis should give us a definitive answer whether iodine scattering scenarios are a consistent explanation of DAMA's annual modulation signal.

Relativistic Derivation of Nonrelativistic Velocity Operators

As mentioned earlier, there are two ways of constructing the velocity degrees of freedom used in our nonrelativistic theory: starting with Galilean invariant operators and orthogonalizing them or starting with the relativistic kinematics and reducing to

the nonrelativistic limit. Here we derive the results shown in section 3.2 using the second method.

To begin, we have the four four-momenta of Fig. 11 from which we need to construct Galilean invariant velocities. As there are ten constraints; one from energy conservation, three from momentum conservation, four from mass constraints, and two from rotational invariance; we only need two velocity operators. Using a little foresight, we define three velocities

$$\begin{aligned}
\vec{v}_N &\equiv \vec{v}_{N_{in}} - \vec{v}_{N_{out}}, \\
\vec{v}_\chi &\equiv \frac{m_{\chi_1} + m_{\chi_2}}{2m_N}(\vec{v}_{\chi_2} - \vec{v}_{\chi_1}), \text{ and} \\
\vec{v}_{\rm el}^{\perp} &\equiv \frac{1}{2}(\vec{v}_{\chi_2} + \vec{v}_{\chi_1} - \vec{v}_{N_{out}} - \vec{v}_{N_{in}}).
\end{aligned} \tag{3.21}$$

and expect to find one relationship between them beyond the orthogonality relations so as to have a total of six degrees of freedom. The mass factor in front of the relative DM velocity is so that in the elastic limit $\vec{v}_\chi \to \vec{v}_N$. We also chose the form for $\vec{v}_{\rm el}^{\perp}$ which is perpendicular to the momentum transfer in the elastic limit and because the velocities have good quantum numbers under P, T, and hermitian conjugation.

Now that we have our three velocities, we need to orthogonalize them. We begin with Lorentz invariant combinations:

$$\begin{aligned}
(p+k)^2 &= (p'+k')^2, \\
(p-k')^2 &= (p'-k)^2, \\
k'^2 &= (p+k-p')^2, \text{ and} \\
(p-p')^2 &= (k-k')^2,
\end{aligned} \tag{3.22}$$

which we take the nonrelativistic limit of to obtain

$$
\begin{aligned}
&-(m_{\chi_1}+m_N)^2 - m_{\chi_1}m_N(\vec{v}_{\chi_1}-\vec{v}_{N_{in}})^2 = -(m_{\chi_2}+m_N)^2 - m_{\chi_2}m_N(\vec{v}_{\chi_2}-\vec{v}_{N_{out}})^2,\\
&-(m_{\chi_1}-m_N)^2 + m_{\chi_1}m_N(\vec{v}_{\chi_1}-\vec{v}_{N_{out}})^2 = -(m_{\chi_2}-m_N)^2 + m_{\chi_2}m_N(\vec{v}_{\chi_2}-\vec{v}_{N_{in}})^2,\\
&-(m_{\chi_1}+m_N-m_{\chi_2})^2 - m_{\chi_1}m_N(\vec{v}_{\chi_1}-\vec{v}_{N_{in}})^2 + m_{\chi_1}m_{\chi_2}(\vec{v}_{\chi_1}-\vec{v}_{\chi_2})^2\\
&+m_{\chi_2}m_N(\vec{v}_{\chi_2}-\vec{v}_{N_{in}})^2 = -m_N^2, \text{ and}\\
&-(m_{\chi_1}-m_{\chi_2})^2 + m_{\chi_1}m_{\chi_2}(\vec{v}_{\chi_1}-\vec{v}_{\chi_2})^2 = m_N^2(\vec{v}_{N_{in}}-\vec{v}_{N_{out}})^2.
\end{aligned}
\tag{3.23}
$$

From these relations we can substitute in the velocities from Eq. 3.21 and solve for their dot products. These are, with the replacement $m_{\chi_2} \to m_{\chi_1}+\delta$,

$$
\begin{aligned}
\vec{v}_N\cdot\vec{v}_\chi &= v_\chi^2,\\
\vec{v}_N\cdot\vec{v}_{\rm el}^{\perp} &= -\frac{\delta\left((\delta+2m_{\chi_1})^2+m_N^2v_\chi^2\right)}{m_N(\delta+2m_{\chi_1})^2}, \text{ and}\\
\vec{v}_\chi\cdot\vec{v}_{\rm el}^{\perp} &= -\frac{\delta\left((\delta+2m_{\chi_1})^2\left(v_N^2+4(v_{\rm el}^{\perp})^2+8\right)+4m_N^2v_\chi^2\right)}{8m_N(\delta+2m_{\chi_1})^2}.
\end{aligned}
\tag{3.24}
$$

Also, because of the degrees of freedom and our choice of velocities there is a relation between v_N^2 and v_χ^2. This is obtained from the last momentum-conservation equation of Eq. 3.22 and is

$$
\frac{4m_{\chi_1}(m_{\chi_1}+\delta)m_N^2}{(2m_{\chi_1}+\delta)^2}v_\chi^2 = \delta^2 + m_N^2v_N^2. \tag{3.25}
$$

The final, orthogonal velocities are given by

$$\begin{aligned}
\vec{v}_N^{\perp} &= \vec{v}_N, \\
\vec{v}_\chi^{\perp} &= \vec{v}_\chi - \frac{\vec{v}_\chi \cdot \vec{v}_N^{\perp}}{(\vec{v}_N^{\perp})^2}\vec{v}_N^{\perp}, \text{ and} \\
\vec{v}_{\text{inel}}^{\perp} &= \vec{v}_{\text{el}}^{\perp} - \frac{\vec{v}_{\text{el}}^{\perp} \cdot \vec{v}_N^{\perp}}{|\vec{v}_N^{\perp}|^2}\vec{v}_N^{\perp} - \frac{\vec{v}_{\text{el}}^{\perp} \cdot \vec{v}_\chi^{\perp}}{|\vec{v}_\chi^{\perp}|^2}\vec{v}_\chi^{\perp}.
\end{aligned} \tag{3.26}$$

As stated in section 3.2, we are treating all momenta as order v and δ as order v^2, so the final forms for the velocity operators are, with $\vec{v}_N \to \vec{q}/m_N$,

$$\vec{v}_N^{\perp} = \frac{\vec{q}}{m_N}, \vec{v}_\chi^{\perp} = 0, \text{ and } \vec{v}_{\text{inel}}^{\perp} = \vec{v}_{\text{el}}^{\perp} + \frac{\delta}{|\vec{q}|^2}\vec{q}, \tag{3.27}$$

so we only have two velocity-like operators. As a check, these variables agree with section 3.2.

Reduction of Relativistic Operators

In this paper we have written the nonrelativistic reduction of many relativistic operators, but there are other possibilities not considered here (mainly interactions with spin 2 and beyond mediators). To help with the reduction of these other operators, we have included a series of reductions for the prototypical elements of a relativistic field theory. See [111] for similar results.

We concern ourselves with the spinor contractions

$$\begin{gathered}
\bar{\psi}_2\psi_1, \quad \bar{\psi}_2\gamma^5\psi_1, \quad \bar{\psi}_2\gamma_\mu\gamma^5\psi_1, \\
\bar{\psi}_2\sigma_{\mu\nu}\psi_1, \text{ and } \quad \bar{\psi}_2\sigma_{\mu\nu}\gamma^5\psi_1,
\end{gathered}$$

where $\sigma_{\mu\nu} \equiv \frac{i}{2}[\gamma_\mu, \gamma_\nu]$.

In the nonrelativistic limit these become

$$\bar{\psi}_2\psi_1 \simeq 2\sqrt{m_1}\sqrt{m_2}\mathbf{1}_\psi, \tag{3.28}$$

$$\bar{\psi}_2\gamma^5\psi_1 \simeq 2\sqrt{m_1}\sqrt{m_2}(\vec{v}_1 - \vec{v}_2)\cdot\vec{S}_\psi, \tag{3.29}$$

$$\bar{\psi}_2\gamma_\mu\gamma^5\psi_1 \simeq 2\sqrt{m_1}\sqrt{m_2}(2S^i_\psi\delta^i_\mu - (\vec{v}_1 + \vec{v}_2)\cdot\vec{S}_\psi\delta^0_\mu), \tag{3.30}$$

$$\begin{aligned}\bar{\psi}_2\sigma_{\mu\nu}\psi_1 \simeq \sqrt{m_1}\sqrt{m_2}\Big\{ & 4\epsilon_{ijk}S^k_\psi\delta^i_\mu\delta^j_\nu \\ & + i(\delta^0_\mu\delta^a_\nu - \delta^a_\mu\delta^0_\nu)\left[-2i\epsilon_{aik}(\vec{v}_1 + \vec{v}_2)^i S^k_\psi + (\vec{v}_1 - \vec{v}_2)^a\right]\Big\}, \text{ and}\end{aligned} \tag{3.31}$$

$$\begin{aligned}\bar{\psi}_2\sigma_{\mu\nu}\gamma^5\psi_1 \simeq -\sqrt{m_1}\sqrt{m_2}\Big\{ & 4iS^i_\psi(\delta^0_\mu\delta^i_\nu - \delta^i_\mu\delta^0_\nu) \\ & + \epsilon_{abc}\delta^a_\mu\delta^b_\nu\left[-2i\epsilon_{cid}(\vec{v}_1 + \vec{v}_2)^i S^d_\psi + (\vec{v}_1 - \vec{v}_2)^c\right]\Big\}.\end{aligned} \tag{3.32}$$

In these equations $\mathbf{1}_\psi$ is the unit operator in spin-space, $\vec{v}_1$ is the velocity of the incoming ψ_1 particle, $\vec{v}_2$ is the velocity of the outgoing ψ_2 particle, $\vec{S}_\psi$ is the spin operator for the ψ particle, $g_{\mu\nu}$ is the metric tensor, and ϵ_{ijk} is the Levi-Civita symbol. These reductions rely on ψ_1 in the initial state and ψ_2 in the final state (not their antiparticles) and that the only difference in these particles is the mass (m_1 and m_2 for initial and final respectively). One can also use the Gordon identity,

$$\bar{\psi}_1\gamma_\mu\psi_2 = \frac{1}{2\sqrt{m_1}\sqrt{m_2}}\bar{\psi}_1(p_{1\mu} + p_{2\mu} + i\sigma_{\mu\nu}q^\nu)\psi_2, \tag{3.33}$$

for the vector interaction.

Another useful result is the nonrelativistic limit for the time-like component of the momentum transfer, which is

$$
\begin{aligned}
q^0 &\simeq \delta + \frac{m_{\chi 1}}{2}(\vec{v}_{\chi 2}^2 - \vec{v}_{\chi 1}^2), \text{ or} \\
q^0 &\simeq \frac{m_N}{2}(\vec{v}_{N_{in}}^2 - \vec{v}_{N_{out}}^2).
\end{aligned}
\tag{3.34}
$$

These relations are sometimes needed for the preservation of Galilean invariance but can be easy to overlook.

To reduce operators for spin 1 particles we must take into account the polarization of a nonrelativistic vector boson. This is given by

$$
\begin{aligned}
\varepsilon_\lambda^0(\vec{p}) &\simeq \frac{\vec{p}}{m} \cdot \vec{\varepsilon}_\lambda(\vec{0}) \\
\vec{\varepsilon}_\lambda(\vec{p}) &\simeq \vec{\varepsilon}_\lambda(\vec{0}),
\end{aligned}
\tag{3.35}
$$

to lowest order in $\vec{p}$.

Transition Amplitude in Nuclear Response Basis

Since the effective theory for inelastic dark matter is so similar to the effective theory for elastic dark matter, it can be easy to overlook some of the important differences. The change in the Galilean-invariant incoming dark matter velocity is stressed above, but the possible complex nature for the coefficients of the nonrelativistic operators Eq. 3.8 is another modification. To highlight both of these effects we reproduce the relevant results for the squared matrix element, following [33].

First we write our Lagrangian as

$$
\mathcal{L} = \sum_{\tau=0,1} \sum_{i=1}^{15} c_i^\tau \mathcal{O}_i, \tag{3.36}
$$

where τ characterizes the isospin structure of the coupling, allowing different couplings to protons and neutrons. We then calculate the transition amplitude, by averaging over initial spins and summing over outgoing spins, and expand in the basis of the nuclear responses, giving

$$\begin{aligned}
\frac{1}{2j_\chi+1}\frac{1}{2j_N+1}\sum_{\text{spins}}|\mathcal{M}|^2_{\text{nuclear}} = \frac{4\pi}{2j_N+1}\sum_{\tau=0,1}\sum_{\tau'=0,1}\Bigg\{ \\
\sum_{J=0,2,\ldots}^{\infty}\Bigg[R_M^{\tau\tau'}(|\vec{v}^{\perp}_{\text{inel}\,T}|^2,\frac{|\vec{q}|^2}{m_N^2})\langle j_N||M_{J;\tau}(q)||j_N\rangle\langle j_N||M_{J;\tau'}(q)||j_N\rangle \\
+\frac{|\vec{q}|^2}{m_N^2}R_{\Phi''}^{\tau\tau'}(|\vec{v}^{\perp}_{\text{inel}\,T}|^2,\frac{|\vec{q}|^2}{m_N^2})\langle j_N||\Phi''_{J;\tau}(q)||j_N\rangle\langle j_N||\Phi''_{J;\tau'}(q)||j_N\rangle \\
+\frac{|\vec{q}|^2}{m_N^2}R_{\Phi''M}^{\tau\tau'}(|\vec{v}^{\perp}_{\text{inel}\,T}|^2,\frac{|\vec{q}|^2}{m_N^2})\langle j_N||\Phi''_{J;\tau}(q)||j_N\rangle\langle j_N||M_{J;\tau'}(q)||j_N\rangle\Bigg] \\
+\sum_{J=2,4,\ldots}^{\infty}\left[\frac{|\vec{q}|^2}{m_N^2}R_{\tilde{\Phi}'}^{\tau\tau'}(|\vec{v}^{\perp}_{\text{inel}\,T}|^2,\frac{|\vec{q}|^2}{m_N^2})\langle j_N||\tilde{\Phi}'_{J;\tau}(q)||j_N\rangle\langle j_N||\tilde{\Phi}'_{J;\tau'}(q)||j_N\rangle\right] \\
+\sum_{J=1,3,\ldots}^{\infty}\Bigg[R_{\Sigma''}^{\tau\tau'}(|\vec{v}^{\perp}_{\text{inel}\,T}|^2,\frac{|\vec{q}|^2}{m_N^2})\langle j_N||\Sigma''_{J;\tau}(q)||j_N\rangle\langle j_N||\Sigma''_{J;\tau'}(q)||j_N\rangle \\
+R_{\Sigma'}^{\tau\tau'}(|\vec{v}^{\perp}_{\text{inel}\,T}|^2,\frac{|\vec{q}|^2}{m_N^2})\langle j_N||\Sigma'_{J;\tau}(q)||j_N\rangle\langle j_N||\Sigma'_{J;\tau'}(q)||j_N\rangle \\
+\frac{|\vec{q}|^2}{m_N^2}R_{\Delta}^{\tau\tau'}(|\vec{v}^{\perp}_{\text{inel}\,T}|^2,\frac{|\vec{q}|^2}{m_N^2})\langle j_N||\Delta_{J;\tau}(q)||j_N\rangle\langle j_N||\Delta_{J;\tau'}(q)||j_N\rangle \\
+\frac{|\vec{q}|^2}{m_N^2}R_{\Delta\Sigma'}^{\tau\tau'}(|\vec{v}^{\perp}_{\text{inel}\,T}|^2,\frac{|\vec{q}|^2}{m_N^2})\langle j_N||\Delta_{J;\tau}(q)||j_N\rangle\langle j_N||\Sigma'_{J;\tau'}(q)||j_N\rangle\Bigg]\Bigg\}.
\end{aligned} \tag{3.37}$$

This result is expanded in spherical harmonics leading to the nuclear operators $M, \Delta, \Sigma', \Sigma'', \tilde{\Phi}', \Phi''$. The inelastic kinematics does not modify these operators, so we do not reproduce their expressions. Instead, the changes are solely in the R

coefficients

$$
\begin{aligned}
R_M^{\tau\tau'}(|\vec{v}_T|^2, \frac{|\vec{q}|^2}{m_N^2}, \delta) &= c_1^\tau c_1^{\tau'*} + \frac{j_\chi(j_\chi+1)}{3}\left[\left(\frac{|\vec{q}|^2}{m_N^2}c_5^\tau c_5^{\tau'*} + c_8^\tau c_8^{\tau'*}\right)\left(|\vec{v}_T|^2 - v_{\min T}^2(\delta)\right)\right. \\
&\quad \left. + \frac{|\vec{q}|^2}{m_N^2}c_{11}^\tau c_{11}^{\tau'*}\right] \\
R_{\Phi''}^{\tau\tau'}(|\vec{v}_T|^2, \frac{|\vec{q}|^2}{m_N^2}, \delta) &= \frac{1}{4}\frac{|\vec{q}|^2}{m_N^2}c_3^\tau c_3^{\tau'*} + \frac{j_\chi(j_\chi+1)}{12}\left(c_{12}^\tau - \frac{|\vec{q}|^2}{m_N^2}c_{15}^\tau\right)\left(c_{12}^{\tau'*} - \frac{|\vec{q}|^2}{m_N^2}c_{15}^{\tau'*}\right) \\
R_{\Phi''M}^{\tau\tau'}(|\vec{v}_T|^2, \frac{|\vec{q}|^2}{m_N^2}, \delta) &= \mathrm{Re}\left[c_3^\tau c_1^{\tau'*} + \frac{j_\chi(j_\chi+1)}{3}\left(c_{12}^\tau - \frac{|\vec{q}|^2}{m_N^2}c_{15}^\tau\right)c_{11}^{\tau'*}\right] \\
R_{\tilde{\Phi}'}^{\tau\tau'}(|\vec{v}_T|^2, \frac{|\vec{q}|^2}{m_N^2}, \delta) &= \frac{j_\chi(j_\chi+1)}{12}\left[c_{12}^\tau c_{12}^{\tau'*} + \frac{|\vec{q}|^2}{m_N^2}c_{13}^\tau c_{13}^{\tau'*}\right] \\
R_{\Sigma''}^{\tau\tau'}(|\vec{v}_T|^2, \frac{|\vec{q}|^2}{m_N^2}, \delta) &= \frac{1}{4}\frac{|\vec{q}|^2}{m_N^2}c_{10}^\tau c_{10}^{\tau'*} + \frac{j_\chi(j_\chi+1)}{12}\left[c_4^\tau c_4^{\tau'*} + \frac{|\vec{q}|^2}{m_N^2}\left(c_4^\tau c_6^{\tau'*} + c_6^\tau c_4^{\tau'*}\right)\right. \\
&\quad \left. + \frac{|\vec{q}|^4}{m_N^4}c_6^\tau c_6^{\tau'*} + \left(c_{12}^\tau c_{12}^{\tau'*} + \frac{|\vec{q}|^2}{m_N^2}c_{13}^\tau c_{13}^{\tau'*}\right)\left(|\vec{v}_T|^2 - v_{\min T}^2(\delta)\right)\right] \\
R_{\Sigma'}^{\tau\tau'}(|\vec{v}_T|^2, \frac{|\vec{q}|^2}{m_N^2}, \delta) &= \frac{1}{8}\left[\frac{|\vec{q}|^2}{m_N^2}c_3^\tau c_3^{\tau'*} + c_7^\tau c_7^{\tau'*}\right]\left(|\vec{v}_T|^2 - v_{\min T}^2(\delta)\right) + \frac{j_\chi(j_\chi+1)}{12}\left\{c_4^\tau c_4^{\tau'*}\right. \\
&\quad + \frac{|\vec{q}|^2}{m_N^2}c_9^\tau c_9^{\tau'*} \\
&\quad + \frac{1}{2}\left[\left(c_{12}^\tau - \frac{|\vec{q}|^2}{m_N^2}c_{15}^\tau\right)\left(c_{12}^{\tau'*} - \frac{|\vec{q}|^2}{m_N^2}c_{15}^{\tau'*}\right) + \frac{|\vec{q}|^2}{m_N^2}c_{14}^\tau c_{14}^{\tau'*}\right] \\
&\quad \left.\times\left(|\vec{v}_T|^2 - v_{\min T}^2(\delta)\right)\right\} \\
R_{\Delta}^{\tau\tau'}(|\vec{v}_T|^2, \frac{|\vec{q}|^2}{m_N^2}, \delta) &= \frac{j_\chi(j_\chi+1)}{3}\left[\frac{|\vec{q}|^2}{m_N^2}c_5^\tau c_5^{\tau'*} + c_8^\tau c_8^{\tau'*}\right] \\
R_{\Delta\Sigma'}^{\tau\tau'}(|\vec{v}_T|^2, \frac{|\vec{q}|^2}{m_N^2}, \delta) &= \frac{j_\chi(j_\chi+1)}{3}\mathrm{Re}\left[c_5^\tau c_4^{\tau'*} - c_8^\tau c_9^{\tau'*}\right].
\end{aligned}
\tag{3.38}
$$

Here we have expanded $|\vec{v}_{\mathrm{inel}\,T}^{\perp}|^2$ as in Eq. 3.13 to show the dependence on δ, and we have also included the appropriate complex conjugation of the coefficients as relativistic inelastic dark matter operators can produce complex coefficients for their nonrelativistic counterparts.

CHAPTER IV

NAKM

This chapter is work done by myself, Spencer Chang, and Gabriel Barello [36].

Introduction

Kinetic mixing (KM) is a phenomenon that produces an interaction between gauge bosons of two different gauge groups, and generically occurs when there are two U(1) gauge symmetries in a theory. KM will be generated by loop processes whenever there are particles charged under both symmetries [38, 112]. This makes KM a common ingredient of models beyond the standard model (SM) of particle physics. In Z' [112] and many dark matter models [113, 114], the SM is supplemented by an additional U(1) gauge symmetry which can mix with $\mathrm{U}(1)_Y$. Such models have motivated a large and diverse experimental effort with current and upcoming searches at intensity frontier experiments (fixed-target and flavor factories) and the LHC (see [37] for overview and references). The main focus of these searches and models has been on the dynamics of the dark photon or signals of particles charged only under the dark sector, while little attention has been paid to the aforementioned particle charged under both symmetries, which mediates KM.

The reason this mediating particle is ignored is that it's mass can usually be made large while leaving the KM strength fixed. In the most studied case of KM between two abelian sectors, where the mixing operator is dimension four, the mediator mass only logarithmically affects the strength of KM. Moreover, KM between abelian sectors is described by a renormalizable operator, so it can be included without

reference to a mediator. Thus, in the abelian case, it is not guaranteed that the mediator will be light enough to be discovered. On the other hand, when KM goes through a nonabelian gauge sector, the operator is nonrenormalizable and inextricably linked to a mass scale. This fact gives nonabelian kinetic mixing models unique predictive power which has not yet been studied in the literature. This study fills that gap. Furthermore, as we will show, nonabelian KM strengths relevant for current intensity frontier experiments is unambiguously linked to a weak scale mediator, predicting a correlated signal at the energy frontier. Although such nonabelian mixing is already well known in the literature this study represents the first statement of this connection, and the first presentation of a model where a nonabelian operator is the sole origin of KM.

In this paper we discuss a case of particular modern interest: an abelian dark sector mixing with $\mathrm{SU}(2)_L$ of the SM. The lowest dimensional operator involving only SM fields and the dark photon which kinetically mixes $\mathrm{SU}(2)_L$ and the dark photon is

$$\frac{c}{16\pi^2 m_\phi^2}\left(H^\dagger \tau^a H\right) W^a_{\mu\nu} F_D^{\mu\nu} \tag{4.1}$$

where $W^a_{\mu\nu}(F_D^{\mu\nu})$ is the field strength of the SM $\mathrm{SU}(2)_L$ gauge boson (dark gauge boson), H is the SM higgs field, and τ^a are the Pauli matrices divided by two. Anticipating the origin of this operator, we include the mass of the mediator m_ϕ, a loop factor, and absorb $O(1)$ numbers and couplings into the coefficient c. Once electroweak symmetry is broken, Eq. 4.1 contains the canonical mixing between the photon and the dark photon

$$\frac{\epsilon}{2} F_{\mu\nu} F_D^{\mu\nu}; \qquad \epsilon = \frac{c\, v^2 s_W}{32\pi^2 m_\phi^2} \tag{4.2}$$

where s_W is the sine of the electroweak mixing angle, and v is the SM higgs vacuum expectation value (vev). Already this expression shows a connection between intensity and energy frontier experiments: planned searches for the dark photon include *i*) fixed target experiments, probing the region $\epsilon \sim 10^{-5} - 10^{-4}$ for a dark photon of mass $M_{A_D} \sim 10 - 200$ MeV and $\epsilon \gtrsim 3 \times 10^{-4}$ for $M_{A_D} \sim 10 - 600$ MeV (*e.g.* APEX [115] and HPS [116]), *ii*) next generation flavor factories, sensitive to $\epsilon \sim 10^{-4} - 10^{-3}$ for dark photon masses up to 10 GeV [37] (going beyond existing BABAR, BESIII limits [117, 118]), and *iii*) a proposed LHCb search sensitive to the range $\epsilon \sim 10^{-5} - 10^{-3}$ and $M_{A_D} \leq 100$ MeV [119]. In our models of interest, Eq. 4.3 shows that this parameter space requires

$$m_\phi = \sqrt{\frac{c\, v^2 s_W}{32\pi^2 \epsilon}} \sim \sqrt{\frac{c}{\epsilon/10^{-4}}} \times 1\,\text{TeV}. \tag{4.3}$$

Thus, in theories with only nonabelian kinetic mixing, there is a strong correlation between signals of dark photons at the intensity frontier and the corresponding mediator particles at the LHC. This conclusion is independent of the specific realization of nonabelian KM.

In the rest of this paper we present a simple model where the only KM that occurs is nonabelian. In such scenarios, the mediator particle's signals at the LHC are correlated with the dark photon searches of the intensity frontier. We will analyze the model's dynamics and then discuss the mediator particle's phenomenology and relevant constraints.

Model

In this model, there is a dark gauge symmetry $\mathrm{U}(1)_D$ with a dark photon, A_D. The field mediating KM is a scalar $\mathrm{SU}(2)_L$ triplet with unit dark charge that we call ϕ. In order to give the dark photon mass we introduce a dark higgs, H_D, with unit dark charge that gets a vev $\langle H_D \rangle = v_D/\sqrt{2}$. The most general, renormalizable theory with these fields has many terms in its scalar potential. Only a subset of them will be relevant for our discussion, and the terms we study are

$$\begin{aligned} V(H, H_d, \phi) &= \lambda|H|^4 - \mu^2|H|^2 + \lambda_D|H_D|^4 - \mu_D^2|H_D|^2 \\ &\quad + m_\phi^2|\phi|^2 + \lambda_{\mathrm{mix}}(\phi^\dagger T^a \phi)(H^\dagger \tau^a H) \\ &\quad + \kappa\left[\phi^a (H^\dagger \tau^a H) H_D^\dagger + \mathrm{h.c.}\right] \end{aligned} \tag{4.4}$$

where κ can be taken to be real after a field redefinition and T^a is the triplet representation's generators for $\mathrm{SU}(2)_L$. Of particular importance is the term with coefficient λ_{mix} as it is responsible for KM. After integrating out ϕ, KM is generated with strength

$$\epsilon = \frac{g g_D \lambda_{\mathrm{mix}}}{96\pi^2} \frac{v^2}{m_\phi^2} s_W \sim 10^{-4}\, g_D\, \lambda_{\mathrm{mix}} \left(\frac{400\ \mathrm{GeV}}{m_\phi}\right)^2 \tag{4.5}$$

where g is the gauge coupling for $\mathrm{SU}(2)_L$, and g_D is the dark gauge coupling. As the final expression shows, if the new couplings are order one, mixings relevant to intensity frontier experiments are spanned by m_ϕ in the range $100\ \mathrm{GeV} - 1\ \mathrm{TeV}$.

This model does not contain a particle charged under both $\mathrm{U}(1)_D$ and hypercharge so there is no abelian kinetic mixing. If, for example, this model were embedded into a grand unified theory (GUT), particles with GUT-scale masses may generate abelian kinetic mixing, however in that case abelian kinetic mixing would

arise from two-loop diagrams and would generate mixing strengths on the order $\epsilon \sim 10^{-6} - 10^{-4}$ as discussed in [120]. In this model nonabelian kinetic mixing is dominant over, or of comparable strength to, abelian mixing. This means that we can use Eq. 4.5 to predict the mediator mass from the kinetic mixing strength.

Mass Spectrum

The term responsible for KM also generates a mass splitting in the ϕ states. Two states, labeled $\chi^{\pm}$ and $\eta^{\pm}$, are charged under electromagnetism and have masses

$$m_{\chi}^2 = m_{\phi}^2 + \frac{\lambda_{\text{mix}} v^2}{4}, \quad m_{\eta}^2 = m_{\phi}^2 - \frac{\lambda_{\text{mix}} v^2}{4}. \tag{4.6}$$

This splitting can cause the lightest charged state's mass to become tachyonic, spontaneously breaking $\text{U}(1)_{EM}$ and giving the photon mass. This places a constraint that $m_{\phi}^2 > \lambda_{\text{mix}} v^2/4$.

The two remaining, neutral degrees of freedom are the real and imaginary parts of the third component of ϕ, denoted ϕ_R^0 and ϕ_I^0, respectively. These states will be nearly degenerate with mass m_{ϕ} – a very small splitting is generated which vanishes as $\kappa \to 0$. Throughout we will use ϕ to refer to all of these states collectively and their individual names when specificity is required.

Potential Minimization

The κ term in the potential was introduced in order for the ϕ particles to decay, but also has other important effects that can constrain the model. Once

the electroweak and dark symmetries are broken, this term induces a vev for the real, neutral component of ϕ. The size of this vev is

$$\langle \phi \rangle = \frac{\kappa v^2 v_D}{4\sqrt{2} m_\phi^2}. \tag{4.7}$$

Since this is only in the neutral component, $\mathrm{U}(1)_{EM}$ remains unbroken, but it does shift the W boson mass, with a contribution to the T parameter

$$T_{\langle \phi \rangle} \sim 10^{-3}\, \kappa^2 \left(\frac{v_D}{1\ \mathrm{GeV}} \right)^2 \left(\frac{200\ \mathrm{GeV}}{m_\phi} \right)^4, \tag{4.8}$$

which is very small as long as the dark photon scale is sub-GeV. In addition, there is a one loop contribution to T from the ϕ particles due to their mass splitting [121] which in the limit of small splitting goes as

$$T_{\mathrm{loop}} \sim \frac{\lambda_{\mathrm{mix}}^2 v^4}{192\pi s_W^2 c_W^2 m_Z^2 m_\phi^2} \sim 0.1\, \lambda_{\mathrm{mix}}^2 \left(\frac{200\ \mathrm{GeV}}{m_\phi} \right)^2. \tag{4.9}$$

Contributions to S are negligible, so to be consistent with electroweak precision constraints requires $T < 0.2$ (95% C.L.) [1], putting a lower bound on m_ϕ (from Eq. 4.9) and an upper bound on κ (from Eq. 4.8).

The κ term also causes mixing between ϕ_R^0, h_D, and the SM higgs. This leads to a correction to the μ_D^2 term of size $\kappa^2 v^4/(16 m_\phi^2)$. Thus, a large hierarchy between the dark and electroweak scales requires a tuning in the value of μ_D^2. The severity of this tuning depends on κ, and for certain regions of parameter space this tuning can be small. It is however interesting that the tuning in this model is indirectly observable. This is in contrast to the SM where the details of tuning depend on some unknown,

as-of-yet-unobservable higher scale. If KM with $SU(2)_L$ is observed, this model will provide insight into the validity of tuning as a theoretical constraint.

Fixed Target Benchmark

Now lets consider a benchmark set of parameters, chosen in order to remain within the region of immediate interest to fixed-target experiments: $m_{A_D} = 0.1$ GeV and $g_D = 0.5$. This choice implies that $v_D = 0.2$ GeV, and we set $m_{h_D} = 0.4$ GeV so that the dark higgs can decay into two dark photons. Note that the dark higgs and photon masses are negligibly small relative to electroweak scale masses, so we can safely neglect them in later formulas. We also set $\lambda_{\text{mix}} = 1$ which puts a lower limit on m_ϕ of 155 GeV due to the electroweak precision constraint. In our analysis we specifically explore the range 150 GeV $< m_\phi <$ 500 GeV in order to be relevant for collider searches while remaining in the $10^{-5} < \epsilon < 10^{-3}$ window, though it should be kept in mind that precision electroweak constraints exclude the small part of this region $m_\phi <$ 155 GeV.

Decays

A ϕ particle can decay directly into gauge and higgs bosons through the κ term, or undergo cascade decays through its mass states by radiating $W^{(*)}$ bosons. The cascade decay rate, in the large m_ϕ and massless fermion limit, is

$$\Gamma(\chi^\pm \to W^{\pm *}\phi^0_{R,I}) = \Gamma(\phi^0_{R,I} \to W^{\mp *}\eta^\pm) = \sum_{f\bar{f}'} \frac{N_c G_f^2 \Delta m^5}{15\pi^3} \tag{4.10}$$

where G_f is the Fermi constant, Δm is the mass splitting between ϕ states, and $f\bar{f}'$ includes all fermion pairs except the top-bottom pair for which the splitting Δm is

too small to produce. The κ mediated decay rates, in the limit that $m_{h_D}, m_{A_D} \to 0$, are

$$\begin{aligned}
\Gamma(\phi_R^0 \to h h_D) &= \Gamma(\phi_I^0 \to h A_D) = \frac{\kappa^2 v^2}{64\pi m_\phi^3}\left(m_\phi^2 - m_h^2\right), \\
\Gamma(\chi^\pm \to W^\pm h_D) &= \Gamma(\chi^\pm \to W^\pm A_D) \\
&= \frac{\kappa^2 v^2}{128\pi m_\phi^4 m_\chi^3}\left(m_\chi^2 - m_W^2\right)^3, \text{ and} \\
\Gamma(\eta^\pm \to W^\pm h_D) &= \Gamma(\eta^\pm \to W^\pm A_D) \\
&= \frac{\kappa^2 v^2}{128\pi m_\phi^4 m_\eta^3}\left(m_\eta^2 - m_W^2\right)^3.
\end{aligned} \tag{4.11}$$

The decay phenomenology depends sensitively on κ. If κ is sufficiently small the cascade decays will dominate, and heavier ϕ will tend to decay down to the lightest state, $\eta^\pm$, emitting two fermions via an off-shell W per step, followed by the $\eta^\pm$ decaying half the time to $W^\pm h_D$ and half the time to $W^\pm A_D$. On the other hand, if κ is large, κ mediated decays dominate with the neutral components of ϕ decaying as $\phi_R^0 \to h h_D, \phi_I^0 \to h A_D$ and $\eta^\pm, \chi^\pm$ decaying to $W^\pm h_D, W^\pm A_D$ equally. Note that the simplicity of the decays are a consequence of our benchmark choice. As the value of v_D is increased from our benchmark, additional decay modes due to κ become more important, *e.g.* $\phi_R^0 \to hh, ZZ, WW$ and $\eta^\pm \to W^\pm h, W^\pm Z$. However, since these decay rates are proportional to v_D^2, only when $v_D \gtrsim 100$ GeV do these start to become important and thus in the intensity frontier parameter space we do not expect these decays to have appreciable rates.

In Fig. 20, we highlight some of the important regions of our benchmark parameter space. Some characteristic values of ϵ are given at three m_ϕ values in dashed lines, though these can be scaled up or down by changes in $g_D, \lambda_{\rm mix}$. The green line denotes the value of κ where the cascade decays are comparable to the κ

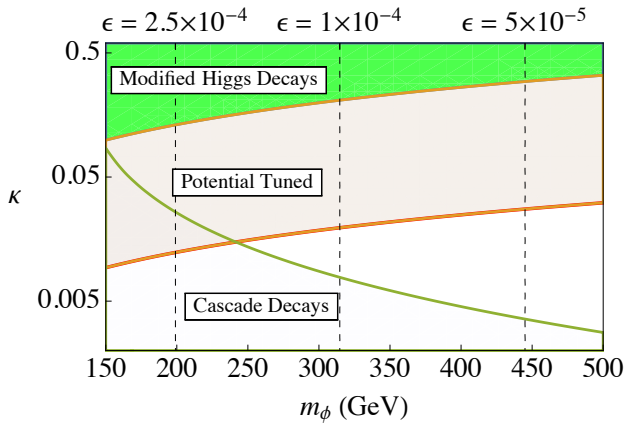

FIGURE 20. Regions of interest in the (m_ϕ,κ) plane.
This figure shows regions of interest in the (m_ϕ,κ) plane. Starting from the top, the regions are where the new higgs decays are greater than 10% of its SM expected total width (green region), where μ_D^2 is tuned to $> 10\%$ (above the thick orange curve) and where the electroweak cascade decays are faster than the κ decays (below the green curve). Vertical dashed lines mark values of ϵ, labeled at the top.

induced decays below which the off-shell cascade decays dominate. The middle region of Fig. 20 shows where the tuning in μ_D^2 is worse than 10%, and the last region at the top shows when the SM higgs has new decays with a branching ratio greater than 10%, which will be discussed below.

Production Rates

In order to observe these decays, ϕ particles will need to be produced, which at a hadron collider proceeds predominantly through Drell-Yan production. The production cross sections at the 13 TeV LHC are shown in Fig. 21. We used FeynRules [122] to generate our Lagrangian and CalcHEP [123] to generate the events using the `cteq6l` parton distribution function for the proton. Pair production of the neutral particles does not occur due to the lack of photon, Z couplings. Also, production rates for ϕ_I^0 are identical to ϕ_R^0 and so are not included on the plot.

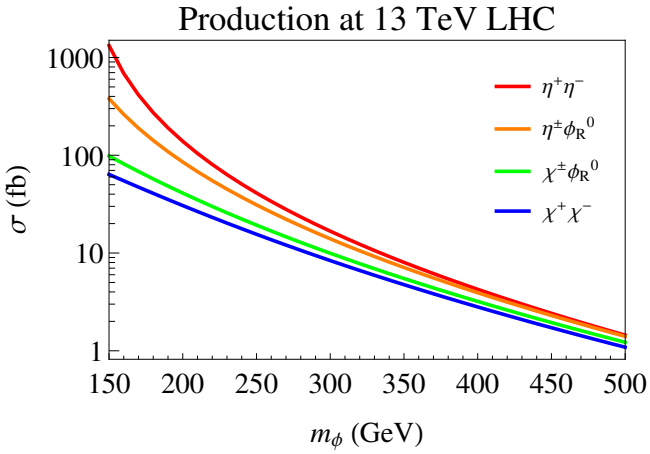

FIGURE 21. Production cross section.
This figure shows the pair production cross section for various mass states of ϕ at the $\sqrt{s} = 13\,\text{TeV}$ LHC. The different curves are: two η states (red), an η and a ϕ_R^0 or ϕ_I^0 (orange) a χ and a ϕ_R^0 or ϕ_I^0 (green) and two χ states (blue). The legend is arranged in order of decreasing cross section. Curves were generated using the `cteq6l` parton distribution function of CalcHEP [123].

The strategy for ϕ searches should start with adaptations to the existing searches for dark photons and lepton jets [39, 120, 124, 125]. All events contain either h_D or A_D particles produced at significant boosts, which coupled with the decay $h_D \to A_D A_D$, will lead to many events with boosted lepton pairs. For small enough ϵ, many of these A_D decays will be displaced. If the value of κ is small, where cascade decays dominate, there will also be soft leptons or jet activity from the off-shell W's. An interesting signal in this regime is the possibility of same sign η production due to the cascade decays of ϕ_R^0, ϕ_I^0 going equally into $\eta^\pm$ (see Eq. 4.10). Their subsequent decay produces a like-sign pair of W's leading to same sign lepton events in addition to the lepton jets of the event. On the other hand, if the value of κ is large, there can be other associated objects like the SM higgs bosons produced in ϕ_R^0, ϕ_I^0 decays (see Eq. 4.11), which could be of interest in terms of tagging or reconstructing the events.

To summarize, this scenario's predominant collider signal is lepton jets in association with W, h with mass resonances between a lepton jet and the W or h.

Since the benchmark's dark photon mass restricts it to electron decays, the lepton jets could be challenging to pick out. Boosted electron pairs are much more difficult to distinguish from jets and in fact, most existing lepton jet searches rely on muons (with significant constraints only for $M_{A_D} > 2m_\mu \sim 0.2$ GeV). To overcome these challenges, some promising strategies could be to look for displaced jets and/or jets with significant electromagnetic energy deposit. We leave studies of such issues as well as existing LHC constraints and discovery reach for such particles to future work.

SM Higgs Phenomenology

This model also predicts new decays for the SM higgs. The dominant new decays are into dark higgs bosons and dark gauge bosons. The kinetic mixing operator itself, Eq. 4.1, generates new decays of the higgs to a dark photon and either a Z or a photon. The rates of these decays are

$$\Gamma(h \to h_D h_D) = \Gamma(h \to A_D A_D) = \frac{\kappa^4 v^6}{512\pi m_h m_\phi^4} \tag{4.12}$$

$$\Gamma(h \to \gamma_D \gamma) = v\frac{\epsilon^2}{32\pi}\left(\frac{m_h}{v}\right)^3 \tag{4.13}$$

$$\Gamma(h \to \gamma_D Z) \cong \Gamma(h \to \gamma_D \gamma) \times \left(\frac{2\, c_W}{s_W}\right)^2 \times 10^{-1} \tag{4.14}$$

again we take the limit where A_D and h_D are massless. Indirectly, these new decay widths are constrained by the relatively good fits of the SM higgs decay signal strengths [21]. As an approximation of this constraint, the top green region of Fig. 20 shows where higgs decays into the dark sector exceed 10% of the SM higgs total width. In particular, decays of the higgs involving the dark photon are a direct consequence

of the kinetic mixing term, and provide a model independent signal of nonabelian kinetic mixing. For $\epsilon \sim 10^{-3}$ the branching ratio of the higgs to a dark photon will be $\Gamma(h \to \gamma_D + Z/\gamma) \sim .5 \times 10^{-6}$ GeV. There is potential for the LHC to detect these higgs decays, if the dark photon is heavier than our benchmark. For example, if $m_{A_D} \sim 0.6 - 60$ GeV, the LHC can be sensitive to the dark photon through higgs decays into $2A_D$ [126] and a recent LHC analysis constrains $Br(h \to 2A_D) \gtrsim 3 \times 10^{-4}$ for $m_{A_D} = 15 - 60$ GeV [127]. While the fixed target parameter space motivates searches at much lower dark photon masses, a simple modification of our benchmark can give these heavier masses. In these modified benchmarks, if one improves the higgs branching ratio constraint to $BR_{\text{new}} < BR_{\text{limit}}$, this would constrain the range $\kappa > 0.25(m_\phi/200 \text{ GeV}) Br_{\text{limit}}^{1/4}$. As our formulas and discussion show, increasing m_{A_D} to these larger values, either through increasing g_D or v_D, changes very little in the ϕ phenomenology, however, in this heavier parameter space correlated signals at the intensity frontier could only be seen at future flavor factories for $m_{A_D} < 10$ GeV.

Conclusions

In this letter, we have argued for a direct connection between current intensity frontier searches for dark photons and the signals of new particles at the LHC. The connection occurs if KM involves a nonabelian gauge symmetry, since the mixing operator requires higgs fields to be gauge invariant and thus closely ties the mediator particle mass to the vev of the higgs and the strength of KM. To illustrate this, we wrote down a simple model where the only KM which occurs is between a new dark U(1) gauge symmetry and $SU(2)_L$. This requires a scalar triplet ϕ of $SU(2)_L$ which is charged under the dark U(1). Analyzing the model, we looked at the constraints

and briefly considered the phenomenology of the ϕ particles at the LHC which could be searched through simple modifications of existing dark photon searches.

Aside from our simple model, there are obvious extensions to explore. Fermionic mediators, mixing with a nonabelian dark gauge symmetry and incorporating dark matter are all intriguing modifications, which will all produce the same, model-independent correlation of signals. Interestingly, these directions all tend to lead to larger multiplicity in the dark sector, suggesting that the model in this paper is unique in its simplicity. Investigation of these directions, as well as a detailed collider study of this model is forthcoming.

To conclude, KM of the $\mathrm{SU}(2)_L$ of the SM and an abelian dark sector is timely and well motivated given the current run of the LHC, ongoing fixed target experiments, and potential next generation flavor factories. The connection it draws between intensity and energy frontier experiments is unambiguous and leads to correlated signals at these experiments, promising unprecedented insight into the physics of the dark sector.

CHAPTER V

CONCLUSION

In this dissertation I have presented three papers that examine and define methods for looking beyond the standard model of particle physics. First we have a means of enhancing the SM Higgs couplings to fermions and gauge bosons. This is unusual for extended Higgs sector models, and can provide an explanation if the best fit point for the couplings is indeed larger than the SM. Second we looked at inelastic DM, an intriguing change to the standard kinematics most searches for DM assume. Our modification of Anand *et al.*'s code allow many theories for this type of DM to be tested easily, and we also showed that increasing the energy window in which direct detection experiments search can be beneficial to finding inelastic particles. Finally we examined the strange phenomenon known as kinetic mixing and found an esoteric connection between the strength of this mixing and the mass of the new particle responsible for this mixing so long as the mixing is between a nonabelian and Abelian symmetry.

This is an interesting time for particle physics. Many exciting discoveries, or disappointing fluctuations, are rearing their heads and the works contained herein may provide answers for what these are, or what to expect next.

REFERENCES CITED

[1] K.A. Olive et al. Review of Particle Physics. *Chin.Phys.*, C38:090001, 2014.

[2] D. Hanneke, S. Fogwell, and G. Gabrielse. New Measurement of the Electron Magnetic Moment and the Fine Structure Constant. *Phys. Rev. Lett.*, 100:120801, 2008.

[3] T. Aoyama, M. Hayakawa, T. Kinoshita, and M. Nio. Revised value of the eighth-order QED contribution to the anomalous magnetic moment of the electron. *Phys. Rev.*, D77:053012, 2008.

[4] G. W. Bennett et al. Final Report of the Muon E821 Anomalous Magnetic Moment Measurement at BNL. *Phys. Rev.*, D73:072003, 2006.

[5] Michel Davier, Andreas Hoecker, Bogdan Malaescu, and Zhiqing Zhang. Reevaluation of the Hadronic Contributions to the Muon g-2 and to alpha(MZ). *Eur. Phys. J.*, C71:1515, 2011. [Erratum: Eur. Phys. J.C72,1874(2012)].

[6] T. Teubner, K. Hagiwara, R. Liao, A. D. Martin, and D. Nomura. g-2 of the muon and Delta alpha re-evaluated. *Nucl. Phys. Proc. Suppl.*, 218:225–230, 2011.

[7] J. Albrecht et al. Working Group Report: Charged Leptons. In *Community Summer Study 2013: Snowmass on the Mississippi (CSS2013) Minneapolis, MN, USA, July 29-August 6, 2013*, 2013.

[8] Wolfgang Pauli. Open letter to the group of radioactive people at the Gauverein meeting in Tubingen. 1930.

[9] C. L. Cowan, F. Reines, F. B. Harrison, H. W. Kruse, and A. D. McGuire. Detection of the free neutrino: A Confirmation. *Science*, 124:103–104, 1956.

[10] S. L. Glashow, J. Iliopoulos, and L. Maiani. Weak Interactions with Lepton-Hadron Symmetry. *Phys. Rev.*, D2:1285–1292, 1970.

[11] J. J. Aubert et al. Experimental Observation of a Heavy Particle J. *Phys. Rev. Lett.*, 33:1404–1406, 1974.

[12] J. E. Augustin et al. Discovery of a Narrow Resonance in e+ e- Annihilation. *Phys. Rev. Lett.*, 33:1406–1408, 1974. [Adv. Exp. Phys.5,141(1976)].

[13] Georges Aad et al. Observation of a new particle in the search for the standard model higgs boson with the atlas detector at the lhc. *Physics Letters B*, 716(1):1 – 29, 2012.

[14] Serguei Chatrchyan et al. Observation of a new boson at a mass of 125 gev with the cms experiment at the lhc. *Physics Letters B*, 716(1):30 – 61, 2012.

[15] Combined coupling measurements of the Higgs-like boson with the ATLAS detector using up to 25 fb^{-1} of proton-proton collision data. Technical Report ATLAS-CONF-2013-034, CERN, Geneva, Mar 2013.

[16] Spencer Chang, Christopher A. Newby, Nirmal Raj, and Chaowaroj Wanotayaroj. Revisiting Theories with Enhanced Higgs Couplings to Weak Gauge Bosons. *Phys. Rev.*, D86:095015, 2012.

[17] Howard Georgi and Marie Machacek. DOUBLY CHARGED HIGGS BOSONS. *Nucl.Phys.*, B262:463, 1985.

[18] Ian Low, Riccardo Rattazzi, and Alessandro Vichi. Theoretical Constraints on the Higgs Effective Couplings. *JHEP*, 1004:126, 2010.

[19] Adam Falkowski, Slava Rychkov, and Alfredo Urbano. What if the Higgs couplings to W and Z bosons are larger than in the Standard Model? *JHEP*, 1204:073, 2012.

[20] Michael E. Peskin and Tatsu Takeuchi. Estimation of oblique electroweak corrections. *Phys.Rev.*, D46:381–409, 1992.

[21] Measurements of the Higgs boson production and decay rates and constraints on its couplings from a combined ATLAS and CMS analysis of the LHC pp collision data at sqrt(s) = 7 and 8 TeV. Technical Report ATLAS-CONF-2015-044, CERN, Geneva, Sep 2015.

[22] P. Cushman, C. Galbiati, D.N. McKinsey, H. Robertson, T.M.P. Tait, et al. Working Group Report: WIMP Dark Matter Direct Detection. 2013.

[23] J. L. Feng et al. Planning the Future of U.S. Particle Physics (Snowmass 2013): Chapter 4: Cosmic Frontier. In *Community Summer Study 2013: Snowmass on the Mississippi (CSS2013) Minneapolis, MN, USA, July 29-August 6, 2013*, 2014.

[24] J. Angle et al. Constraints on inelastic dark matter from XENON10. *Phys.Rev.*, D80:115005, 2009.

[25] E. Aprile et al. Dark Matter Results from 225 Live Days of XENON100 Data. *Phys.Rev.Lett.*, 109:181301, 2012.

[26] D.S. Akerib et al. First results from the LUX dark matter experiment at the Sanford Underground Research Facility. *Phys.Rev.Lett.*, 112:091303, 2014.

[27] Z. Ahmed et al. Search for inelastic dark matter with the CDMS II experiment. *Phys.Rev.*, D83:112002, 2011.

[28] E. Behnke et al. First Dark Matter Search Results from a 4-kg CF_3I Bubble Chamber Operated in a Deep Underground Site. *Phys.Rev.*, D86:052001, 2012.

[29] R. Bernabei, P. Belli, F. Cappella, V. Caracciolo, S. Castellano, et al. Final model independent result of DAMA/LIBRA-phase1. *Eur.Phys.J.*, C73:2648, 2013.

[30] G. Barello, Spencer Chang, and Christopher A. Newby. A Model Independent Approach to Inelastic Dark Matter Scattering. *Phys. Rev.*, D90(9):094027, 2014.

[31] David Tucker-Smith and Neal Weiner. The Status of inelastic dark matter. *Phys.Rev.*, D72:063509, 2005.

[32] A. Liam Fitzpatrick, Wick Haxton, Emanuel Katz, Nicholas Lubbers, and Yiming Xu. The Effective Field Theory of Dark Matter Direct Detection. *JCAP*, 1302:004, 2013.

[33] Nikhil Anand, A. Liam Fitzpatrick, and W.C. Haxton. Model-independent WIMP Scattering Responses and Event Rates: A Mathematica Package for Experimental Analysis. 2013.

[34] Spencer Chang, Neal Weiner, and Itay Yavin. Magnetic Inelastic Dark Matter. *Phys.Rev.*, D82:125011, 2010.

[35] J.I. Collar. Quenching and channeling of nuclear recoils in NaI(Tl): Implications for dark-matter searches. *Phys.Rev.*, C88(3):035806, 2013.

[36] G. Barello, Spencer Chang, and Christopher A. Newby. Correlated Signals at the Energy and Intensity Frontiers from Nonabelian Kinetic Mixing. 2015.

[37] Rouven Essig et al. Working Group Report: New Light Weakly Coupled Particles. In *CSS 2013: Snowmass*, 2013.

[38] Bob Holdom. Two U(1)'s and Epsilon Charge Shifts. *Phys.Lett.*, B166:196, 1986.

[39] Georges Aad et al. A search for prompt lepton-jets in pp collisions at $\sqrt{s} = 8$ TeV with the ATLAS detector. *JHEP*, 02:062, 2016.

[40] Updated combination of cdf and d's searches for standard model higgs boson production with up to 10.0 fb-1 of data. Technical Report FERMILAB-CONF-12-318-E, FNAL, June 2012.

[41] Aleksandr Azatov, Roberto Contino, and Jamison Galloway. Model-Independent Bounds on a Light Higgs. *JHEP*, 1204:127, 2012.

[42] Dean Carmi, Adam Falkowski, Eric Kuflik, Tomer Volansky, and Jure Zupan. Higgs After the Discovery: A Status Report. 2012.

[43] J.R. Espinosa, C. Grojean, M. Muhlleitner, and M. Trott. First Glimpses at Higgs' face. 2012.

[44] John Ellis and Tevong You. Global Analysis of the Higgs Candidate with Mass 125 GeV. 2012.

[45] Pier Paolo Giardino, Kristjan Kannike, Martti Raidal, and Alessandro Strumia. Is the resonance at 125 GeV the Higgs boson? 2012.

[46] Observation of an excess of events in the search for the standard model higgs boson in the gamma-gamma channel with the atlas detector. Technical Report ATLAS-CONF-2012-091, CERN, Geneva, July 2012.

[47] Evidence for a new state decaying into two photons in the search for the standard model higgs boson in pp collisions. Technical report, CERN, 2012.

[48] Coupling properties of the new higgs-like boson observed with the atlas detector at the lhc. Technical Report ATLAS-CONF-2012-127, CERN, Geneva, Sep. 2012.

[49] Leonard Susskind. Dynamics of Spontaneous Symmetry Breaking in the Weinberg-Salam Theory. *Phys.Rev.*, D20:2619–2625, 1979.

[50] Steven Weinberg. Implications of Dynamical Symmetry Breaking: An Addendum. *Phys.Rev.*, D19:1277–1280, 1979.

[51] Michael S. Chanowitz and Mitchell Golden. HIGGS BOSON TRIPLETS WITH M (W) = M (Z) cos theta omega. *Phys.Lett.*, B165:105, 1985.

[52] J.F. Gunion, R. Vega, and J. Wudka. Higgs triplets in the standard model. *Phys.Rev.*, D42:1673–1691, 1990.

[53] Peter Galison. LARGE WEAK ISOSPIN AND THE W MASS. *Nucl.Phys.*, B232:26, 1984.

[54] Spencer Chang. A 'Littlest Higgs' model with custodial SU(2) symmetry. *JHEP*, 0312:057, 2003.

[55] Heather Erin Logan. Radiative corrections to the Z b anti-b vertex and constraints on extended Higgs sectors. 1999.

[56] A.G. Akeroyd. Cascade decays of triplet Higgs bosons at LEP-2. *Phys.Lett.*, B442:335–343, 1998.

[57] Howard E. Haber and Heather E. Logan. Radiative corrections to the Z b anti-b vertex and constraints on extended Higgs sectors. *Phys.Rev.*, D62:015011, 2000.

[58] Combined search for the standard model higgs boson in pp collisions at sqrt(s) = 7 tev with the atlas detector. Technical Report CERN-PH-EP-2012-167, CERN, Geneva, August 2012.

[59] LHC Higgs Cross Section Working Group, S. Dittmaier, C. Mariotti, G. Passarino, and R. Tanaka (Eds.). Handbook of LHC Higgs Cross Sections: 1. Inclusive Observables. *CERN-2011-002*, CERN, Geneva, 2011.

[60] Georges Aad et al. A search for ttbar resonances with the ATLAS detector in 2.05 fb^{-}1 of proton-proton collisions at sqrt(s) = 7 TeV. 2012.

[61] A search for resonances in semileptonic top pair production. Technical Report CMS-PAS-TOP-11-009, CERN, 2012.

[62] J. Dai, J.F. Gunion, and R. Vega. Detection of neutral MSSM Higgs bosons in four b final states at the Tevatron and the LHC: An update. *Phys.Lett.*, B387:801–803, 1996.

[63] U. Baur, T. Plehn, and David L. Rainwater. Probing the Higgs selfcoupling at hadron colliders using rare decays. *Phys.Rev.*, D69:053004, 2004.

[64] Search for doubly charged higgs boson production in like-sign muon pairs in pp collisions at s=7 tev. Technical Report ATLAS-CONF-2011-127, CERN, Geneva, Sep 2011.

[65] Inclusive search for doubly charged higgs in leptonic final states at sqrt s=7 tev. Technical Report CMS-PAS-HIG-11-007, CERN, 2011.

[66] Cheng-Wei Chiang, Takaaki Nomura, and Koji Tsumura. Search for doubly charged Higgs bosons using the same-sign diboson mode at the LHC. *Phys.Rev.*, D85:095023, 2012.

[67] Mayumi Aoki and Shinya Kanemura. Unitarity bounds in the Higgs model including triplet fields with custodial symmetry. *Phys.Rev.*, D77:095009, 2008.

[68] Marco Farina, Christophe Grojean, and Ennio Salvioni. (Dys)Zphilia or a custodial breaking Higgs at the LHC. 2012.

[69] Ian Low and Joseph Lykken. Revealing the electroweak properties of a new scalar resonance. *JHEP*, 1010:053, 2010.

[70] A. Alves, E. Ramirez Barreto, A.G. Dias, C.A. de S. Pires, F.S. Queiroz, et al. Probing 3-3-1 Models in Diphoton Higgs Boson Decay. *Phys.Rev.*, D84:115004, 2011.

[71] A.G. Akeroyd and S. Moretti. Enhancement of H to gamma gamma from doubly charged scalars in the Higgs Triplet Model. 2012.

[72] Lei Wang and Xiao-Fang Han. The recent Higgs boson data and Higgs triplet model with vector-like quark. 2012.

[73] Mark W. Goodman and Edward Witten. Detectability of Certain Dark Matter Candidates. *Phys.Rev.*, D31:3059, 1985.

[74] David Tucker-Smith and Neal Weiner. Inelastic dark matter. *Phys.Rev.*, D64:043502, 2001.

[75] Spencer Chang, Aaron Pierce, and Neal Weiner. Momentum Dependent Dark Matter Scattering. *JCAP*, 1001:006, 2010.

[76] Brian Feldstein, A. Liam Fitzpatrick, and Emanuel Katz. Form Factor Dark Matter. *JCAP*, 1001:020, 2010.

[77] Yang Bai and Patrick J. Fox. Resonant Dark Matter. *JHEP*, 0911:052, 2009.

[78] Maxim Khlopov. Dark atoms and puzzles of dark matter searches. *Int.J.Mod.Phys.*, A29:1443002, 2014.

[79] Spencer Chang, Jia Liu, Aaron Pierce, Neal Weiner, and Itay Yavin. CoGeNT Interpretations. *JCAP*, 1008:018, 2010.

[80] Jonathan L. Feng, Jason Kumar, Danny Marfatia, and David Sanford. Isospin-Violating Dark Matter. *Phys.Lett.*, B703:124–127, 2011.

[81] Vincenzo Cirigliano, Michael L. Graesser, Grigory Ovanesyan, and Ian M. Shoemaker. Shining LUX on Isospin-Violating Dark Matter Beyond Leading Order. 2013.

[82] JiJi Fan, Matthew Reece, and Lian-Tao Wang. Non-relativistic effective theory of dark matter direct detection. *JCAP*, 1011:042, 2010.

[83] A. Liam Fitzpatrick, Wick Haxton, Emanuel Katz, Nicholas Lubbers, and Yiming Xu. Model Independent Direct Detection Analyses. 2012.

[84] Marco Cirelli, Eugenio Del Nobile, and Paolo Panci. Tools for model-independent bounds in direct dark matter searches. *JCAP*, 1310:019, 2013.

[85] Moira I. Gresham and Kathryn M. Zurek. On the Effect of Nuclear Response Functions in Dark Matter Direct Detection. *Phys.Rev.*, D89:123521, 2014.

[86] Riccardo Catena and Paolo Gondolo. Global fits of the dark matter-nucleon effective interactions. 2014.

[87] Vera Gluscevic and Annika H. G. Peter. Understanding WIMP-baryon interactions with direct detection: A Roadmap. 2014.

[88] Chiara Arina, Eugenio Del Nobile, and Paolo Panci. Not so Coy Dark Matter explains DAMA (and the Galactic Center excess). 2014.

[89] Douglas P. Finkbeiner, Tracy R. Slatyer, Neal Weiner, and Itay Yavin. PAMELA, DAMA, INTEGRAL and Signatures of Metastable Excited WIMPs. *JCAP*, 0909:037, 2009.

[90] Rouven Essig, Jared Kaplan, Philip Schuster, and Natalia Toro. On the Origin of Light Dark Matter Species. *Submitted to Physical Review D*, 2010.

[91] Peter W. Graham, Roni Harnik, Surjeet Rajendran, and Prashant Saraswat. Exothermic Dark Matter. *Phys.Rev.*, D82:063512, 2010.

[92] Tao Han and Ralf Hempfling. Messenger sneutrinos as cold dark matter. *Phys.Lett.*, B415:161–169, 1997.

[93] Lawrence J. Hall, Takeo Moroi, and Hitoshi Murayama. Sneutrino cold dark matter with lepton number violation. *Phys.Lett.*, B424:305–312, 1998.

[94] Yanou Cui, David E. Morrissey, David Poland, and Lisa Randall. Candidates for Inelastic Dark Matter. *JHEP*, 0905:076, 2009.

[95] Daniele S.M. Alves, Siavosh R. Behbahani, Philip Schuster, and Jay G. Wacker. Composite Inelastic Dark Matter. *Phys.Lett.*, B692:323–326, 2010.

[96] David E. Kaplan, Gordan Z. Krnjaic, Keith R. Rehermann, and Christopher M. Wells. Atomic Dark Matter. *JCAP*, 1005:021, 2010.

[97] Kunal Kumar, Arjun Menon, and Tim M.P. Tait. Magnetic Fluffy Dark Matter. *JHEP*, 1202:131, 2012.

[98] Haipeng An, P.S. Bhupal Dev, Yi Cai, and R.N. Mohapatra. Sneutrino Dark Matter in Gauged Inverse Seesaw Models for Neutrinos. *Phys.Rev.Lett.*, 108:081806, 2012.

[99] S.C. Kim, H. Bhang, J.H. Choi, W.G. Kang, B.H. Kim, et al. New Limits on Interactions between Weakly Interacting Massive Particles and Nucleons Obtained with CsI(Tl) Crystal Detectors. *Phys.Rev.Lett.*, 108:181301, 2012.

[100] G. Angloher, M. Bauer, I. Bavykina, A. Bento, C. Bucci, et al. Results from 730 kg days of the CRESST-II Dark Matter Search. *Eur.Phys.J.*, C72:1971, 2012.

[101] Jo Bovy and Scott Tremaine. On the local dark matter density. *Astrophys.J.*, 756:89, 2012.

[102] F. J. Kerr and D. Lynden-Bell. Review of galactic constants. *Mon.Not.Roy.Astron.Soc.*, 221:1023–1038, August 1986.

[103] Martin C. Smith, G.R. Ruchti, A. Helmi, R.F.G. Wyse, J.P. Fulbright, et al. The RAVE Survey: Constraining the Local Galactic Escape Speed. *Mon.Not.Roy.Astron.Soc.*, 379:755–772, 2007.

[104] R. Bernabei, P. Belli, V. Landoni, F. Montecchia, W. Di Nicolantonio, et al. New limits on WIMP search with large-mass low-radioactivity NaI(Tl) set-up at Gran Sasso. *Phys.Lett.*, B389:757–766, 1996.

[105] E. Behnke et al. Direct Measurement of the Bubble Nucleation Energy Threshold in a CF3I Bubble Chamber. *Phys.Rev.*, D88:021101, 2013.

[106] H. Park, D.H. Choi, J.M. Choi, I.S. Hahn, M.J. Hwang, et al. Neutron beam test of CsI crystal for dark matter search. *Nucl.Instrum.Meth.*, A491:460–469, 2002.

[107] J.I. Collar, N.E. Fields, E. Fuller, M. Hai, T.W. Hossbach, et al. Coherent neutrino-nucleus scattering detection with a CsI[Na] scintillator at the SNS spallation source. 2014.

[108] Joachim Kopp, Thomas Schwetz, and Jure Zupan. Global interpretation of direct Dark Matter searches after CDMS-II results. *JCAP*, 1002:014, 2010.

[109] Karin Dissauer, Mads T. Frandsen, Tuomas Hapola, and Francesco Sannino. Perturbative extension of the standard model with a 125 GeV Higgs boson and magnetic dark matter. *Phys.Rev.*, D87(3):035005, 2013.

[110] Neal Weiner and Itay Yavin. UV Completions of Magnetic Inelastic Dark Matter and RayDM for the Fermi Line(s). *Phys.Rev.*, D87:023523, 2013.

[111] Jason Kumar and Danny Marfatia. Matrix element analyses of dark matter scattering and annihilation. *Phys.Rev.*, D88(1):014035, 2013.

[112] Peter Galison and Aneesh Manohar. TWO Z's OR NOT TWO Z's? *Phys. Lett.*, B136:279, 1984.

[113] Maxim Pospelov, Adam Ritz, and Mikhail B. Voloshin. Secluded WIMP Dark Matter. *Phys. Lett.*, B662:53–61, 2008.

[114] Nima Arkani-Hamed, Douglas P. Finkbeiner, Tracy R. Slatyer, and Neal Weiner. A Theory of Dark Matter. *Phys.Rev.*, D79:015014, 2009.

[115] Rouven Essig, Philip Schuster, Natalia Toro, and Bogdan Wojtsekhowski. An Electron Fixed Target Experiment to Search for a New Vector Boson A' Decaying to e+e-. *JHEP*, 02:009, 2011.

[116] Andrea Celentano. The Heavy Photon Search experiment at Jefferson Laboratory. *J. Phys. Conf. Ser.*, 556(1):012064, 2014.

[117] J.P. Lees et al. Search for a Dark Photon in e^+e^- Collisions at BaBar. *Phys.Rev.Lett.*, 113(20):201801, 2014.

[118] Vindhyawasini Prasad, Haibo Li, and Xinchou Lou. Search for low-mass Higgs and dark photons at BESIII. 2015.

[119] Philip Ilten, Jesse Thaler, Mike Williams, and Wei Xue. Dark photons from charm mesons at LHCb. 2015.

[120] Nima Arkani-Hamed and Neal Weiner. LHC Signals for a SuperUnified Theory of Dark Matter. *JHEP*, 12:104, 2008.

[121] L. Lavoura and Ling-Fong Li. Making the small oblique parameters large. *Phys. Rev.*, D49:1409–1416, 1994.

[122] Adam Alloul, Neil D. Christensen, Cline Degrande, Claude Duhr, and Benjamin Fuks. FeynRules 2.0 - A complete toolbox for tree-level phenomenology. *Comput. Phys. Commun.*, 185:2250–2300, 2014.

[123] Alexander Belyaev, Neil D. Christensen, and Alexander Pukhov. CalcHEP 3.4 for collider physics within and beyond the Standard Model. *Comput. Phys. Commun.*, 184:1729–1769, 2013.

[124] Georges Aad et al. A search for prompt lepton-jets in pp collisions at $\sqrt{s} = 7$ TeV with the ATLAS detector. *Phys. Lett.*, B719:299–317, 2013.

[125] Vardan Khachatryan et al. A Search for Pair Production of New Light Bosons Decaying into Muons. 2015.

[126] David Curtin, Rouven Essig, Stefania Gori, and Jessie Shelton. Illuminating Dark Photons with High-Energy Colliders. *JHEP*, 02:157, 2015.

[127] Georges Aad et al. Search for new light gauge bosons in Higgs boson decays to four-lepton final states in pp collisions at $\sqrt{s} = 8$ TeV with the ATLAS detector at the LHC. 2015.